Silence of the Lamb Waves

by

Rishon Robert Benjamin

B.S. in Chemical Engineering
Drexel University, 2015

Submitted to the Computation for Design and Optimization (CDO) Department
In partial fulfillment of the requirements for the degree of
Master of Science in CDO
at the

MASSACHUSETTS INSTITUTE OF TECHNOLOGY

June 2017

Signature redacted

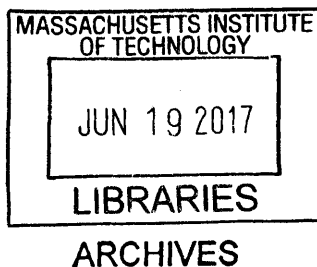Author..
Computation for Design and Optimization
May 31, 2017

Signature redacted

Certified by.......
Brian W. Anthony
Principal Research Scientist, Mechanical Engineering
Thesis Supervisor

Signature redacted

Accepted by..................................... ....
Nicolas Hadjiconstantinou
Professor of Mechanical Engineering
CDO Co-Director

2

ABSTRACT

Roll-to-Roll (R2R) manufacturing has seen great interest in the recent decade due to the proliferation of personalized and wearable devices for monitoring a variety of biometrics. Given the sensitive nature of the potential applications of these sensors, the throughput of manufacturing due to increased demand, and the scale of the electrical components being manufactured, R2R flexible electronics manufacturing technologies require new sensing and measurement capabilities for defect detection and process control.

The work presented herein investigates the use of ultrasound, specifically Lamb and longitudinal waves, as a sensing modality and measurement technique for thin film R2R manufacturing substrates. Contact (transducer-based) and non-contact (photoacoustic) generation methods along with deterministic and probabilistic tomographic reconstruction algorithms were implemented evaluate their suitability for non-destructive evaluation (NDE) and in-line control of surface additions of $76 \mu m$ aluminum and polyethylene terephthalate (PET) films. The ultrasonic waves were used to ascertain properties of these substrates such as the thickness of substrate, applied load, presence of defects (holes/cracks), size of defects, presence of surface features (fluid drops, multi-layer structures), and nature of surface features (differing chemistries). In addition, surface features alter the behavior of sound waves in the presence of such features. These surface features may then be imaged to create tomographic maps.

The results presented show that, currently, a quasi-contact acoustic generation scheme can be used to successfully image defects and surface features on the order of ~1mm. Furthermore, the algorithm is able to distinguish qualitatively between surface features of differing physiochemical properties.

The authors hope that the information collected from this thesis will be part of a rich data set that can contribute to advanced machine-learning frameworks for predictive maintenance, failure, and process control analysis for the R2R process.

Thesis Supervisor: Brian W. Anthony
Title: Principal Research Scientist, Mechanical Engineering

ACKNOWLEDGEMENTS

support and help navigating the MIT system; you provide us students with incredible support and are the sole reason why we can focus on our work here at MIT.

Finally, I come to the very core of my existence: My family. Of all the gems I have found at MIT, the one that shines the brightest is my girlfriend Ina Kundu. You have had the misfortune of witnessing me at my absolute worst, but have stuck with me through all of it. From my crazy cologne obsessions to complete lack of any artistic talent, you have allowed me to grow in my own ways. From the bottom of my heart, I thank you for showing me a part of myself I never knew existed. Thank you also to the Kundu family for accepting me so graciously. Dr. and Mrs. Kundu, and Auni, your warmth, care, and advice through some tough times truly mean a lot to me. Within the short span of a year, I have been fortunate to have gotten a second family.

Next, I would like to thank my parents, Anny and Robert. Mom and Dad, the 100 odd pages of this document would not be enough to thank you for what you have done. Everything I have today, I mean every single thing, is because of you. You gambled your lives coming to the USA and have faced a number of challenges in doing so. Nevertheless, you persevered for Alex and me and our lives are testaments to the unbelievable job you guys did raising us.

Last but not least, thank you to my brother Alex. It is the most amazing feeling to have known that you were by my side for the last 24 years. I have never felt alone knowing that you were often just a few feet away. I have learned so much from you that I cannot even begin making a list. You are incredibly gifted and I wish you much luck as you journey towards a PhD. I am immensely proud to call you my brother and I look forward to the Benjamin Brothers kicking ass for years to come!

I would like to take this moment to specially thank my grandmother in India. Amama, you have been with me and Alex far longer than anyone else has. From feeding us before going to school to getting us dressed to scolding us for being nuisances to buying us unexpected treats, we are forever in your debt. For both of us, you have been a second mother. I wish you could have been with us during our graduations.

As I conclude, I would like to thank my dear friend Cup O'Joe. Hot or cold, sweet or bitter, small or large, you have been an unjudging friend. Thank you for accompanying me on long drives, long nights, and tough days. From your most faithful addict, I thank you for your companionship.

And with that I raise a cup of coffee as a toast to everyone mentioned herein—Thank you.

CONTENTS

8

FIGURES

12

TABLES

14

1

MOTIVATION

1.1 Forward Looking Statement

Before we get into the minute details and technicalities of ultrasound based non-destructive evaluation techniques, it behooves us to remember the overarching motivation for this line of research. The authors would strongly like to emphasize that, much like all research is, this is not a standalone work. The results presented here are building towards an overarching objective; one of an industry that relies on smart manufacturing and predictive analyses. Because manufacturing research without a product-oriented focus seldom leads to significant breakthroughs, we have identified big-data sensing and analysis demands which are key to the successful continued commercial scale-up of R2R manufacturing technologies.

R2R processes require high-precision, non-rigid, registration-control of web or sheet based substrates. Functional fluids must be transferred onto a moving substrate with a specified pattern, film-thickness, width, and surface roughness. The quality of the results depends on the measured quality of the input materials and on precision process control; both of which require a lot of data. The ability to capture and analyze massive quantities of high-speed, high-resolution, heterogeneous sensor data and to use the output information for control and post deployment root-cause failure analysis is critical enabling innovations.

We expect the research outcomes to not only spur innovation in the R2R space but also in other sectors of the manufacturing economy that require data intensive sensing and processing. In essence, the objective of this project is to create a data stream that allows the user to monitor the manufacturing of flexible electronics in real-time and adjust the process as needed.

CHAPTER

2

INTRODUCTION

2.1 Roll-to-Roll Manufacturing

2.1.1 Overview of Process

Roll-to-Roll (R2R) manufacturing is a process that involves the addition or subtraction of components of a variety of sizes onto a continuously moving substrate. Substrate materials can include plastics such as PET and metals such as aluminum with the print features being as small as a few hundred nanometers. The relatively high throughput (substrates move at speeds in the range of 1-20 m/min), and low cost are what differentiate R2R manufacturing from other manufacturing processes [1, 2]. As the substrates move along at relatively high speeds, a number of different addition/subtraction processes can be performed. Examples of them include:

1) **Soft Lithography [2, 3]:** This process involves depositing a photoresist layer onto the substrate, UV curing a pattern into the photoresist, and cleaning/etching the unnecessary material off the substrate. This is perhaps one of the most widely used R2R manufacturing techniques.
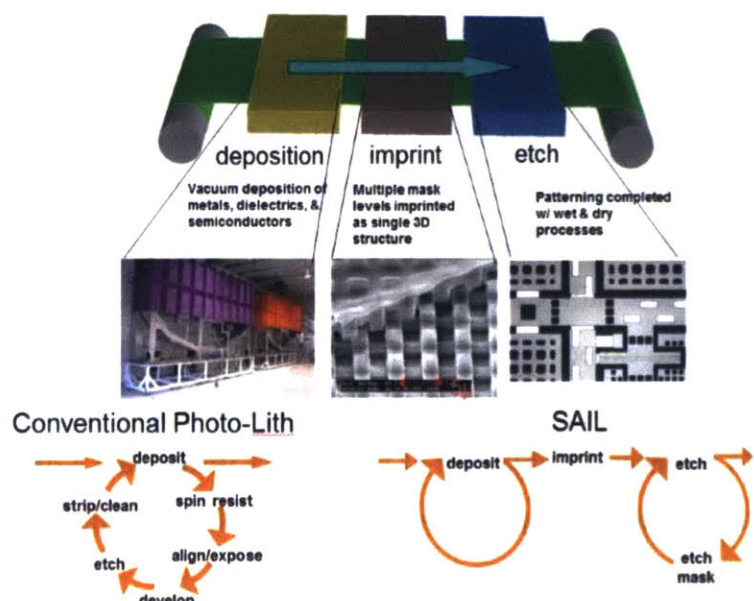
Figure 1: Soft Lithography for R2R Manufacturing [2]

16

2) **Laser Ablation [2, 4]**: As seen in Figures 2 and 3, this process involves directly irradiating a moving polymer substrate with a laser pulse in order to break up the polymer chains using a specific mask or pattern. The loose chains are cleared away leaving a flexible pattern on a polymer substrate.
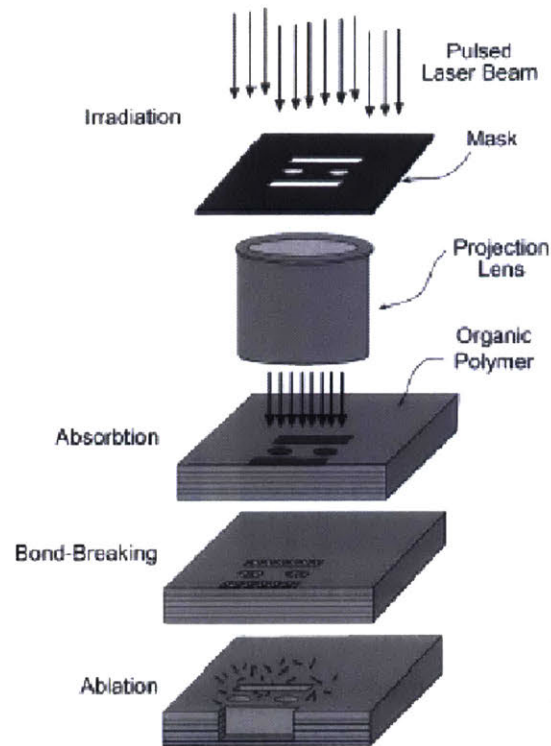
Figure 2: Laser Ablation of Polymer Substrates [2]
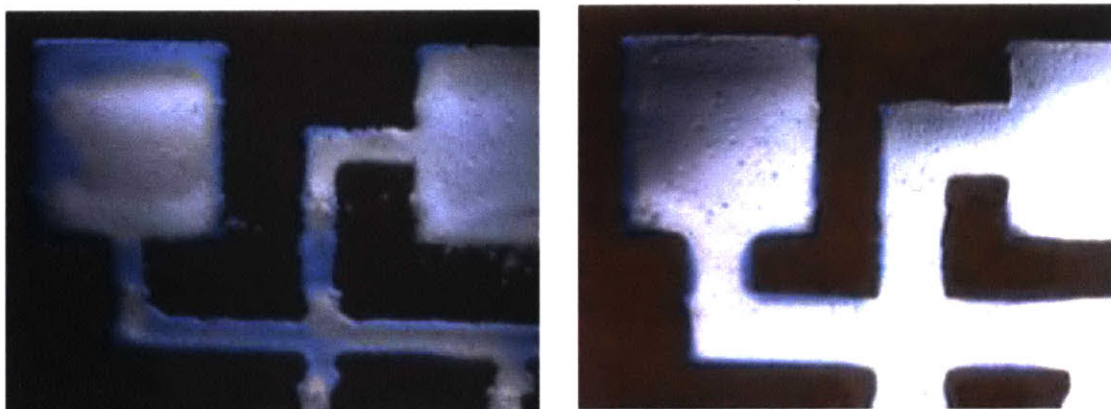
Figure 3: Sample Printed Pattern using (a) 50W power and (b) 80W power [4]

3) **Inkjet Printing [4, 5]**: This process involves addition of nano- and micro- scale patterns onto a moving substrate using a thermal printer. A variety of materials can be printed onto the moving substrate depending on the temperature of the printer. In Figure 4(a), silver has been printed onto a polymer substrate and in 4(b), carbon has been deposited onto a polymer.
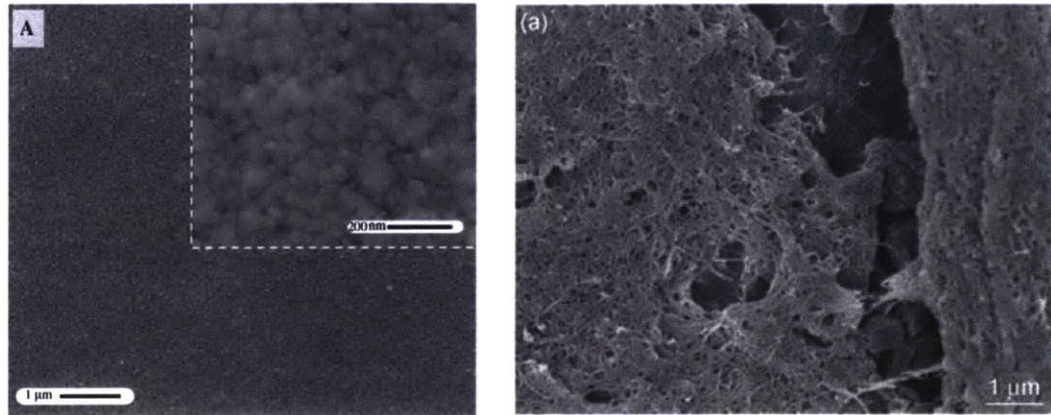
Figure 4: (a) Silver Thermally Printed onto Polymer (b) Carbon Thermally Printed onto Polymer [4]

Whether it is additive or subtractive, R2R manufacturing has wide ranging applications ranging from flexible Organic Light Emitting Diodes (OLED's) and thin-film Li-ion batteries to smart fibers and chemical separation membranes. Furthermore, the market for flexible electronics is expanding at a rate that necessitates the use of R2R for affordable manufacture of sensors/electronic devices.
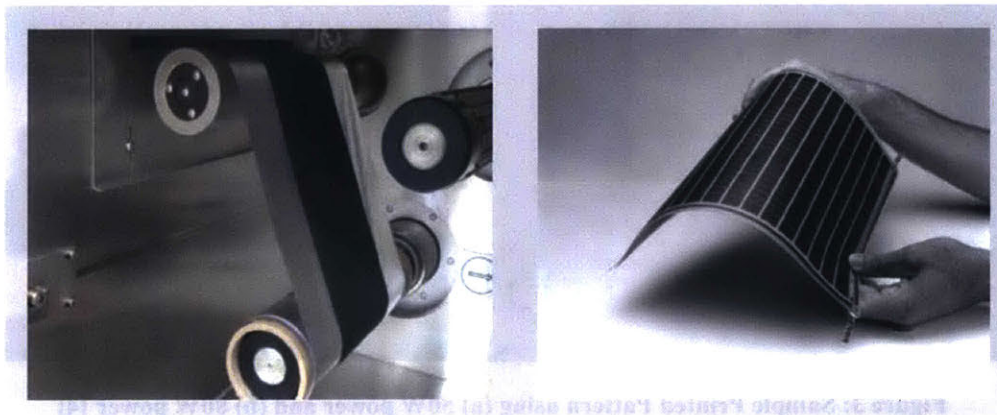
Figure 5: (a) Battery and (b) Solar Panels Produced using R2R Manufacturing [6]

Figure 6: Vision of a Flexible Display Produced by Universal Display Corp [6]

2.1.2 Need for Control in R2R Manufacturing

Inspection is a significant part of the R2R production environment because it assures the quality, determines the yield, and directly impacts the cost of final product. R2R processing only makes sense when the individual process steps have high yields because no defects can be removed from a roll before the full-roll processing is completed [15]. The scrap cost for R2R produced products will always be higher compared to batch produced products; the costs for emerging applications are dominated by the materials cost [7]. Production costs are reduced if yield and quality are maximized. To increase yield and product quality, and reduce waste and cost, monitoring and preventive machine maintenance and handling-procedures are essential.

In the conventional microelectronics industry - such as LCD display productions - yields are high as a result of successive investment in production and analysis techniques as the industry has scaled. On the other hand, R2R fabrication of electronic devices, such as OLED panels and organic photovoltaics (OPVs) is incredibly materials-intensive [8]. The industry demanded objective of this project is to raise the overall manufacturing yield of R2R manufacturing lines, to achieve cost-effective production yields of higher than 95%, so as to minimize wasting expensive substrates, chemicals, metals and other materials [10]. This industry is in the early stages and manufacturers are hesitant to share their yield information, but companies engaged in this manufacturing process would like to see improved yields. Due to the nascent nature of this technique, there is a reluctance to scale-up the volume of production until technologies for identifying and repairing defects, down to the smallest sizes, are developed [11].

The most significant objectives of this project are to raise the overall manufacturing yield of R2R manufacturing lines which will result in lower manufacturing and product costs. One expected outcome is to help reduce energy use and material waste which will result in lower manufacturing and product costs. A correlated support objective is to start to developing the framework for big-data analysis required to manage, process, and use the high-dimensionality, high-velocity, data stream that comes from the data-intensive inspection technologies required for detecting defects such as pinholes and cracks, measurement of web and pattern properties, and inspection for inter-layer delamination and voids [12]. Such data acquired during the manufacturing process will be integrated into process control and feedback systems [14]. These data, combined with functional information, can be used to learn how defects correlate to degraded performance. Defect maps can then be generated and disturbed to all process steps and used to ensure that regions of reduced quality are not processed further and do not reach final product after roll slicing and dicing. Finally, these data can then be used to support predictive machine maintenance and predictive optimization of future products.

The global flexible electronics (FE) market is anticipated to grow at a compounded annual growth rate of 25% during 2016 (revenue $5.42 billion) and 2022 (revenue $20.67 billion)[9,13]. Such a high growth rate is spurred by the ever-expanding consumer goods industry, versatility of application of flexible circuits, light weight and compact structure of these FE's, and the relative environmental friendliness of the finished products. In looking for high impact areas for advanced FE manufacturing research, we have identified processes that will have the broadest impact on the large-scale production of devices and sensors. Continuous R2R manufacturing processes offer the best potential for enabling the manufacturing of many of FEs emerging from research.

2.1.3 Challenges with R2R Manufacturing

Patterned metal, metal oxide and semiconductor films are ubiquitous components of electrical, chemical and optoelectronic devices. To date, these films are predominately prepared by additive processing wherein a planar film is deposited via batch deposition processes, often under conditions of vacuum and high temperature, and patterned using lithographic masks and subsequent etching [16]. In this complex manufacturing research effort, we advance an alternative approach based on R2R processing on flexible polymer, metal film or flexible glass

20

substrates to produce structures with critical dimensions as small as 100 nm at near-ambient temperatures at high production rates. A R2R approach offers the potential to radically shift the cost-structure for large area nanostructured devices and will enable applications including optical metamaterials, multifunctional, active surfaces, steerable and integrated antennas, advanced and multipurpose IR sensors, and printed energy scavenging and management systems. Moreover, R2R additive processes offer substantial improvements in materials and energy efficiency and, due to their direct print nature, can be practiced on portable tools with modest footprints for remote fabrication [18].

Printing nano- or micro-scale patterns on meter scale flexible webs, as in the R2R process, brings forth challenges of pattern analysis and machine intelligence in big data for quality inspection, defect detection, and process control. While printed-pattern fidelity and function are the overarching concerns for the R2R manufacturing process, specific process parameters include, but are not limited to, web and sheet tension, layer-to-layer registration, and fluid transfer rate, as well as the properties of the substrate (surface energy, surface roughness, thermal deformation, adhesiveness, etc.) [17]. Heterogeneous, jointly analyzed, sensory-data sources are required to visualize, quantify, and control the aforementioned print-patterns of each step of a R2R process. Given the high-volume and continuous nature of the processes, these data sources are high-volume, high-dimensionality, and continuously streaming [19]. Making sense of such big data requires high-performance networked-computation, along with process models. The information extracted from the data will support real-time quality monitoring, print pattern recognition and analysis, real-time statistical feedback/feedforward process control, and post deployment root-cause failure analysis. Advanced machine learning on the sensing data will support predictive maintenance and predictive optimization of future products. A high-level schematic of the project objectives can be seen in Figure 7.

The goal of this thesis is to develop a novel inspection tool that will seek to assist with the creation of a feedback loop that will maintain films and patterns over space and time as material, machine, and environmental disturbances occur. Real-time, in-line measurements of R2R on nanometer to meter length scales are necessary for statistical process monitoring and feedback control, which is not possible for a human inspector and not available in commercial inspection tools [20]. Additionally, topographic and electrical property maps may be used as the input to feedback and actuation systems to control the R2R manufacturing processes.

The ultrasonic inspection methods we explore here can augment existing process control and metrology techniques by raising the overall manufacturing yield by providing an information rich data stream for high-speed in-line sensing, deep learning, characterization and data visualization techniques targeted at defect detection, print pattern quality monitoring, and feedback control [21]. Success in this area will have a broad impact on the large-scale production of FE. The proposed work will be relevant to key underlying manufacturing technologies such as formation of coated surfaces, micro and nano patterned templates, micro-patterned vapor-deposited polymers, etc. where process control is critical. Furthermore, micro-scale monitoring and control over a large area, implemented in a continuous basis has the potential for enabling the manufacturing of many new technologies such as transfer printing and micro- and nano-imprint patterning.

With a rigorous process control framework, we will improve yield on very large-area, high-rate production. The expected improvements are enhanced energy and materials efficiency, which in combination with higher production rate will result in lower manufacturing and product costs, thereby increasing competitiveness and sustainability.

Real-time Digitized Data

CAD model-based inspection

Cloud-based platform for storage and deployment

Process Regulation

Dimensionality expansion

Information Integration

Condensation pattern recognition

Large area image distortion analysis

Tomographic mapping

Print Surface Features

Environmental imaging

Optical

Photoacoustic

Misc. Modes

R2R Manufacturing

Predictive control

Deep learning

Tomographic map

Pattern Extraction

Data Mining

Human-machine interface

Process Control (Feedback Loop)

Figure 7: Smart R2R Manufacturing, Inspection, and Process Control Architecture

3

NON-DESTRUCTIVE EVALUATION (NDE)

3.1 Introduction

There has been much interest in recent years on sensor/electronics manufacturing due to the advent of personalized medical devices. From heart rate monitors to step counters to sleep trackers, these devices have become multi-functional, light weight, and relatively cheap. At the very core of these devices are micro- and nano- scale sensors embedded onto pliable substrates that can hug body contours. Given the sensitive nature of printing micro- and nano- scale components on fast moving substrates using R2R and other continuous manufacturing techniques, there has been increased focus on the non-destructive detection and quantification of defects and damages in substrates including but not limited to cracks, voids, cutouts etc. within the thickness of the substrates or on the surface of them.

3.2 NDE of R2R Manufacturing

Given the nature of personalized devices and sensors, continuous in-line Non-Destructive Evaluation (NDE) of the R2R manufacturing process has been the subject of much interest. Commonly used non-destructive methods for quantifying bulk defects in R2R substrates can be seen below.

3.2.1 Visual and Optical Testing

This mode of testing represents the most common and simple means of evaluating the R2R process. This test basically involves illumination of the substrate followed by capturing different visual stimuli at high resolutions.

3.2.1.1 Direct Visual Inspection
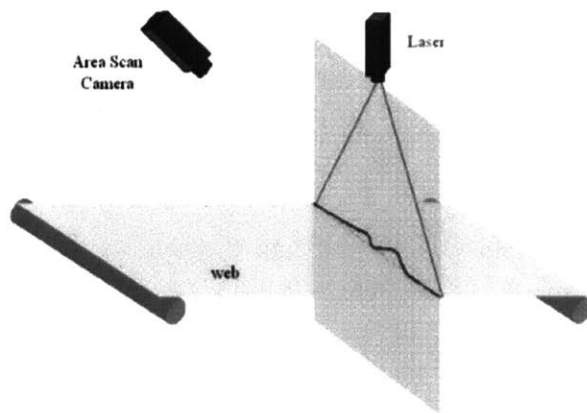
This form of visual testing involves the use of mirrors, cameras, and telescope to acquire high-resolution images using devices with relatively high frame rates. Figure 8 is an illustration of the use of high-accuracy cameras and laser to detect wrinkles in the moving web [22].

Figure 8: Direct Visual Inspection of Moving Web in R2R Manufacturing [22]

3.2.1.2 Remote Visual Testing

For surfaces and substrates that are not directly accessible to the human eye, indirect means of visual inspection such as glass fibers permits the viewer to inspect objects with minimum interference to operation. Differences in these two modalities can be seen in Figure 9.
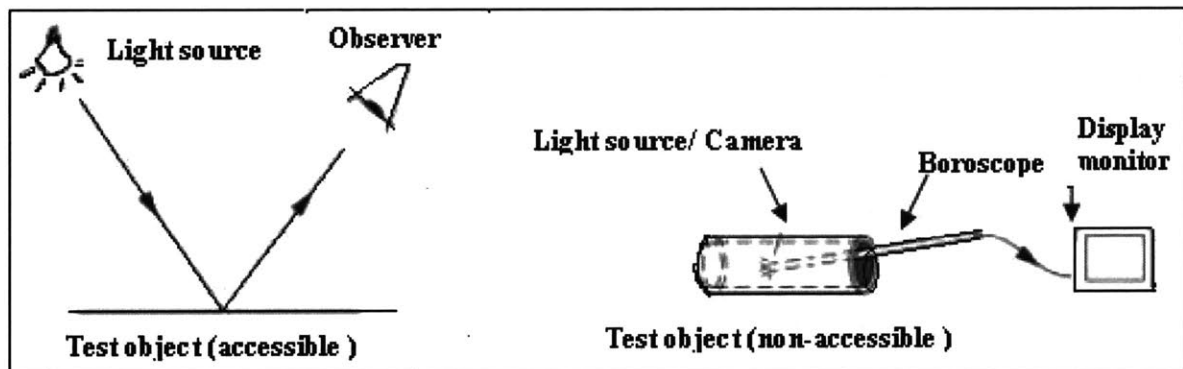
Figure 9: Differences in Direct and Indirect Visual Inspection of R2R Substrates [22]

The main advantages of visual inspection are the relatively low cost of setup and ability to acquire real-time data thereby allowing for instantaneous analyses. However, drawbacks of this technique include high-rate of misinterpretation, variation in result quality due to lighting conditions, and the inability to probe for defects below the surface. The ability to detect defects within the thickness of the substrate is extremely important for a process such as the R2R manufacturing.

3.2.2 Visual and Optical Testing

This is a contrast-based evaluation technique that is used to detect surface breaking in substrates. As seen in Figure 10, during this process a dye or marker-laden penetrant is poured over the substrate. Once the penetrant enters the cracks, the penetrant is cleaned off and the substrate is dusted with a developer material that selectively binds to the dye in the cracks. Visual inspection can then be used to identify defects [23,24].

Penetrant

Steel crack   **Delaminated fiber composite**
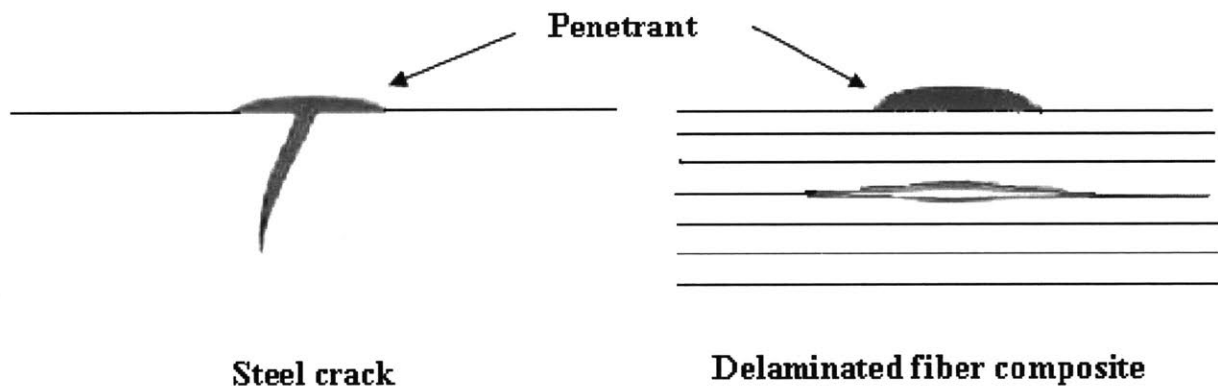
Figure 10: Schematic of the Liquid Penetrant Testing Scheme for R2R Substrates [24]

Advantages of this method include indifference to substrate material (metallic, conductive, magnetic etc.), high sensitivity to small surface discontinuities, and the ability to inspect large areas rapidly and at low cost. On the flip side, this technique loses favor due to its inability to provide real-time analyses and the inability to provide any information about defects within the thickness of the material.

3.2.3 Magnetic Particle Inspection

This is a non-destructive technique used for bulk defect detection. MPI uses strong magnetic fields combined with magnetic particles to detect flaws as show in Figure 11. In essence, if there is a break in the material, a resultant magnetic flux leak will occur and ferromagnetic particles on the surface of the surface will gravitate to these leaks [24,25]. Advantages of this method lie in its simplicity and ease of use. However, the restriction of the inspection of only ferromagnetic materials makes this technique ineffective. Furthermore, the presence of electronic components on substrates makes this technique harsh and prone of damaging the finished goods.
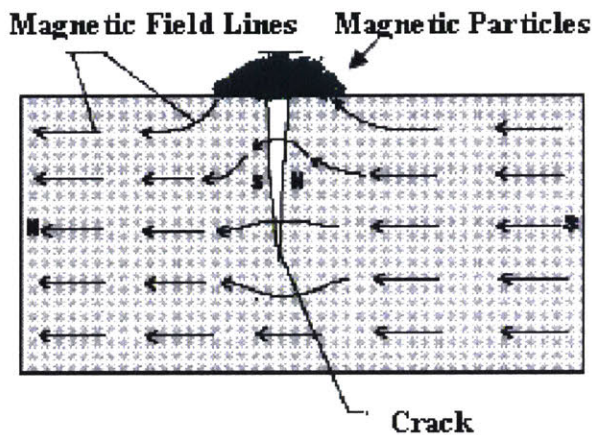
Figure 11: (a) Magnetic Particle Inspection Methodology for R2R Substrates [24] (b) Crack Identification due to Selective Binding of Magentic Particles [25]

3.2.4 Electromagnetic Testing

During this method of inspection, an electric field is produced in the substrate by a time-varying magnetic field [24,26]. The electric currents produced in this manner are knowns as eddy currents and

27
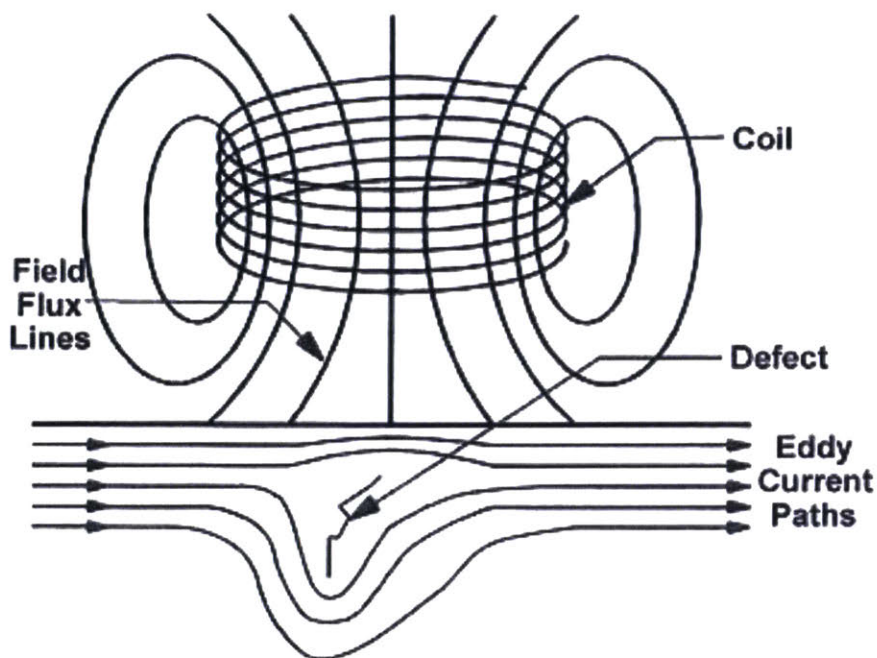
Figure 12: Electromagnetic Testing of Substrates for R2R Manufacturing [26]

tend to flow in circles. As such, imperfections in the path of these eddies will result in a reduction in the strength of the eddies and this can be detected using appropriate equipment. Despite being easy to use, this method of testing relies on the ability of the substrate to be electrically conductive. This is becoming less and less true because there is a preference for the use of light polymers in medical and personal health devices.

3.2.5 Radiography

In general, this method involves bombarding substrates with high-energy penetrating waves such as gamma or X-ray to probe for imperfections. A receiver re-creates features within the substrate using parameters such as attenuation, changes in refractive indices, and absorption properties [24,27]. Given that electromagnetic waves are used as probes, advantages of this technique include high sensitivity and speed. However, the energy intensive nature of the waves poses significant hazards to the user and the materials being inspected.

3.2.6 Ultrasonic

Ultrasonic sound waves in the range of 0.2 to 30 MHz result in the production of bulk stress waves that can be used to probe structural defects. These waves can be excited in a variety of substrate materials and are extremely cheap and safe to produce.

3.2.6.1. Pulse-Echo Method

In this method, as shown in Figure 13, ultrasound pulses are fired from one end of the material and signals deflecting off defects are received on the same side. Characteristics such as time of arrival of these pulses and amplitude of the received pulses can then be used to identify the presence of defects in the material [28]. While this method of inspection is safe, cheap, and easy to setup, it is largely used to probe bulk defects and provides no information about the surface of the substrate being probed.

28
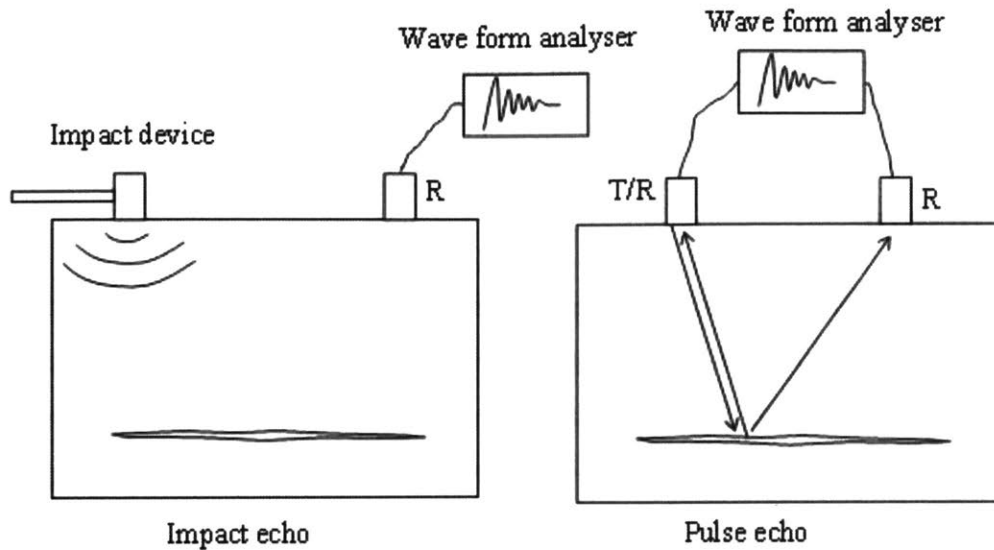
Figure 13: Pulse-Echo Method for Ultrasonic Inspection of Structures [24]

3.2.6.2 Resonance Technique

This ultrasonic method is primarily used to measure thickness of substrates. This is typically done by determining the resonant frequencies of the material under consideration and this value is related to material thickness based on the following equation where h is the thickness of the substrate:

$$h = \frac{c_l}{4(f_{n+1} - f_n)}, n = 1,2,3..n \qquad (3.1)$$

3.2.6.3 Plate Waves (Lamb Waves)

In recent years, there has been growing interest in the use of Lamb waves for the NDE of thin film substrates. This type of ultrasonic propagation will be the focus of majority of this thesis and the theory behind these waves will be explicated upon in later sections. Lamb waves are sound waves that travel within very thin plates. As such, these waves interact with the surfaces of the plates (or substrates) and can not only probe bulk defects, but also surface additions/deletions. Besides being cheap to produce and safe for the materials being inspected,

we hypothesize that Lamb waves can be used for large scale inspection of substrates that are moving at high speeds making it an ideal candidate for inspecting the R2R manufacturing process.

3.3 Conclusion

A summary of the different inspection techniques and their capabilities in comparison to the proposed Lamb Wave based inspection technique is delineated in Table 1. Our hypothesis is that the ultrasonic mode (Lamb waves and longitudinal waves), provides the ability to inspect bulk AND surface properties of substrates. The comparative advantage forms the basis of the experiments and results outlined in the sections below.

Table 1: Comparison of NDE Techniques for Application to the R2R Manufacturing Process

Defect Type	Radiography	Ultrasonic	Electromagnetic	Visual	Liquid Penetrate
Voids	Yes	Yes	No	No	Only surface
Debonds	Yes	Yes	No	No	Only surface
Delamination	Yes	Yes	No	No	Only edge
Break/Cracks	Yes	Yes	Yes	No	No
Micro-cracks	Yes	Yes	Some	No	No
Surface Features	No	Yes	No	Yes	No

CHAPTER

4

LONGITUDINAL ULTRASONIC NDE

4.1 Introduction

As seen in Table 1, ultrasonic based NDE of thin films holds the promise of being able to image not only the bulk of the material, but also surface features. Since longitudinal waves are the easiest to produce in solids, this type of ultrasonic testing was first explored during this research. Longitudinal waves are pressure waves that travel through the medium in question at a constant speed irrespective of the frequency of the exciting transducer. During this type of wave propagation, the particles in the medium are displaced (compression or rarefaction) parallel to the direction of wave propagation. A schematic of this can be seen in Figure 14:
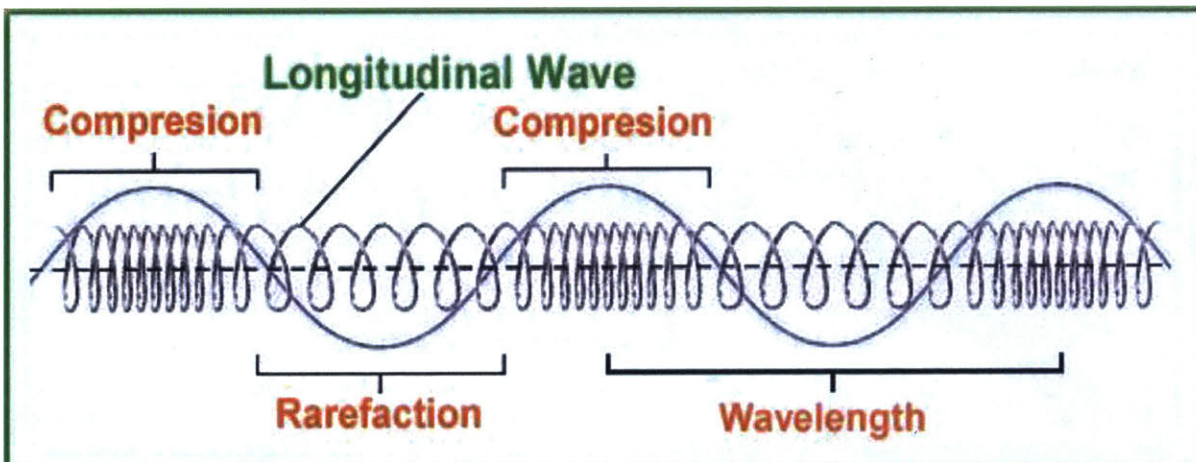
Figure 14: Propagation of Longitudinal Sound Wave [29]

4.2 Experimental Setup

A 76 μm thick polyethylene terephthalate (PET) was used as the substrate. In order to inject a longitudinal wave into the material, a custom designed acrylonitrile butadiene styrene (ABS) wedge at an angle that successfully refracted the incoming longitudinal wave into the bulk of the film according to Snell's law (4.1) was used [30].

$$\frac{\sin(\phi)}{\sin(\gamma)} = \frac{c_i}{c_r} \tag{4.1}$$
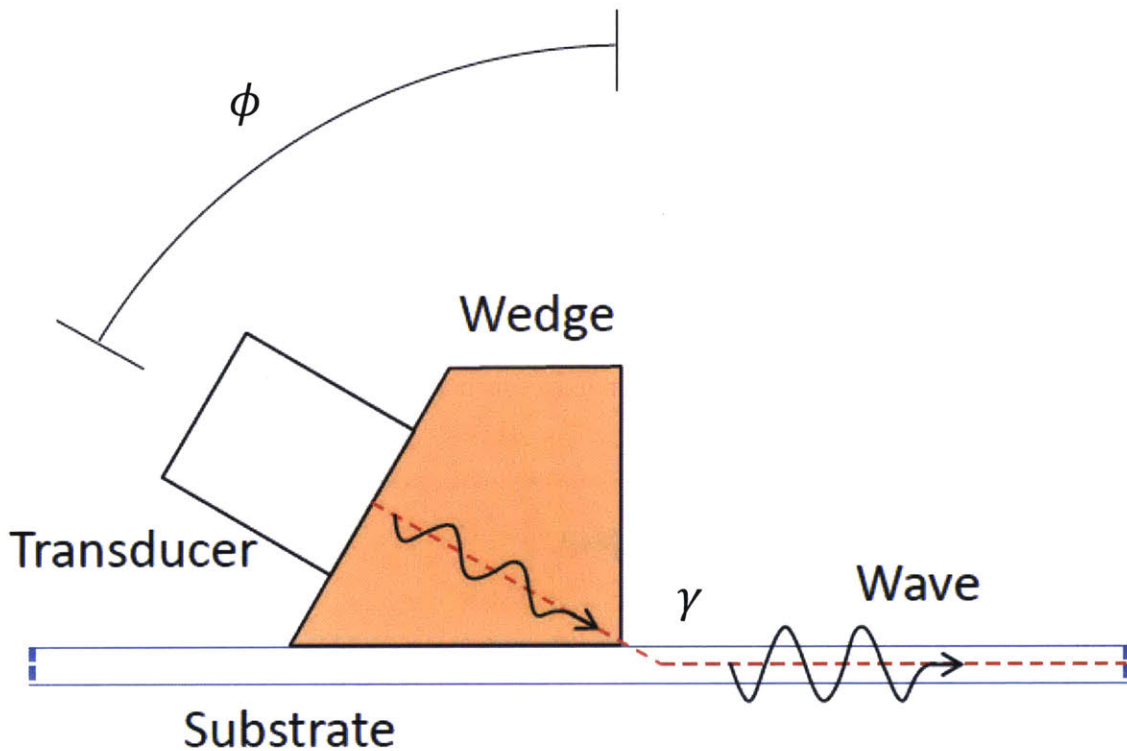
Figure 15: Refraction of Wave from ABS Wedge into PET Film [30]

Here ϕ is the angle of incidence and γ is angle of refraction. Similarly, c_i and c_r are the speeds of sound incident (in the ABS wedge) and refracted (in PET). The goal behind using these wedges was to refract the incident sound waves on the film at an angle of 90° so that the sound wave could travel along the thickness of the substrate. ABS was chosen due to its relatively higher speed of sound as compared to PET and ease of availability/printability. Given the speeds of sound in ABS (~2100 m/s) and PET (~2400 m/s) and an angle of refraction (γ)of

90°, the angle of incidence was determined to be 61°. As such a wedge with an angle of 60° from the vertical was used to introduce the wave into the film and capture the propagating wave.
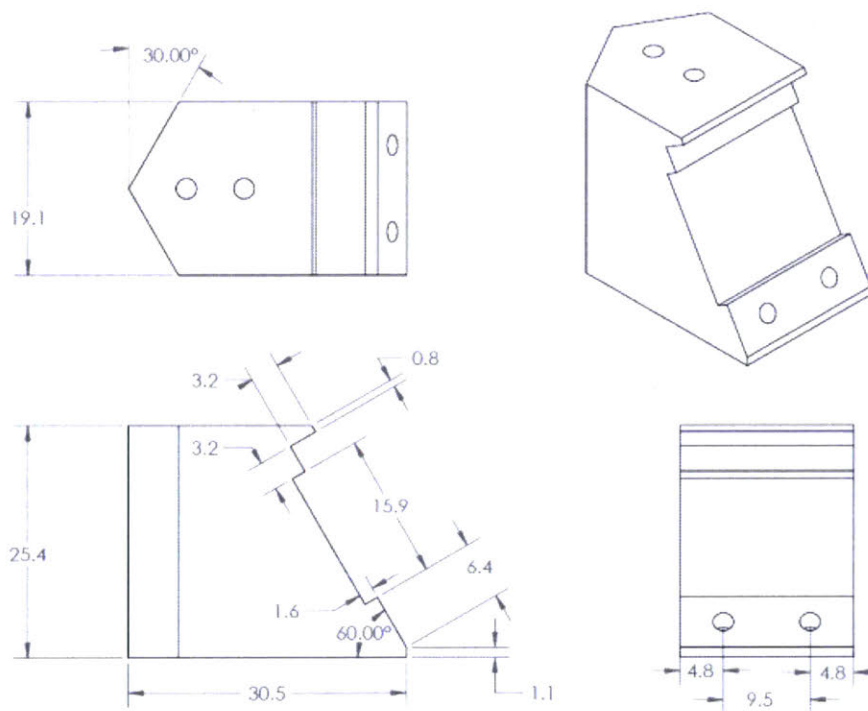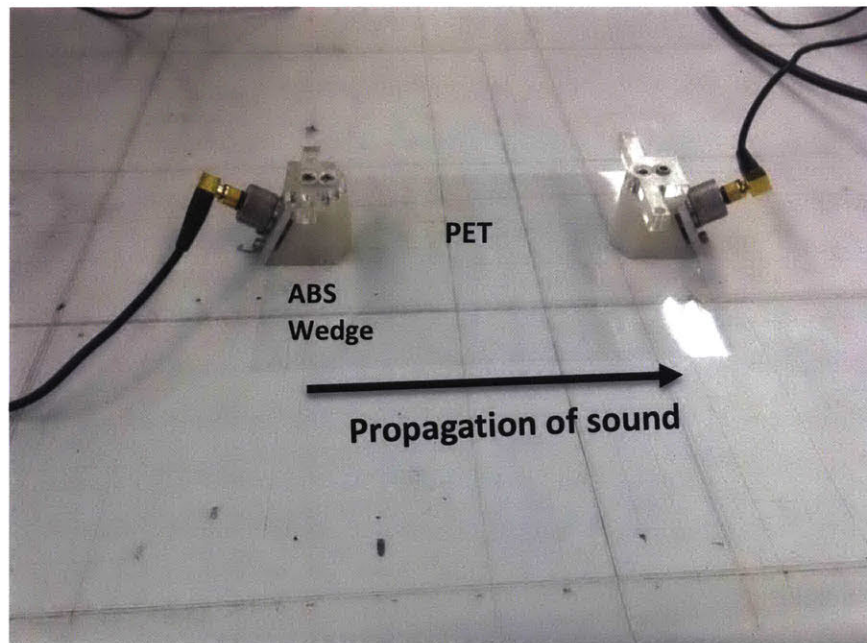
Figure 16: (a) Experimental Setup for Through Transmission Mode of Inspection and (b) Custom Designd ABS Wedge for Refraction [30]

At this point it is natural to ask why this setup did not support the production of Lamb waves in the substrate. As will be described later, Lamb waves are what are known as dispersive i.e. their velocity changes with frequency. As such, Lamb waves have two velocities associated with them: group velocity and phase velocity. While equation (4.1) can still be used, the longitudinal speed of sound in PET needs to be replaced by the desired Lamb wave group velocity. The Lamb wave group velocity in PET was <2100 m/s resulting in a Snell ratio >1. As such, there is no physically realizable angle for the ABS wedge that can support the injection of Lamb waves into the PET substrate.

The transducers used for longitudinal wave injection were 1MHz miniature screw-in Centrascan transducers (C548-SM) from Olympus. The transducers were excited and the propagating wave was captured and visualized using a combination of the DPR3000 Pulser manufactured by JSR Ultrasonics and a picoscope manufactured by Pico Technology. A schematic of the experimental setup can be seen in Figure 17.
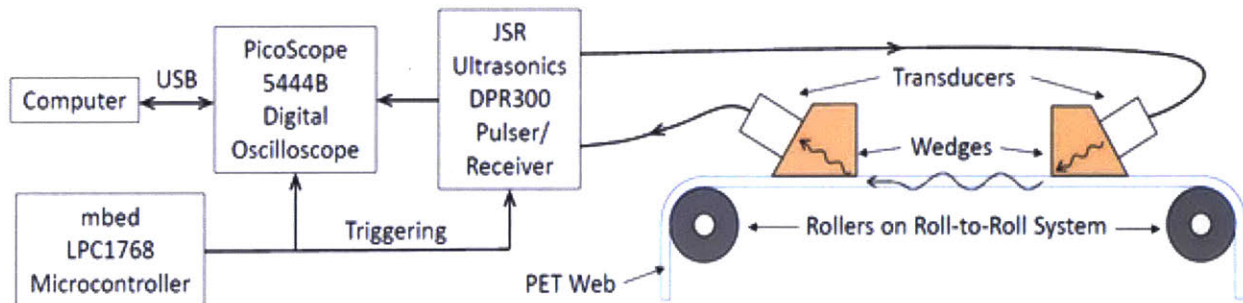
Figure 17: Data Acquisition Setup for Longitudinal Ultrasound Waves[29]

The data was captured and visualized using LabVIEW®. A schematic of the block diagram that was developed can be seen in the Appendix. Data was sampled every 8 ns (125 MHz) and typically range of time was ~80 μs.

4.3 Results

In order to ascertain the viability of using longitudinal waves to detect bulk defects, three experiments were conducted:

4.3.1 Effect of Varying Hole Sizes

Holes of five different sizes were introduced into the PET films using drill bits of pre-determined sized and their effect on the total energy contained the received signals were analyzed. We expect that the presence of holes in the path of the longitudinal waves will result in a very large impedance mismatch (air v. PET) and as such the longitudinal wave will significantly attenuate. It can be seen from Figure 18 that as the size of the hole increases, so does the attenuation in the signal. Figure 18b was generated by integrating (in time) the squared magnitude of the each signal line and referencing the integral to the integral of the undisturbed signal line; when there were 0 holes, the squared integral ratio was 1.
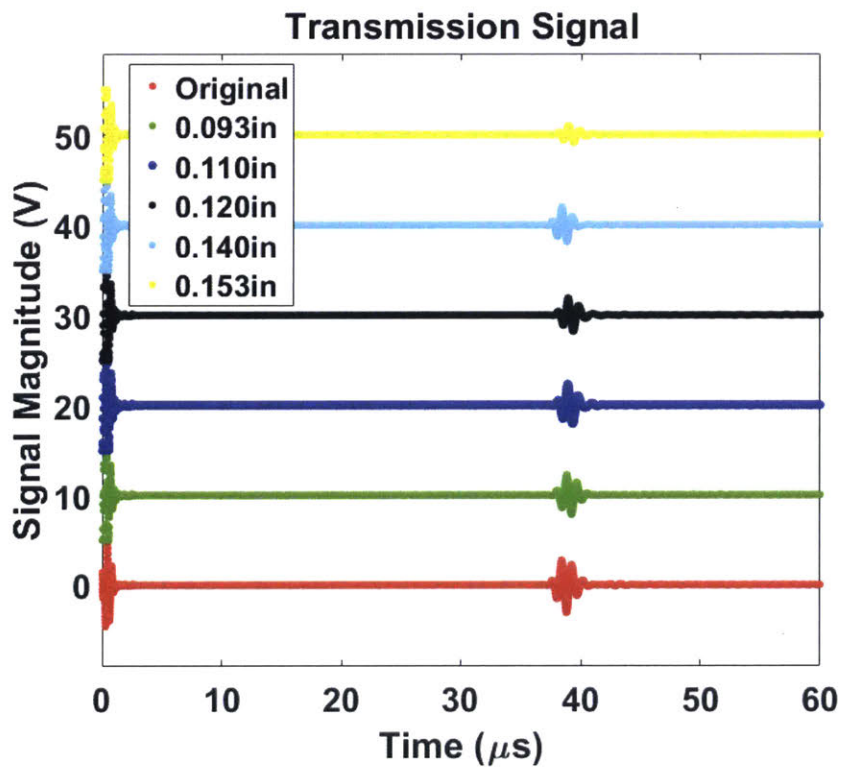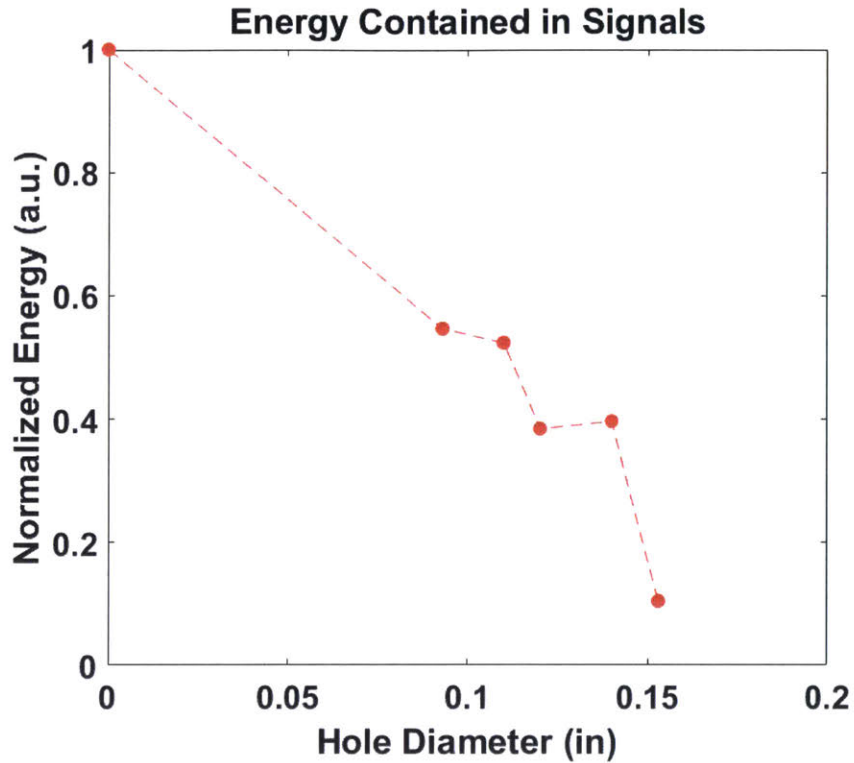
Figure 18: (a) Longitudinal Wave Signals in PET with Varying Hole Sizes (b) Effect of Varying Hole Sizes on the Attenuation of Longitudinal Waves in PET

4.3.2 Effect of Number of Deletions from Substrate

Besides geometry of the holes, the effect of frequency of occurrence of defects was also analyzed. The R2R manufacturing process will rarely have single defects within the substrate and as such, a multi-defect analysis was conducted. Up to three holes were introduced into the substrate collinearly and the behavior of the longitudinal waves was analyzed. The holes were of arbitrary size.

Once again, we expect that the presence of an increasing number of holes in the path of the longitudinal waves will result in larger and larger impedance mismatches (air v. PET) and as such the longitudinal wave should exhibit increasing attenuation. It can be seen from Figure 18 that as the number of holes increase, so does the attenuation in the signal. Figure 18b was generated by integrating (in time) the squared magnitude of the each signal line and referencing the integral to the integral of the undisturbed signal line.

It can be seen from Figure 19 that an increasing number of defects in the substrate increases the attenuation of the sound wave.

Energy Contained in Signals
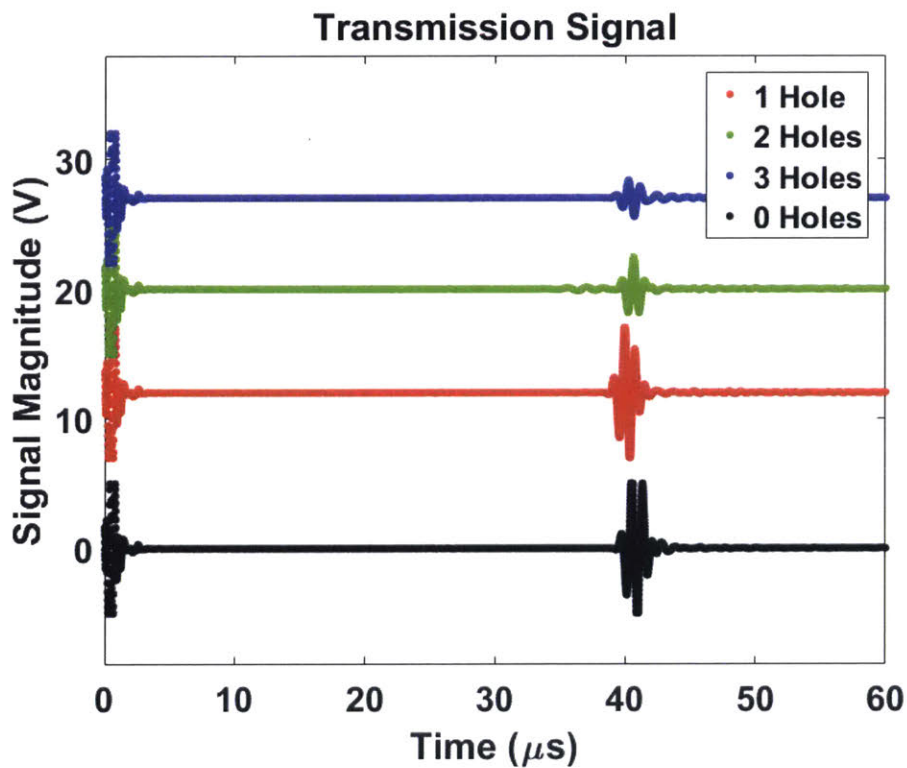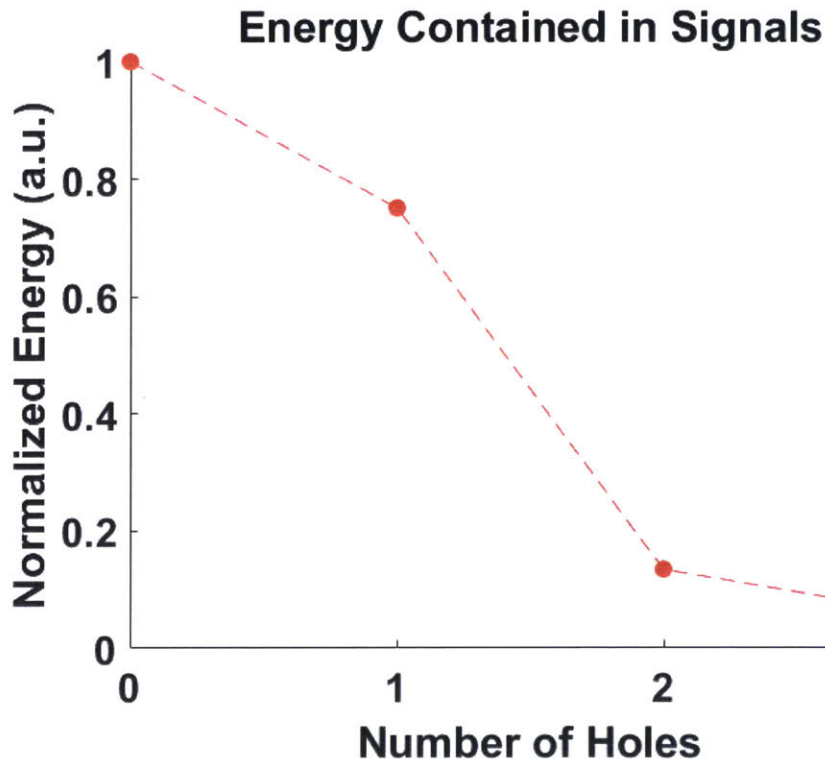
Figure 19: (a) Longitudinal Wave Signals in PET with Varying Number of Deletions (b) Effect of Varying Number of Deletions on the Attenuation of Longitudinal Waves in PET

4.3.3 Effect of Substrate Thickness

Finally, the effects of substrate thickness on the signal characteristics were analyzed. This is of important because often the substrates in the R2R process can be multi-layered or suffer from delaminations resulting in decreased thicknesses. PET films (McMaster Carr ®) of three different thicknesses were obtained and longitudinal waves were injected into them. A priori, we did not have a good hypothesis on any expected variations in the signal characteristics.

However, it can be seen from Figure 19 that increasing the thickness of the substrate makes it more difficult for sound to propagate making it a good tool for thickness measurement.

38
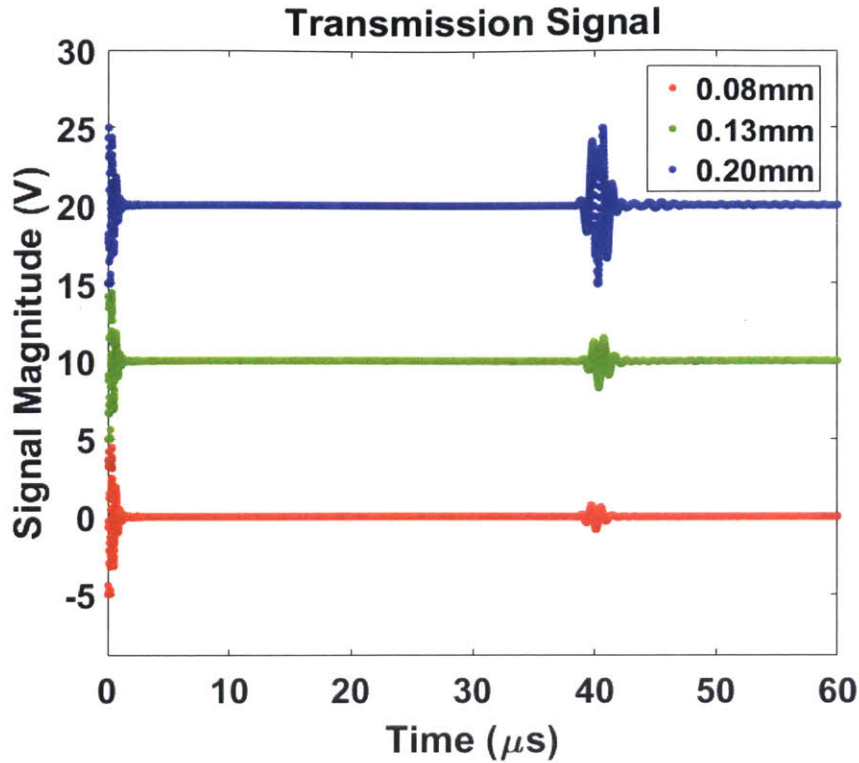
Figure 20: Effect of Substrate Thickness on Longitudinal Wave Attenuation

4.4 Longitudinal Tomographic Reconstruction

Based on the above preliminary results, we believe that defects in PET could be identified using longitudinal waves. With this mind, a full tomographic reconstruction was conducted. A 11cm x 30cm sheet of 76 μm PET film with a 2.5cm diameter hole was used as the substrate. A raster-scanning scheme was used to create transmit-receive signals along the long edge of the film in 2cm increments. The steps during the data acquisition were as follows:

1) Place firing transducer at 2cm increment.
2) Receive data at all 2cm increments on the other side of the PET.
3) Move to second 2cm increment.
4) Repeat steps 1-3 until all 2cm increments were firing sources.

A simulated visualization of the signals collected and the film can be seen in Figure 21b and 21c. Based on the collected data, a simplistic A-line map was created by summing all signals

received at a single receiver. A visualization of this together with an energy profile as a function of position can be seen in Figure 22. The plot in Figure 22a was produced using MATLAB's ® imagesc() command and essentially provides a time-varying plot of signal strength. In essence, the signal lines between 14 and 16cm show no reception along all-time points due to the presence of the hole.

The energy contained in each A-line was found was performing a simple time integral of the squared magnitude of each signal line. The plot in Figure 22b is plotting the energy contained in the signal as a function of the x-position of the PET. It becomes obvious that between 14 and 16cm there is a large drop in energy due to the impedance mismatch caused by the air gap in the 2.5cm diameter hole.

Transmission Signal
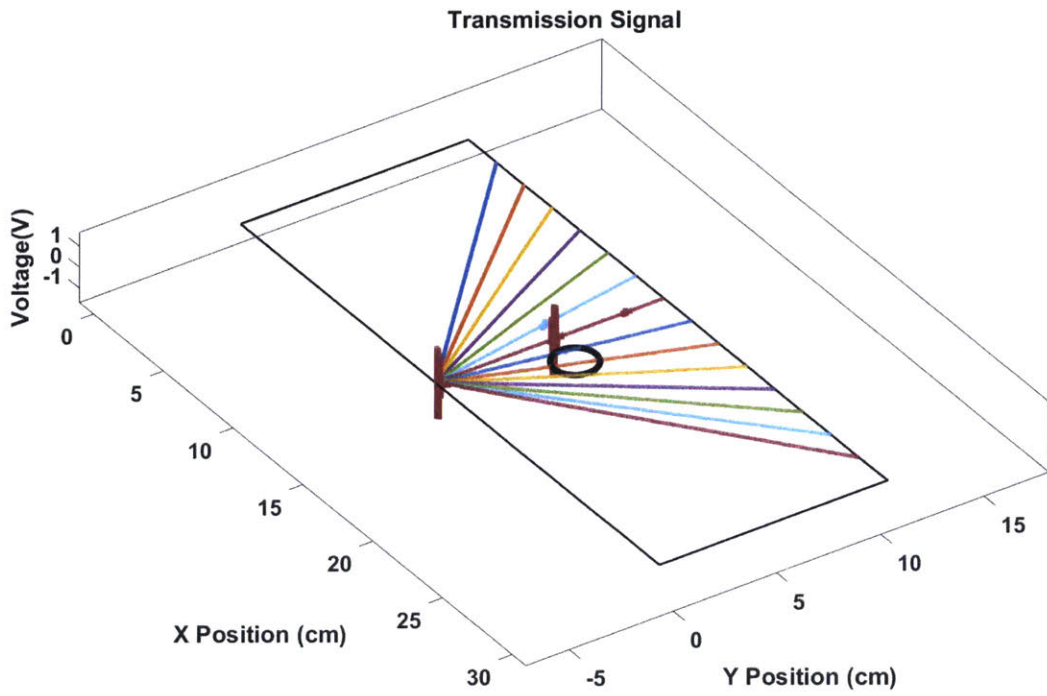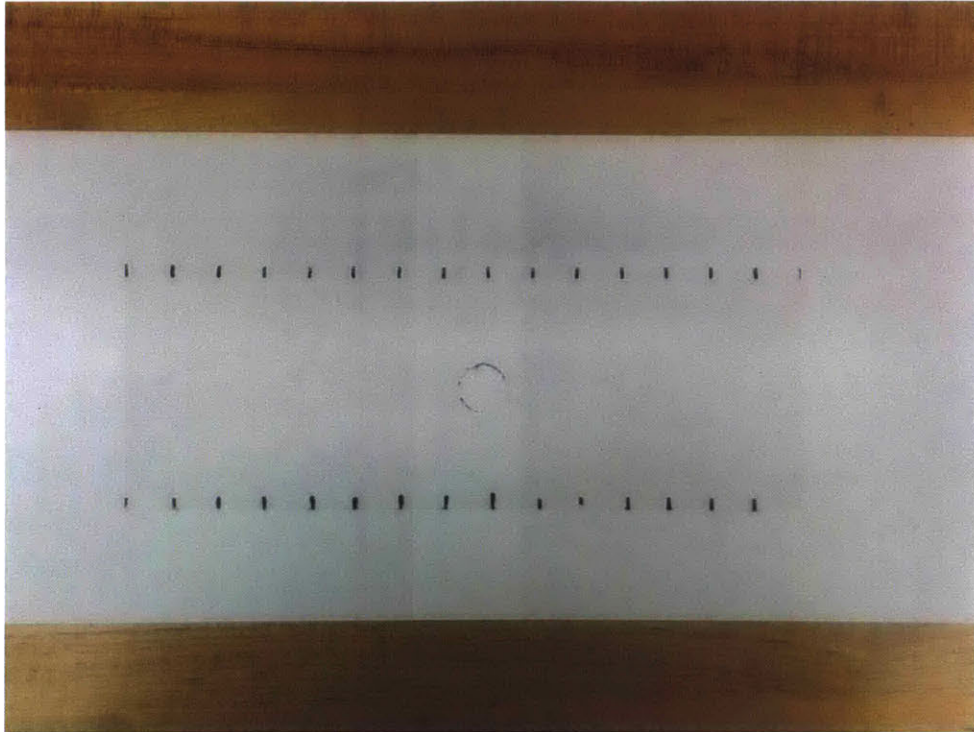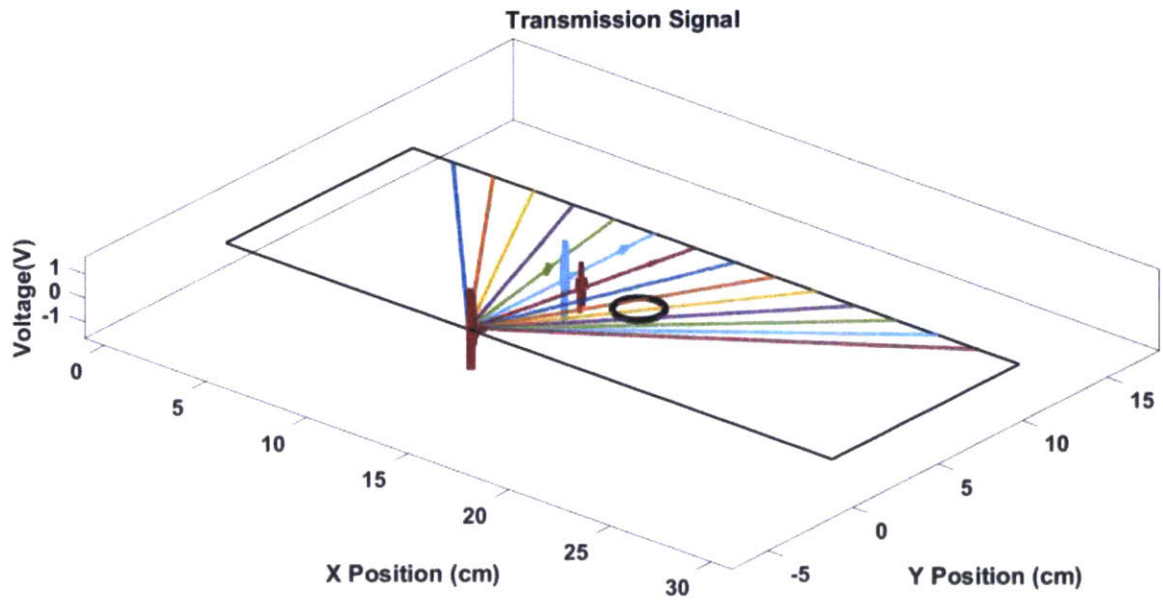
Figure 21: (a) Actual Geometry and (b) Visualization of Tomographic Scanning of PET Film with 2.5cm Hole

Visualization of Defect

Defect Detection in Polymer Film
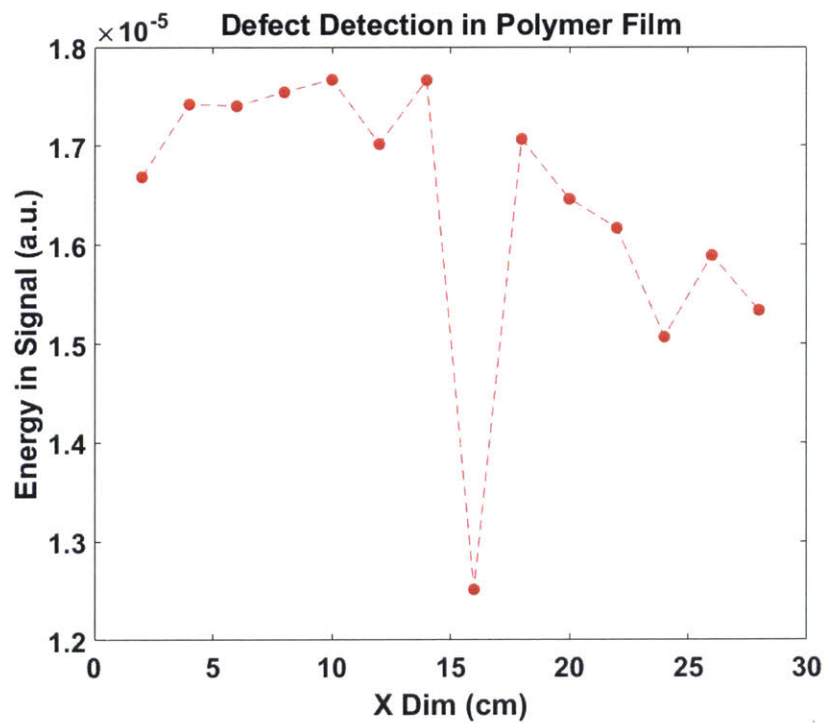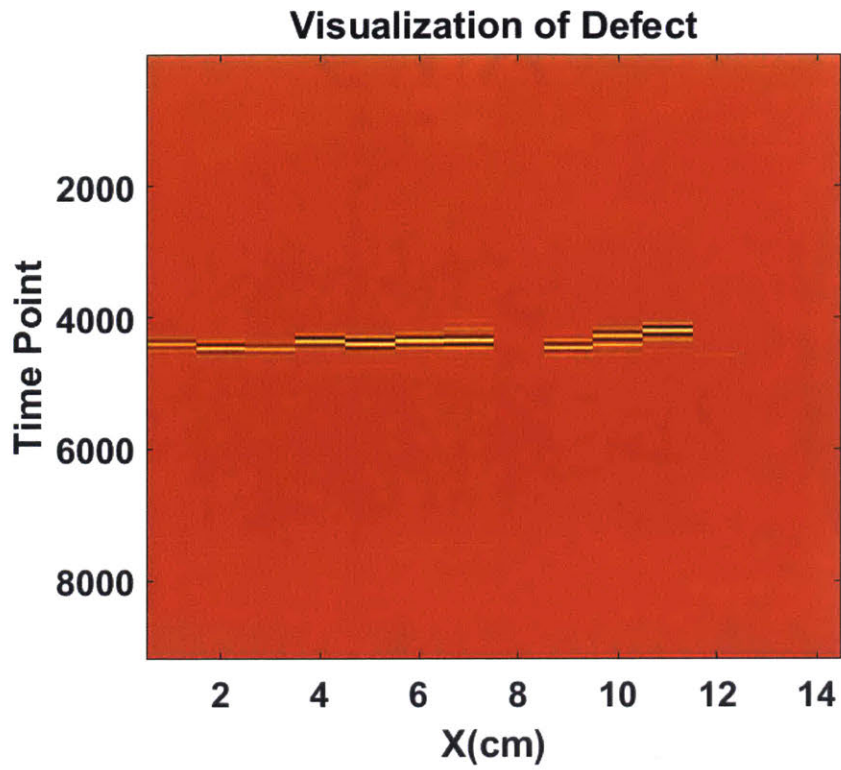
Figure 22: (a) A-Line Image Reconstruction using Longitudinal Waves of PET Film with 2.5 cm hole (b) Tomographic Energy Map of A-lines of a PET Film with 2.5cm Hole

43

Given the promising nature of the results, multiple defects with varying sizes were introduced into the film and the experiment was repeated. The exact locations, kinds, and sizes of these defects can be seen in Figure 22a, but they were as follows:

1) 0.136in diameter hole at (2, 5.2)
2) 0.086in diameter hole at (7, 3.7)
3) 0.086in diameter hole at (7, 8.5)
4) 0.196in diameter hole at (12, 2.8)
5) A slit from (4, 2.8) to (4, 1.9)
6) A slit from (10, 9.5) to (10, 8.5).

A visualization of the recreated image together with the true locations and types of defects can be seen in Figures 23a and 23b. The figures were produced using the same algorithms/techniques as before. This time unfortunately, the described method was unable to discern minute details. Given these results, advantages and disadvantage of this method can be outlined as follows:

Advantages:
1) Ability to identify large defects (order of 10mm). This was evident from the ability of this method to accurately discern the location of a 25mm diameter (hole) defect in the PET.

Disadvantages:
1) Lack of resolution in 2-D. This can be incorporated by scanning from the other direction at the expense of increased scan time. This is evident from Figure 21b because the imagesc plot does not show the vertical extents of the hole.
2) Lack of sensitivity to smaller defects (cracks were not identified). This is largely a limitation of the wavelength of the sound wave being produced. With a frequency of 1MHz and a speed of sound of ~2100 m/s, wavelengths on the order of 2.5mm are produced. As a result, cracks on the order of ~0.5mm are not identified.
2) Because the wave largely travels within the bulk of the film, visualization of surface properties is not possible. Given the nature of R2R manufacturing products, analyzing surface features is critical.

44

3) Inability to distinguish between multiple defects resulting in a more large-scale damage assessment as opposed to localized damage assessment.

4.5 Conclusions

The following can be concluded from these experiments:

1) This setup does not support the injection of Lamb waves into PET.

2) Longitudinal waves in PET are sensitive to the presence of inclusions, thickness variations, and count of inclusions.

3) Longitudinal tomography can be used to discern single co-ordinate locations of defects on the order of ~10mm.

4) Longitudinal tomography at 1MHz cannot provide bi-dimensional tomography for defects on the order of <5mm.

Transmission Signal

Visualization of Defect
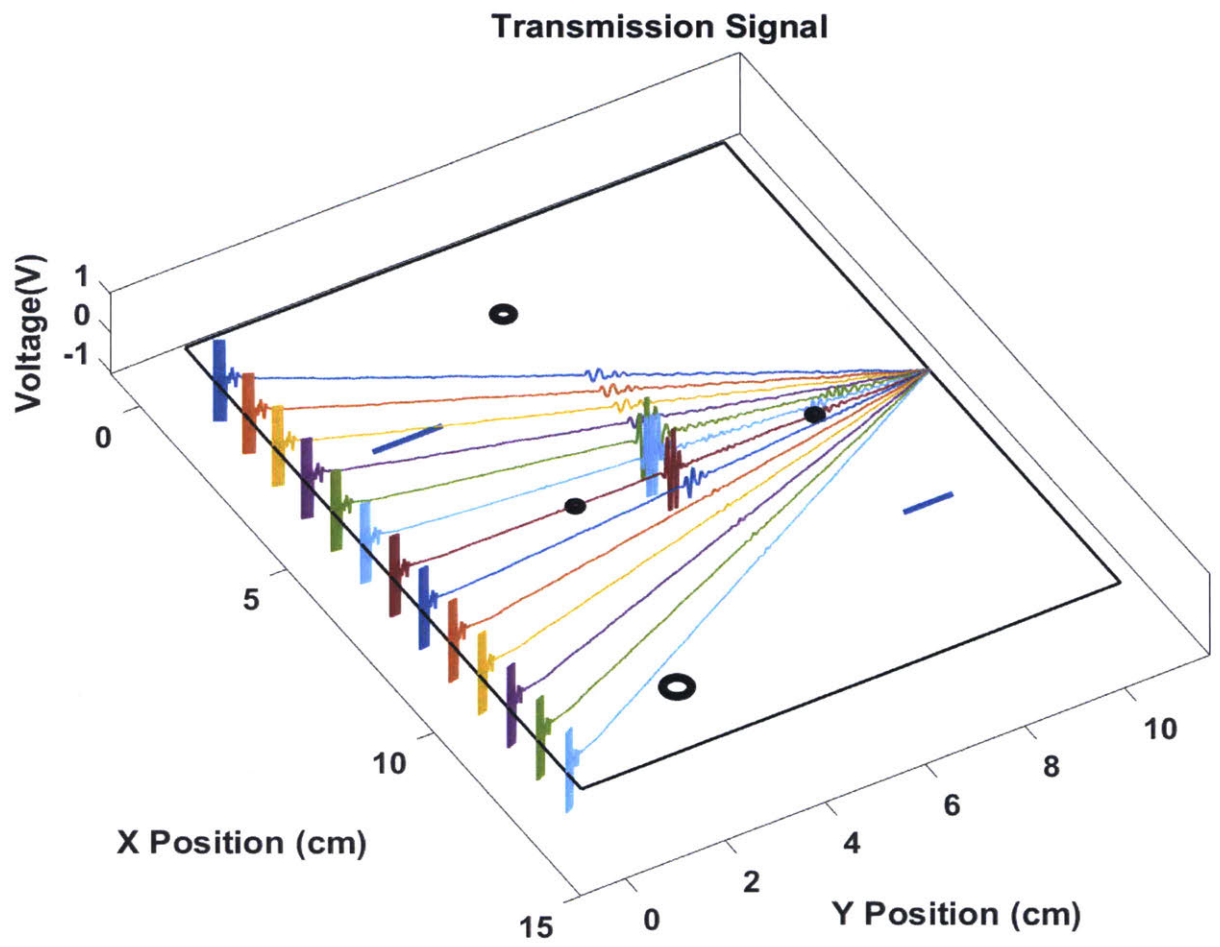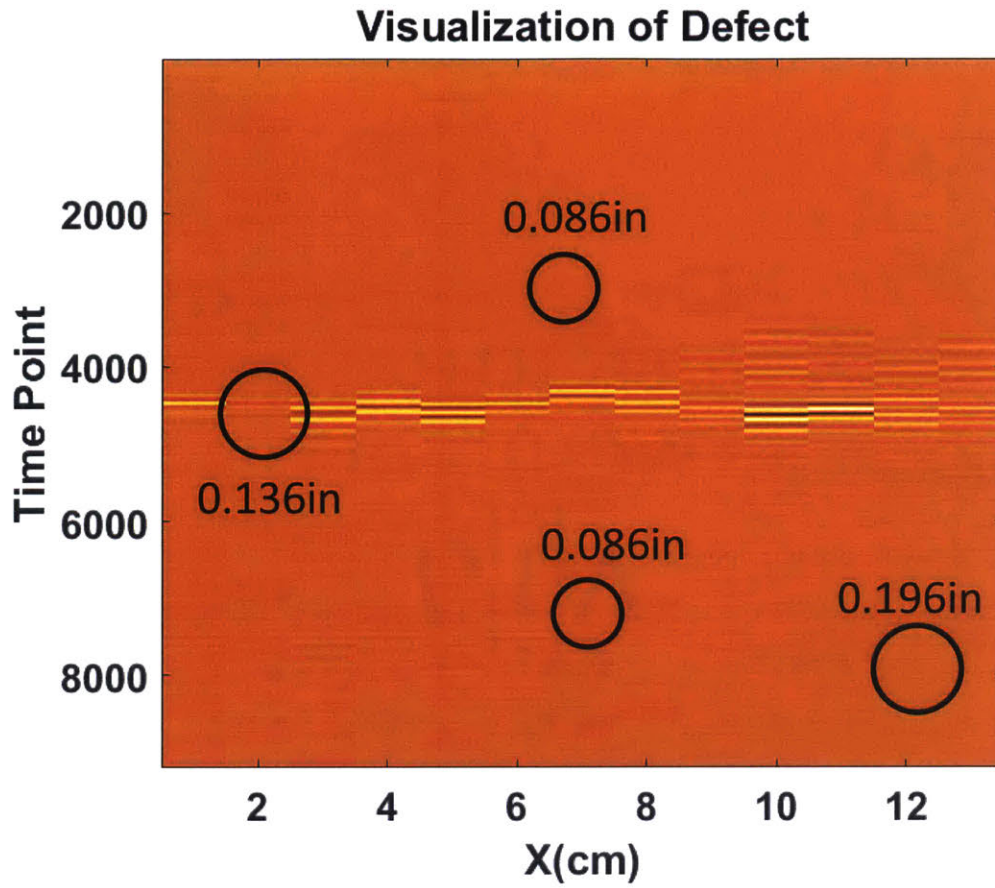
Figure 23: (a) Visualization of PET with a Combination of Cracks and Holes (b) Tomographic Reconstruction of PET Film with Varying Defects

5

LAMB WAVE

5.1 Introduction

This section will expand upon the idea of using a special kind of ultrasonic wave known as Lamb waves to probe surface and bulk characteristics of R2R substrates. This section will develop the equations governing the propagation of Lamb waves in isotropic stress-free substrates, model the propagation of Lamb waves using commercially available software packages, and prove the viability of using these waves for generating tomographs of R2R substrates.

5.2 Lamb Wave Theory

Given that longitudinal waves suffer from low sensitivity and are unable to identify the presence of surface features, a different kind of wave was explored—Lamb Waves. Elastic solids have the ability to sustain the presence of a number of different kinds of sound waves. A schematic of this can be seen in Figure 24:
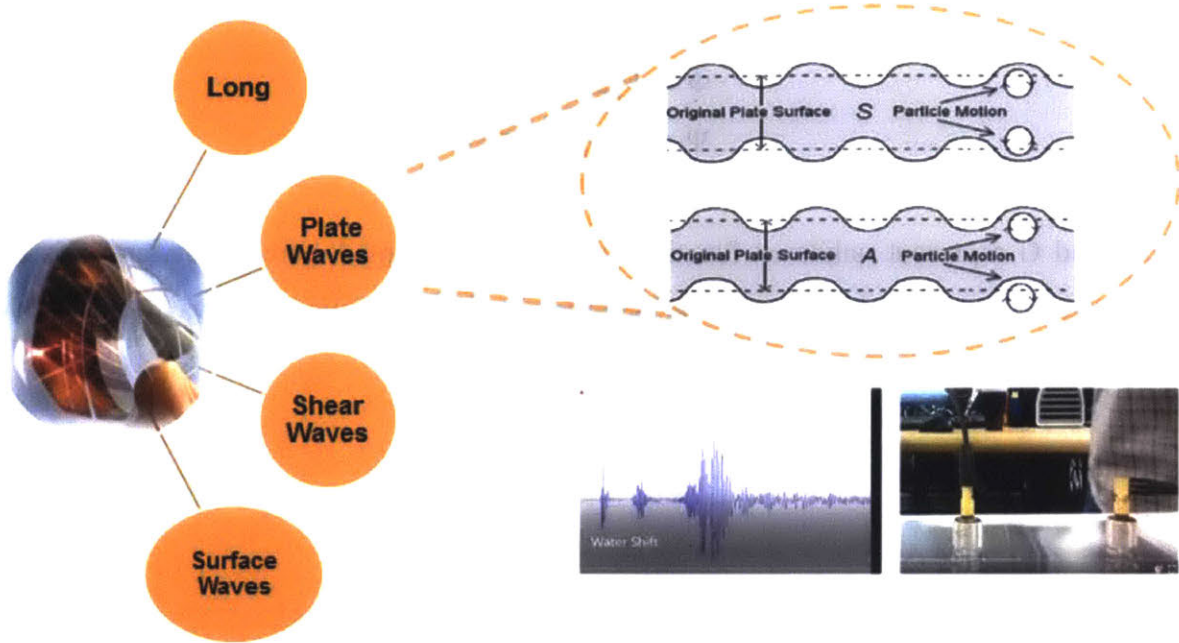
Figure 24: Ultrasonic Wave Forms Possible in Solids with a Focus on Lamb Waves

One such wave form, known as plate waves or Lamb waves, travel within the boundaries of thin plates/films. Unlike longitudinal waves, these waves are transverse waves and while the wave propagates parallel to the plate, the particles move orthogonal to the wave. The particles interact with the boundaries of the film as well as the bulk of the film. The elastic wave equation describing the behavior of the particles of the medium can be seen below [36]:

$$\rho \ddot{u} = f + (\lambda + 2\mu)\nabla(\nabla.u) - \mu \nabla \times (\nabla \times u) \qquad (5.1)$$

Here ρ is the material density, u is the displacement vector, f is the driving force, and λ and μ are Lame parameters which parametrize the elastic moduli for isotropic homogenous media. Using Helmholtz decomposition [32], the displacement vector can be expressed as

$$u = \nabla\Phi + \nabla \times \Psi \qquad (5.2)$$

where Φ is the scalar potential and Ψ is the vector potential. Assuming a plate of thickness d in the z direction infinitely extending in the x and y directions, the following sinusoidal equations can be used along with the Helmholtz decomposition [31] to solve the wave equation:

49

$$\Phi = F(z)e^{i(\omega t - kx)} \tag{5.3}$$

$$\Psi = G(z)e^{i(\omega t - kx)} \tag{5.4}$$

Here, F and G represent unknown functions of z, ω is the angular frequency, and t is time. Applying zero-stress boundary conditions, the following characteristic Lamb wave equations can be derived:

$$\frac{\tan\left(\frac{\beta d}{2}\right)}{\tan\left(\frac{\alpha d}{2}\right)} = -\frac{4\alpha\beta k^2}{(\beta^2 - k^2)^2} \tag{5.5}$$

$$\frac{\tan\left(\frac{\beta d}{2}\right)}{\tan\left(\frac{\alpha d}{2}\right)} = -\frac{(\beta^2 - k^2)^2}{4\alpha\beta k^2} \tag{5.6}$$

These are the governing equations for the symmetric and anti-symmetric modes respectively. Here $\alpha^2 = \frac{\omega^2}{c_l^2} - k^2$, $\beta = \frac{\omega^2}{c_t^2} - k^2$, c_l is the longitudinal speed of sound in the medium, c_t is the shear wave velocity of sound, c_p is the Lamb wave phase velocity and k represents the wavenumber $(k = \frac{\omega}{c_p})$.

Something very important to note from these equations is the frequency dependence of the wave speed. Lamb waves are what are known as dispersive and as such their velocities change with frequencies. Of particular note are the phase and group velocities of Lamb waves. A schematic highlighting the differences in these velocities and the frequency dependence for a 76 μm aluminum film can be seen in Figure 25. The phase velocity of a Lamb wave is the rate at which the amplitude of the wave packet changes whereas the group velocity is the rate at which the wave packet moves through the medium.

The phase velocities, and therefore group velocities, are calculated using numerical root finding methods [37].
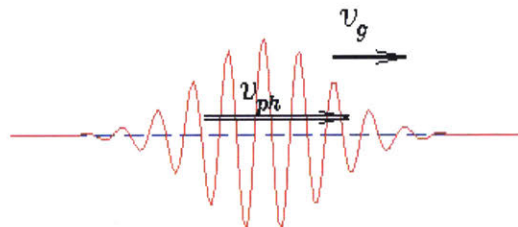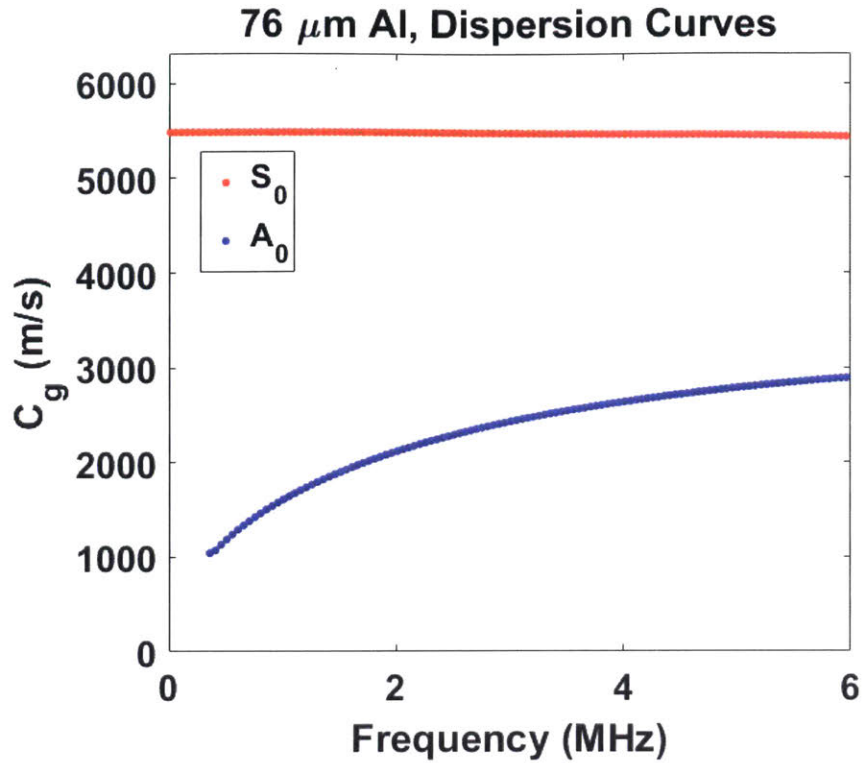
Figure 25: (a) Visualization of Group and Phase Velocities of Lamb Waves (b) Dispersion Curve for 76 μm Al Film

In addition to moving orthogonal to the direction of wave propagation, it can be seen from Figure 24 that the particles can travel in two modes:

Symmetric: Particles along the boundaries of the thin film move together and away in sync creating a plane of symmetry mid-way into the depth.

Antisymmetric: Particles along the boundaries of the thin film move in the same direction creating a plane of anti-symmetry in the film.

Regardless of the kind of Lamb wave being produced within thin films, they hold the promise of being able to characterize not just bulk features, but also surface variations.

5.3 Modelling Lamb Waves in k-Wave®

Once the theory behind Lamb waves was understood, the first step towards developing a means for non-destructively examining substrates was determining the viability of the capabilities of Lamb waves as they relate to identifying bulk and surface features. Numerical simulations using the commercially available software kWave® were implemented. A PET film with thickness of 80μm and 8cm x 20cm area was used as the test surface. A 10-cycle Hanning burst with input characteristics seen in Figure 25 was applied at one end on the surface of the film and data was recorded 2.56cm (21 grid points) away from the source on the surface of the film. The simulation represented a stress-free film of polymer subject to an orthogonal time varying point load. The entire k-wave® code used is attached in the Appendix and can be referred for replicating the results.
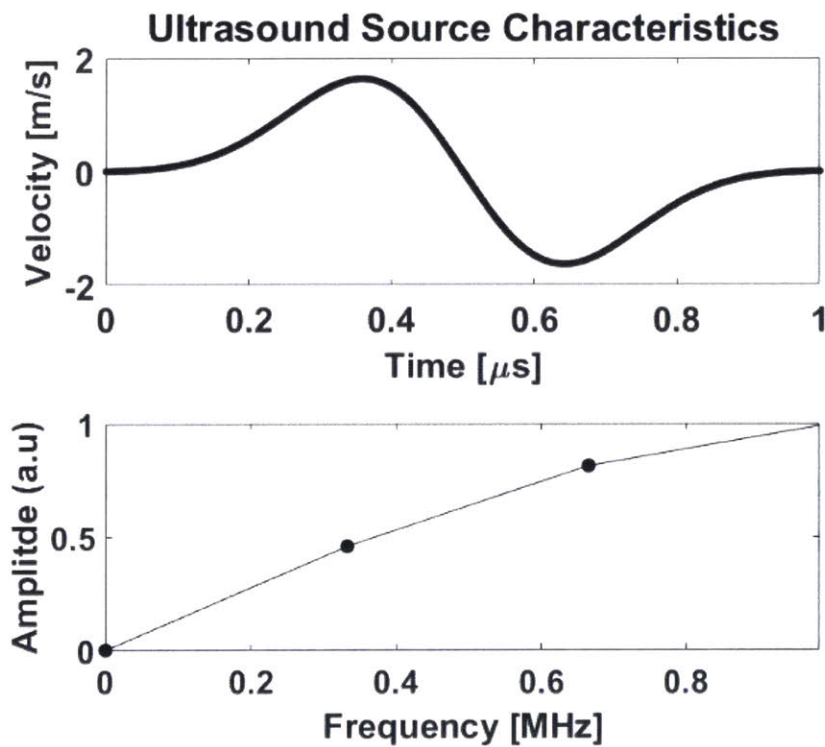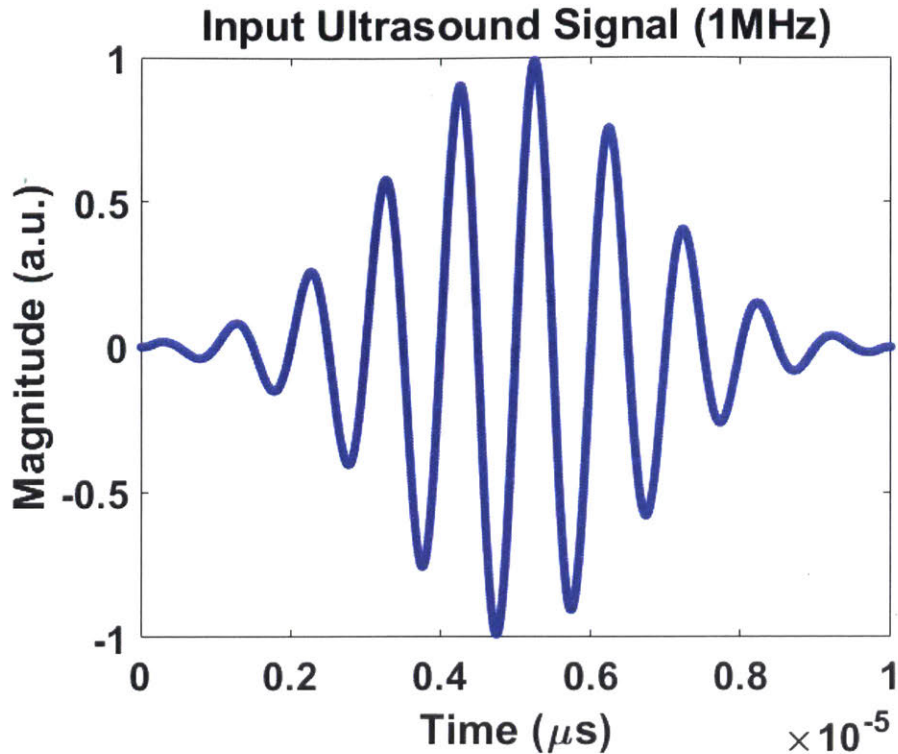
Figure 26: (a) 10-Cycle Hanning Window used to Model k-Wave Transducer (b) k-Wave Input Signal Characteristics

A visualization of the geometry of the setup can be seen in Figure 27. The transducer was modeled as a point load with a center frequency of 1 MHz This was chosen to mimic the Olympus transducer in the lab which also had a center frequency of 1MHz. Properties of the medium were set as follows:

Density: 1380 kg/m^3

Speed of Sound (Longitudinal): 2400 m/s

Attenuation coefficient (dB/ MHz cm): 0.33

Attenuation Power (y): 1.1

Using these parameters, the simulation was successfully run. A time varying pressure field in the on the surface of the film was computed and can be seen below. As seen in Figure 28, the wave propagates as expected with a circular wave front traveling across the surface of the PET; however, looking at the time the signal that is received (~10 μs) it becomes obvious that the

53

received signal is a longitudinal wave and not a Lamb wave. Based on a group velocity of 1530 m/s, the 0th order symmetric Lamb wave (S_0) wave (fastest possible mode) would have arrived at ~14 μs.

Furthermore, the frequency-time decomposition of the signal indicates the reception of only a longitudinal pulse (L) and no 0th order Symmetric (S_0) and 0th order anti-Symmetric (A_0) waves. In light of these simulations, it was concluded that k-wave was inadequate at developing Lamb wave simulations and a full FEM tool was required: ABAQUS®.
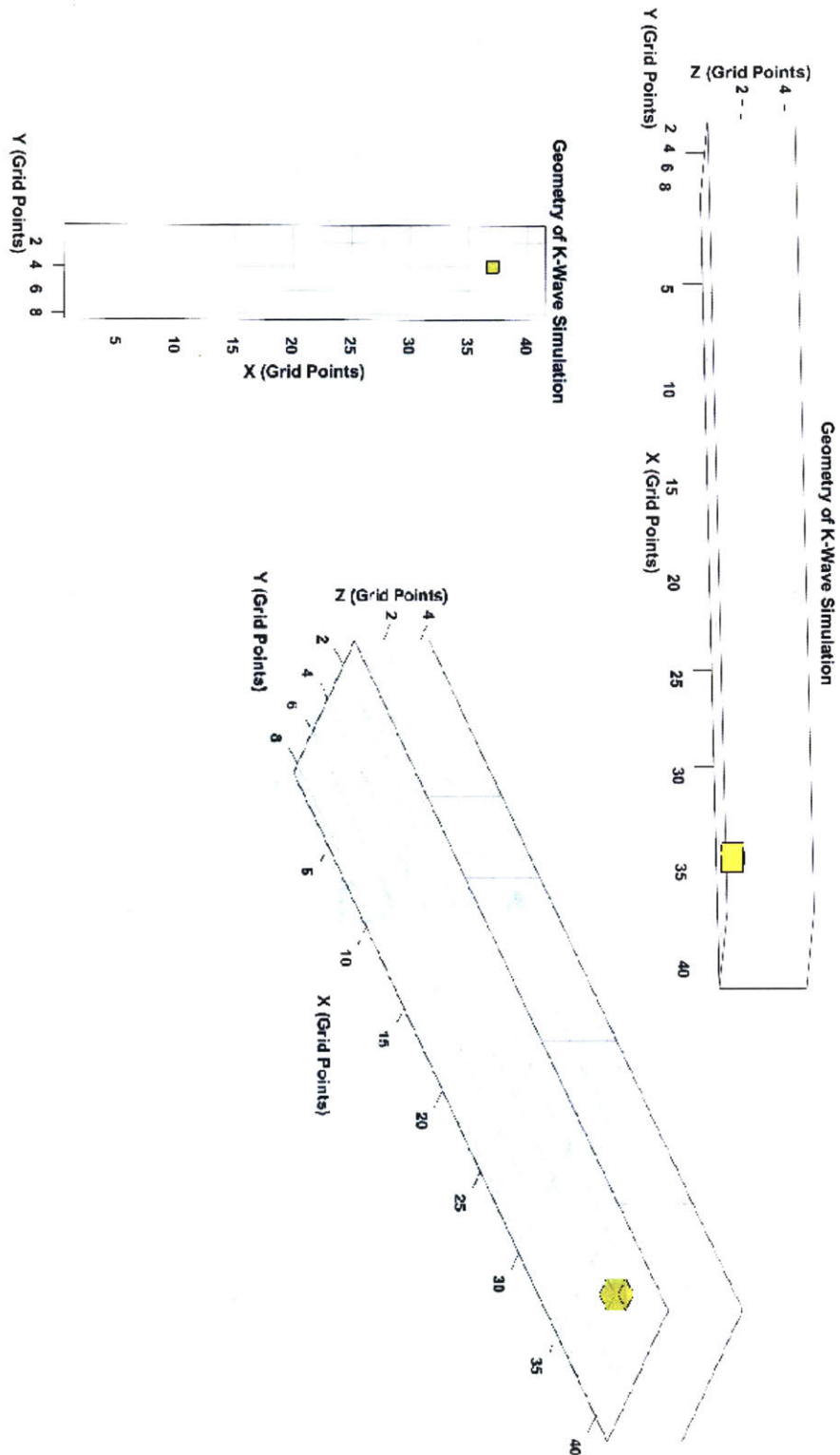
Figure 27: Visualization of k-Wave® Grid Geometry Representing an 80 micron PET Film with transducer (yellow) on surface
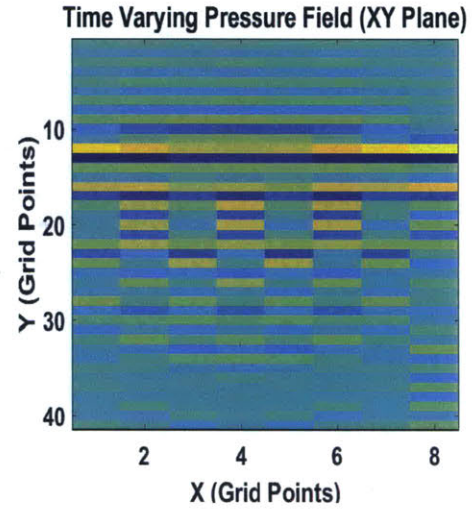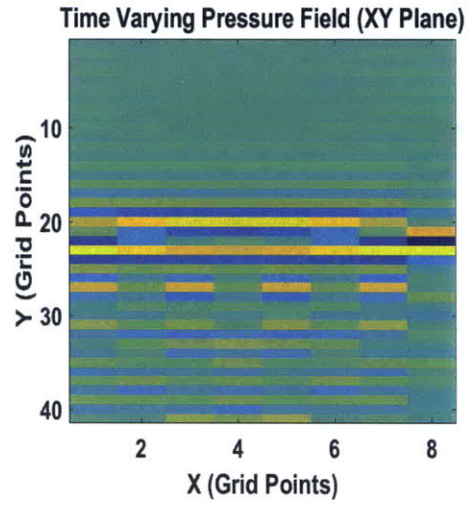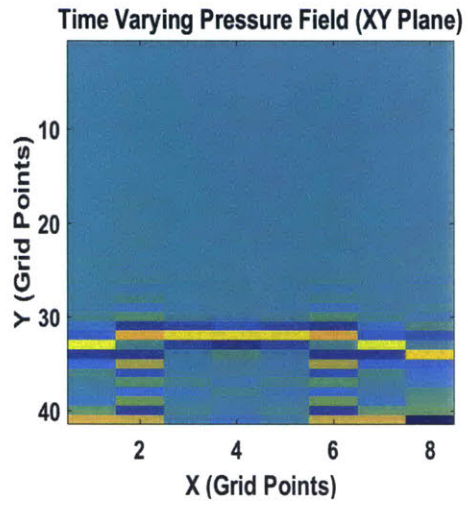
Figure 28: Time Varying Pressure Field on the Surface of the PET Film Simulated in k-Wave®

56

Frequency Time Decomposition for 1.0079" Spacing in PET
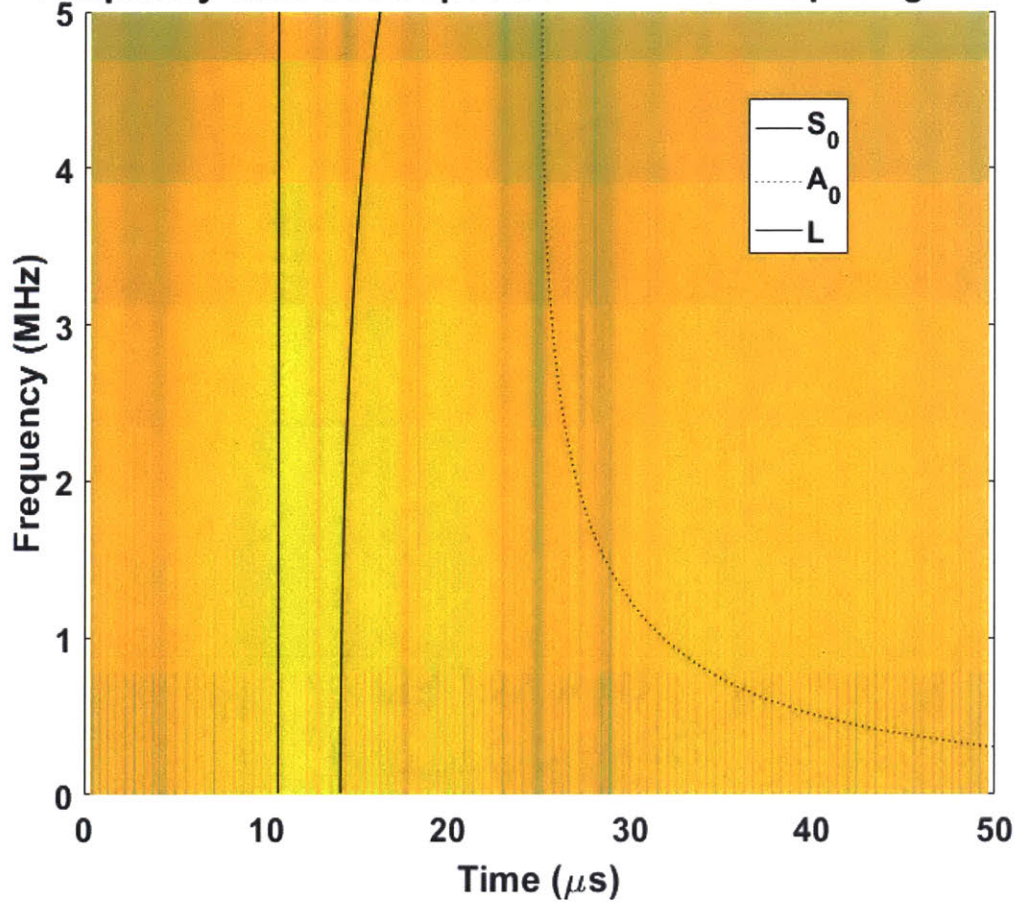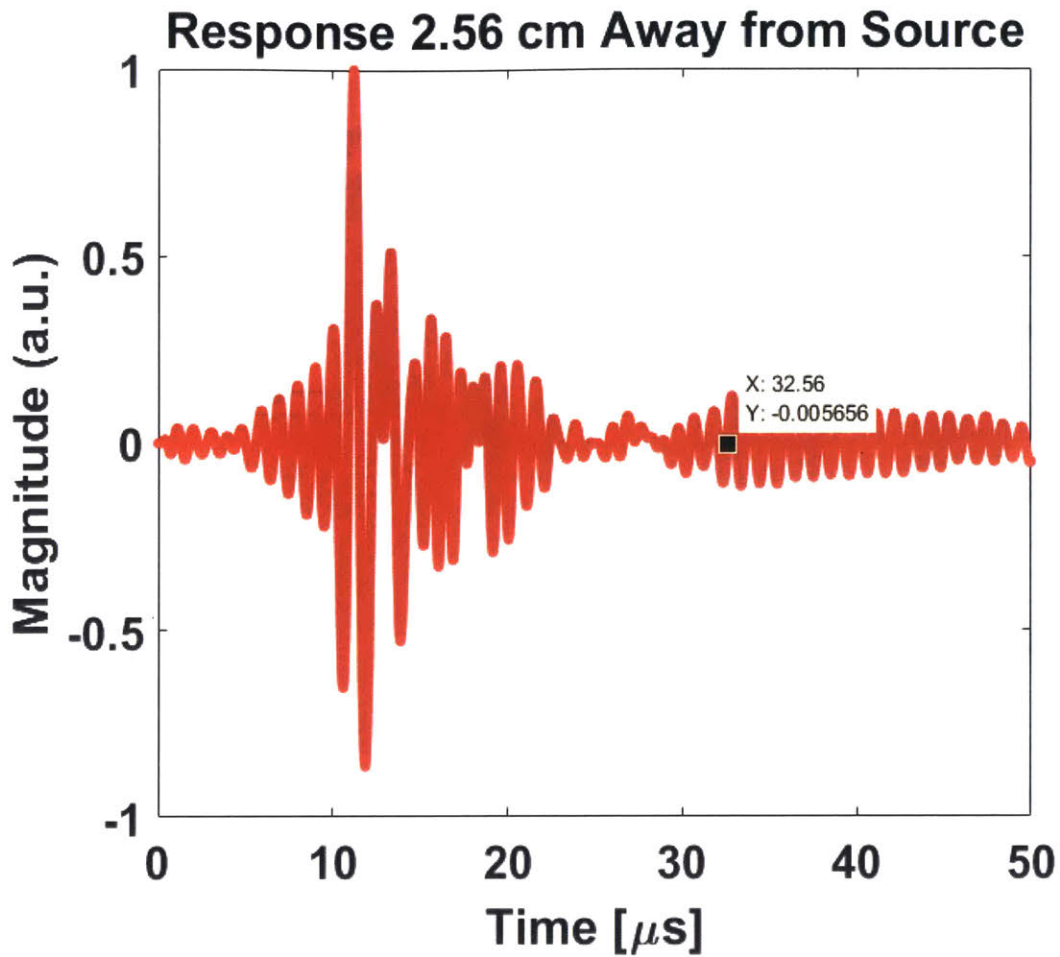
Figure 29: (a) Frequency-Time Decomposition of Received Signal Using k-Wave® 2.56cm from Source (b) Signal Received 2.56cm from Source during Simulation

5.4 Modelling Lamb Waves in ABAQUS®

Given that k-wave® was unable to model the propagation of Lamb waves in PET, a finite element approach was implemented. A 76μm thin film of aluminum (easier to generate Lamb waves in) was modeled in ABAQUS®. A five cycle Hanning window pulse with a center
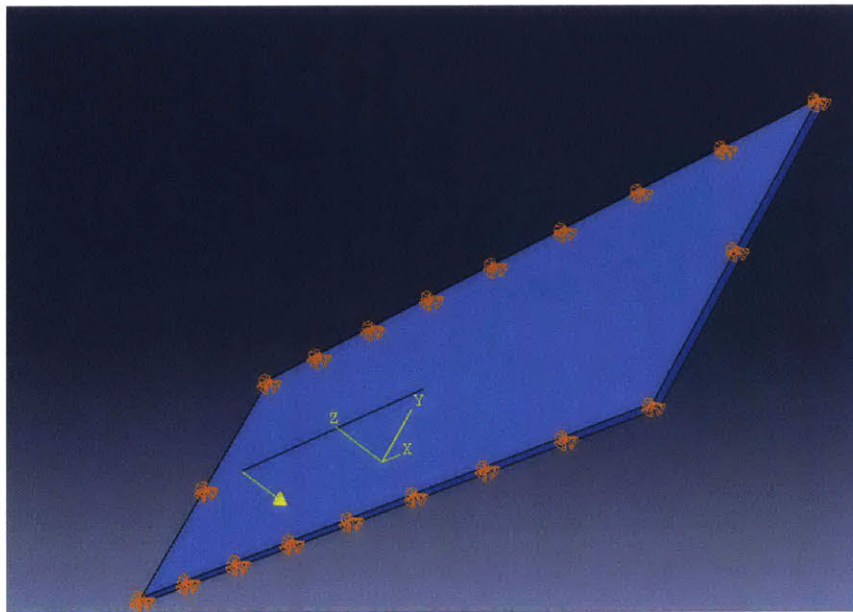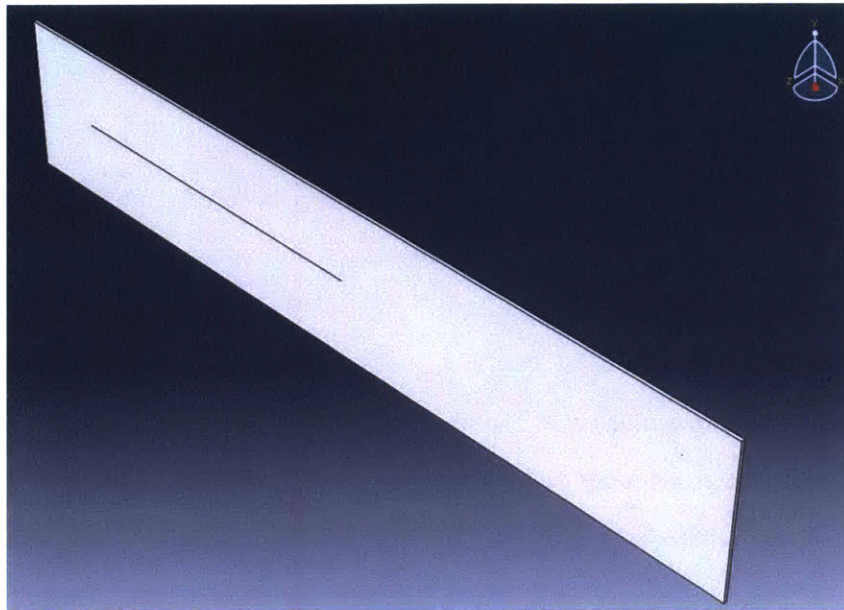
Figure 30: (a) Zero Displacement Boundary Conditions on all Edges of Aluminum Plate (b) Schematic of the Geometry under Analysis

frequency of 1 MHz was applied onto the surface of the film (2700 kg/m^3, 69 GPa, 2cm x 11.5cm) as a point load. In order to replicate true physical conditions, the edge surfaces of the

plate were assigned to have zero displacement. Schematics of the geometry and boundary conditions can be seen in Figure 30.

The input waveform to the plate can be seen in Figure 31. Once the model was setup, two different situations were analyzed:

- *Wave Characteristics with a 2mm Hole:* A 2mm hole was introduced in the film along the path between the transducer and receiver. Schematics of the geometry can be seen in Figure 32.

- *Wave Characteristics with a 0.25mm Crack:* A 0.25mm crack was introduced along the path between the transducer and the receiver in a direction orthogonal to the propagation of the flow of the wave. Schematics of the geometry can be seen in Figure 32.
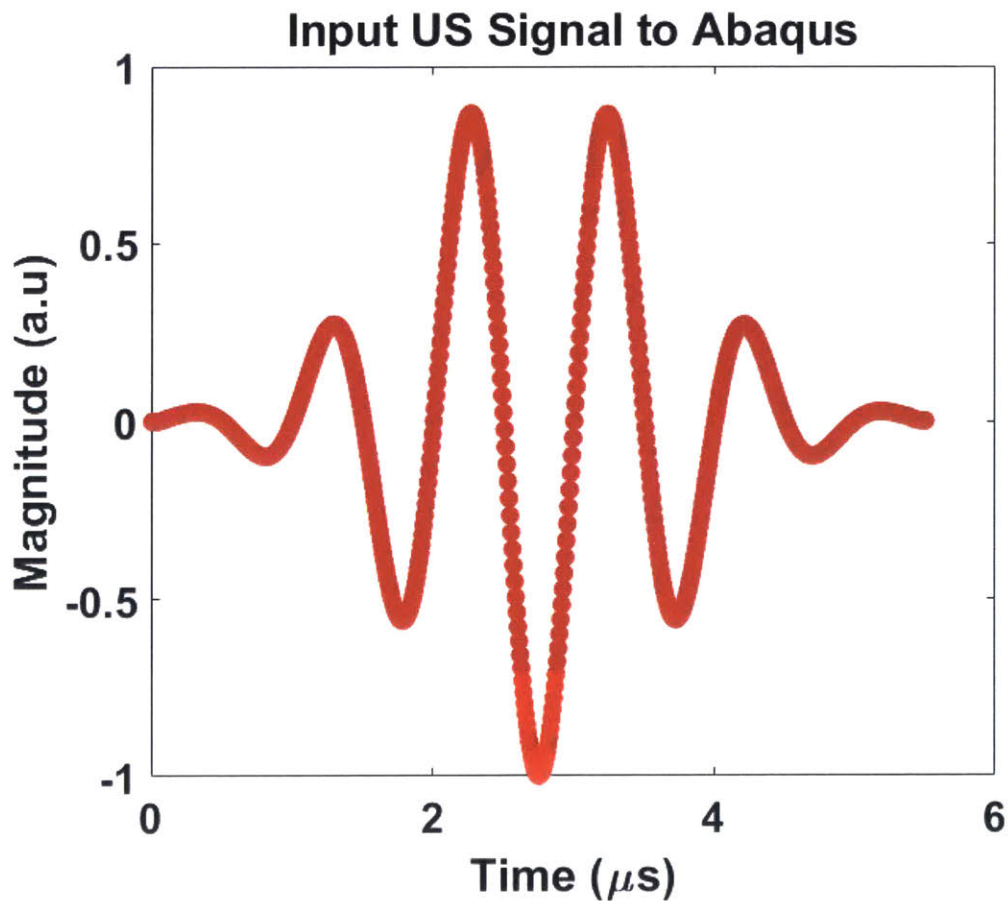
Figure 31: Input Waveform into ABAQUS® Simulation
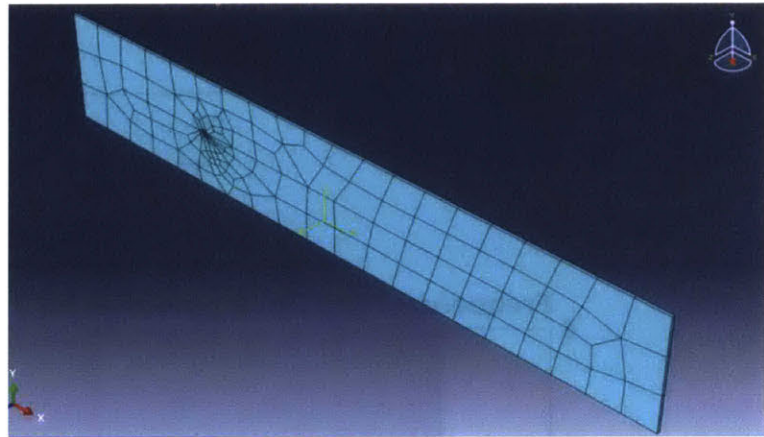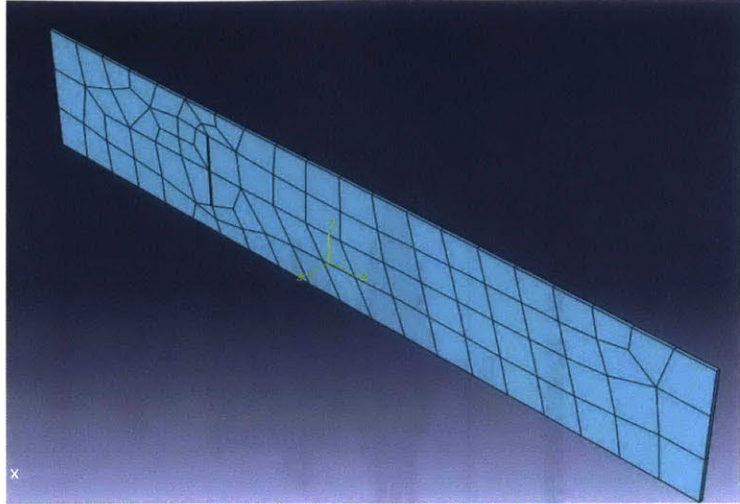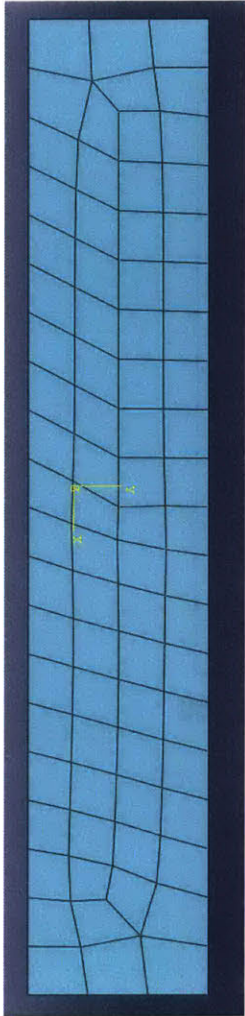
Figure 32: ABAQUS Simulation of Aluminum Film of (a) Original Mesh (b) Mesh with a 0.25mm Crack (c) Mesh with a 2mm Hole
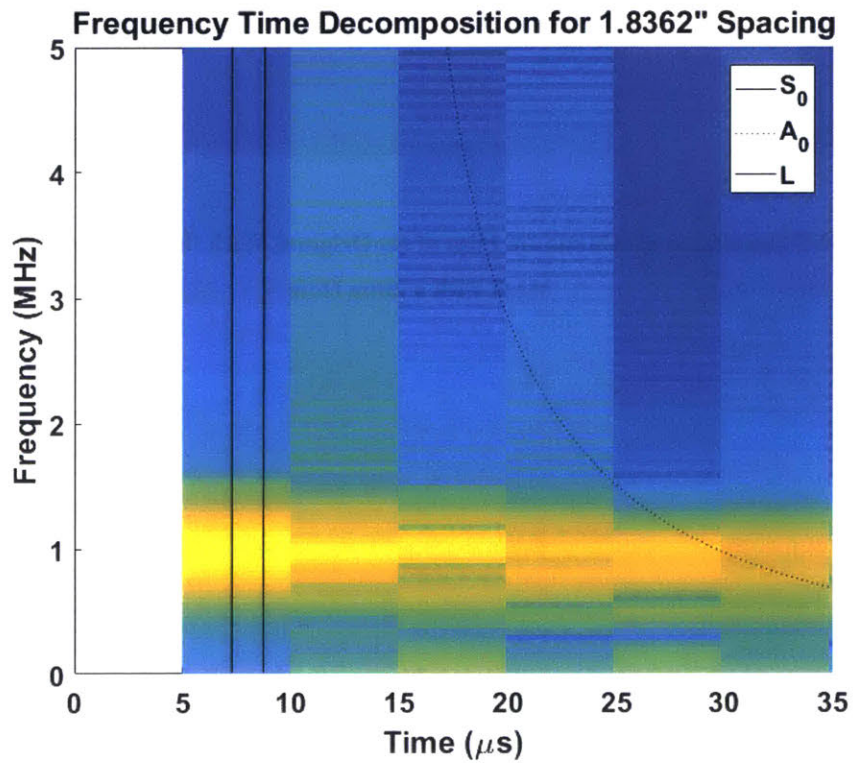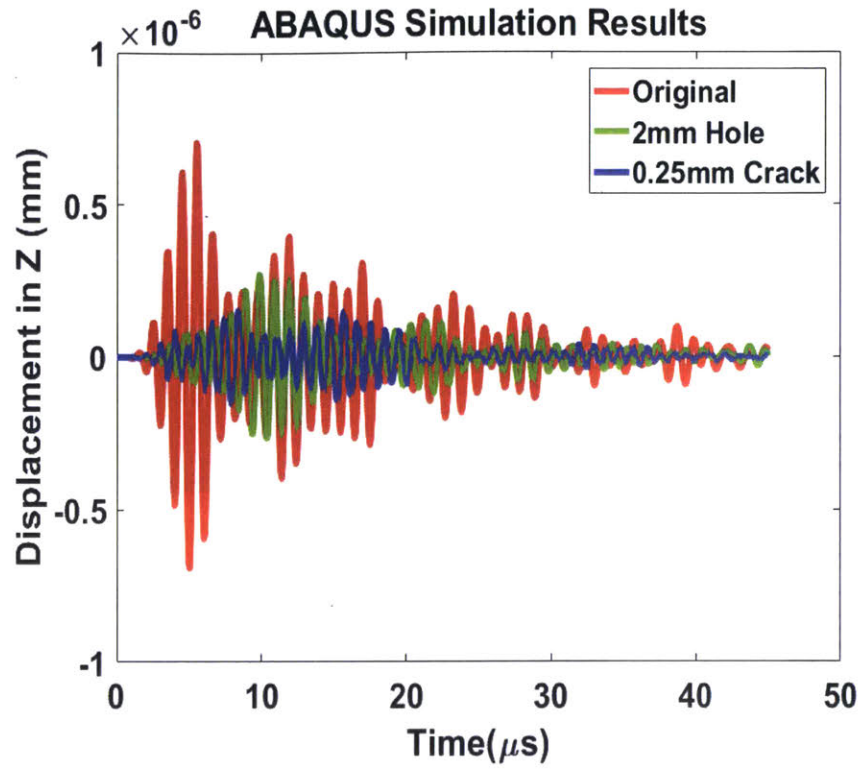
Figure 33: Simulated Proof of Lamb Wave Generation and Interaction in Aluminum

The time duration simulated was 45μs and the signal was measured on the surface of the film at a distance of 4.6cm away from the transducer. In order to ascertain that the waves being produced were indeed Lamb waves, a frequency-time decomposition was performed on the original signal and can be seen in Figure 33. It is evident that not only was a longitudinal pulse detected, S_0 and A_0 modes were also detected. Most importantly, one can observe that the amplitudes of all three waves were affected by the presence of defects. The undisturbed wave (red) exhibits higher amplitudes at all time points than the blue and green signals. This result proved that in a thin film of aluminum, Lamb waves could be generated and that they could be used to probe bulk defects in thin films.

While it is important that Lamb waves be sensitive to bulk defects on the order of a few mm's, the additional hypothesized benefit of this technique lies in its ability to interact with and therefore reveal additions and features. In order to evaluate if this is indeed the case, the 1 MHz transducer was used to excite a 76μm film of Aluminum and the Lamb waves were observed in the presence of water droplets on the surface. From the sequence of images seen in Figure 34, we see that the amplitude of the Lamb wave, specifically the A_0 mode, varies in the presence of water drops and returns to the original configurations when the surface if cleared of any additions. The time of arrival of the two blips seen along the signal confirm that these are indeed the 0th order symmetric and anti-symmetric Lamb waves.

5.5 Conclusions

The results in this section show that:

1) 0th order symmetric and anti-symmetric lamb waves can potentially be created and propagated through 76 μm aluminum films.

2) The Lamb waves are potentially sensitive to bulk defects on the order of ~1-2mm.

3) The Lamb waves are potentially sensitive enough to interrogate surface features
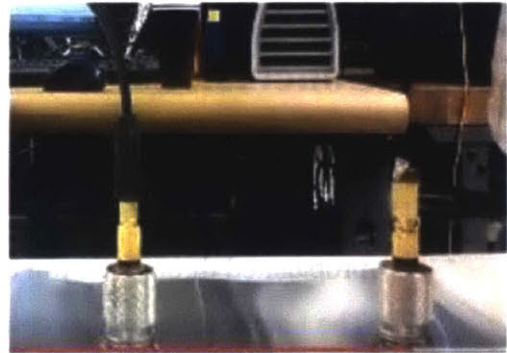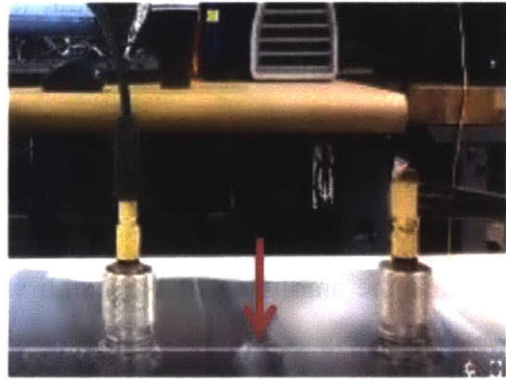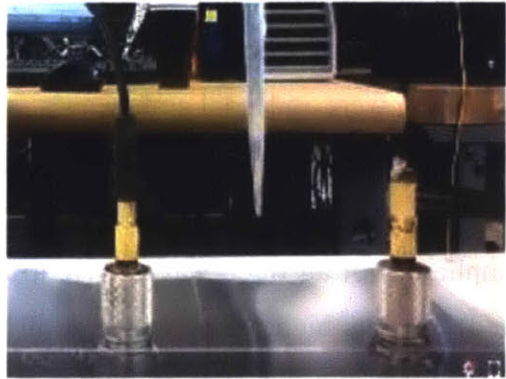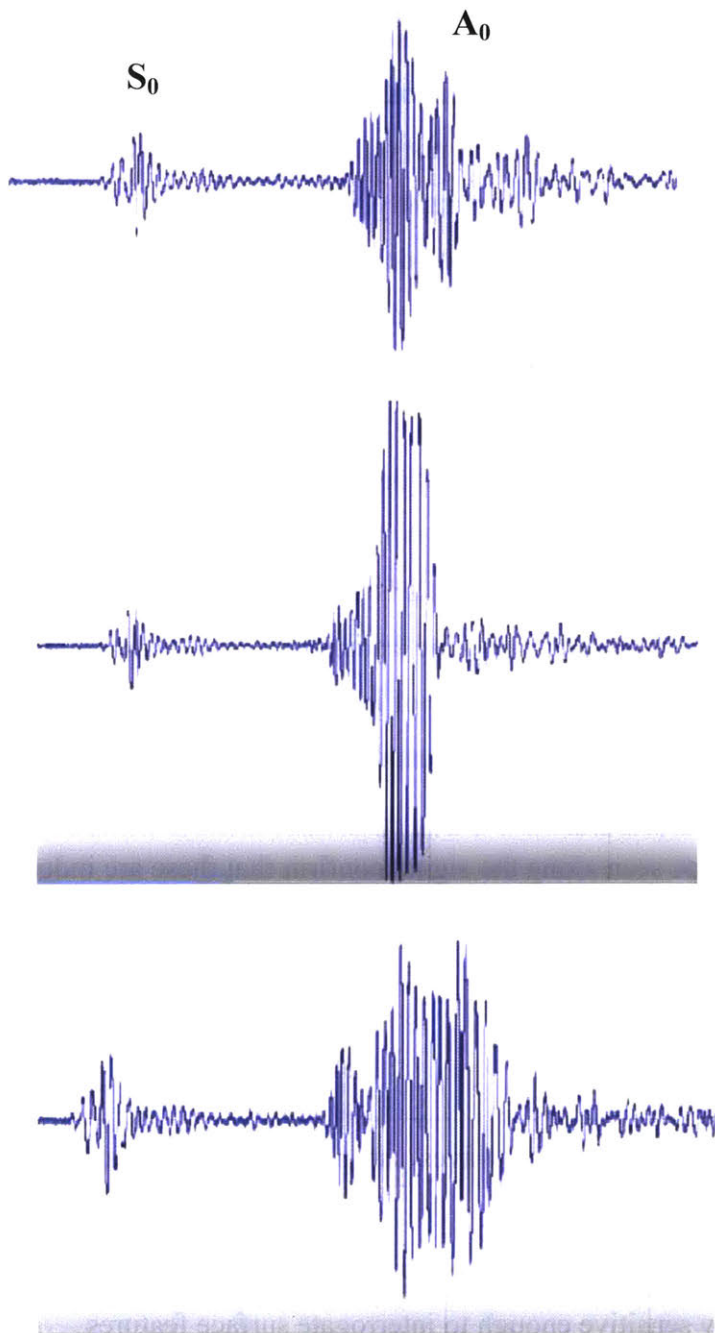
Figure 34: Sensitivity of Lamb Waves to Surface Features (Water Drops)

6

AREA OF LAMB WAVE INFLUENCE

6.1 Introduction

Simple experiments and simulation suggest that it will be possible to use Lamb waves to interrogate thin films. The possibility of a full tomographic reconstruction of thin films in the presence of defects/additions was explored by analyzing the radiation patterns of the firing transducer patterns

6.2 Defining Transducer Radiation Pattern

First, the beam or radiation pattern of the source and/or generating geometry was explored. Lamb waves were generated using 1MHz transducers in 76 µm thin aluminum films and the receiving transducer was laterally shifted on the opposite side of the film up to 4cm. The receiving transducer was able to pick up good signals to at least an 8cm (4cm on each side). What is more, as seen in Figure 35, the signal strengths remained

Source
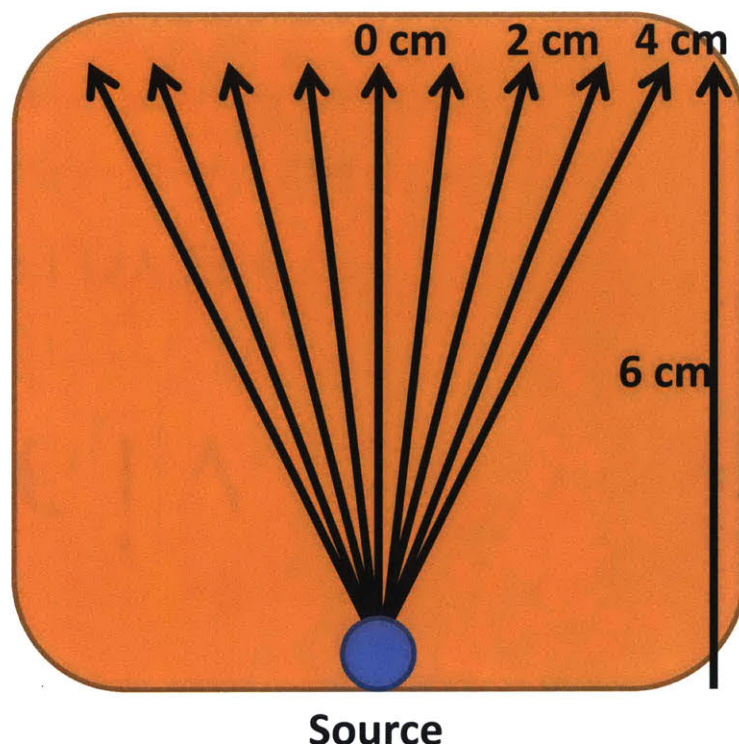
Figure 35: Area of Influence of Lamb Waves in Thin Films

65

relatively strong making this kind of wave ideal for large area interrogation. This was confirmed by integrating the squared magnitude of each of the signal lines and creating a span of the energy profile as seen in Figure 36.
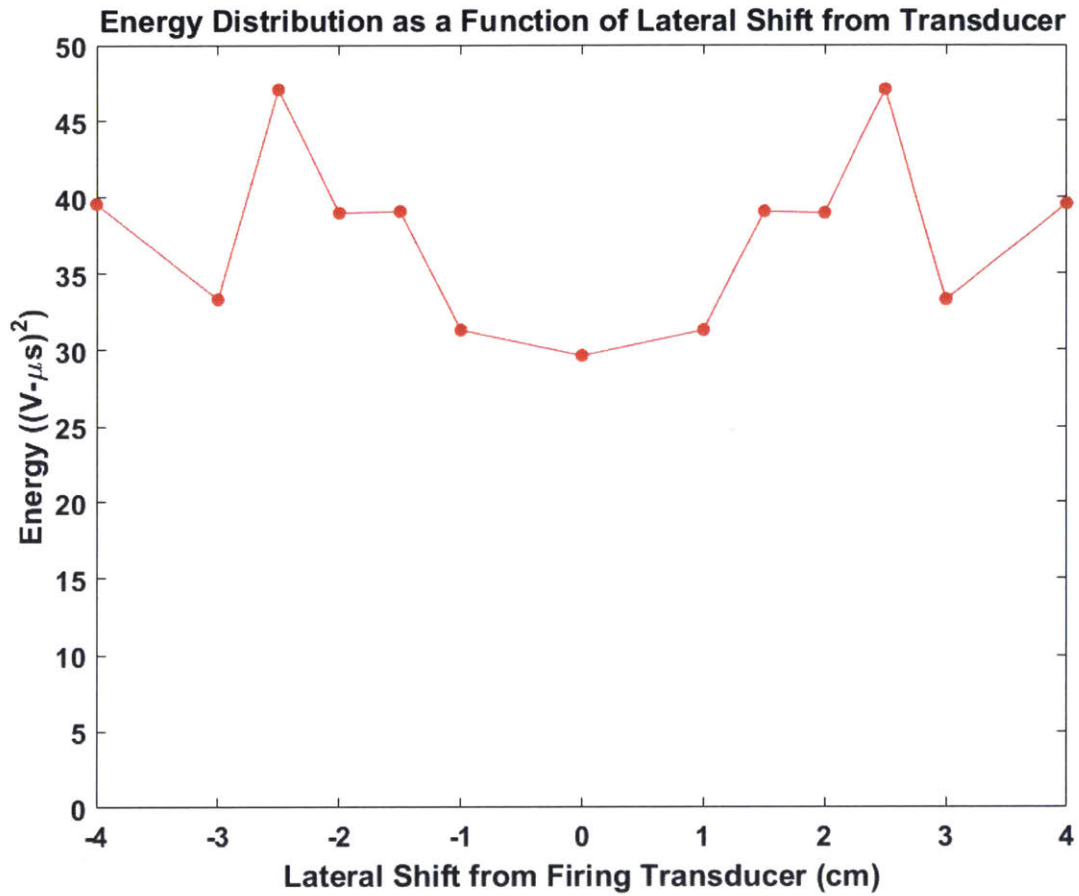
Figure 36: Energy Distribution Around Firing Transducer
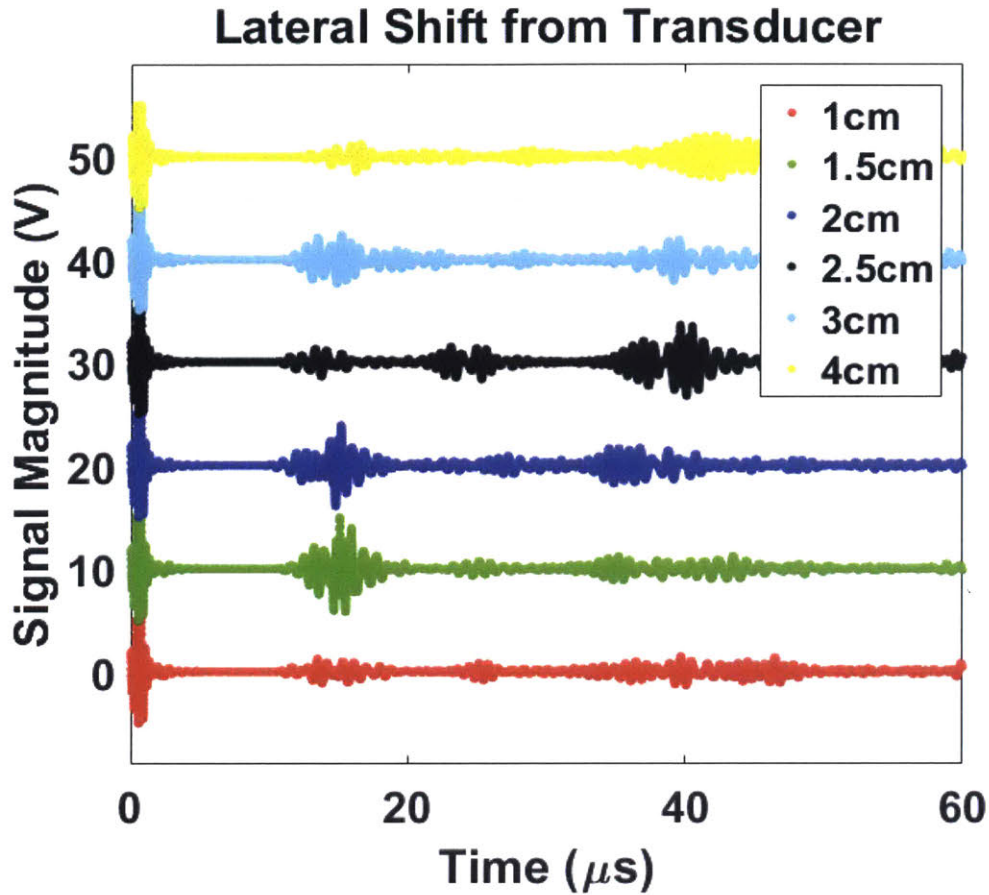
Figure 37: Lamb Wave Signal Characteristics as a Function of Lateral Shifts in Receiving Transducer

In addition to lateral shifts, the effect of receiving distance was also analyzed and, as seen in Figure 37, the signal strength stays relatively high or attenuates slowly further indicating that this method of probing thin films over large areas is promising. This was confirmed by integrating the squared magnitude of each of the signal lines. This fact combined with the ability of Lamb waves to identify surface additions/deletions, makes for a promising technique for NDE of R2R substrates. In essence, this simple experiments promises the ability to interrogate an area of at least 6cm x 8cm (48cm^2).
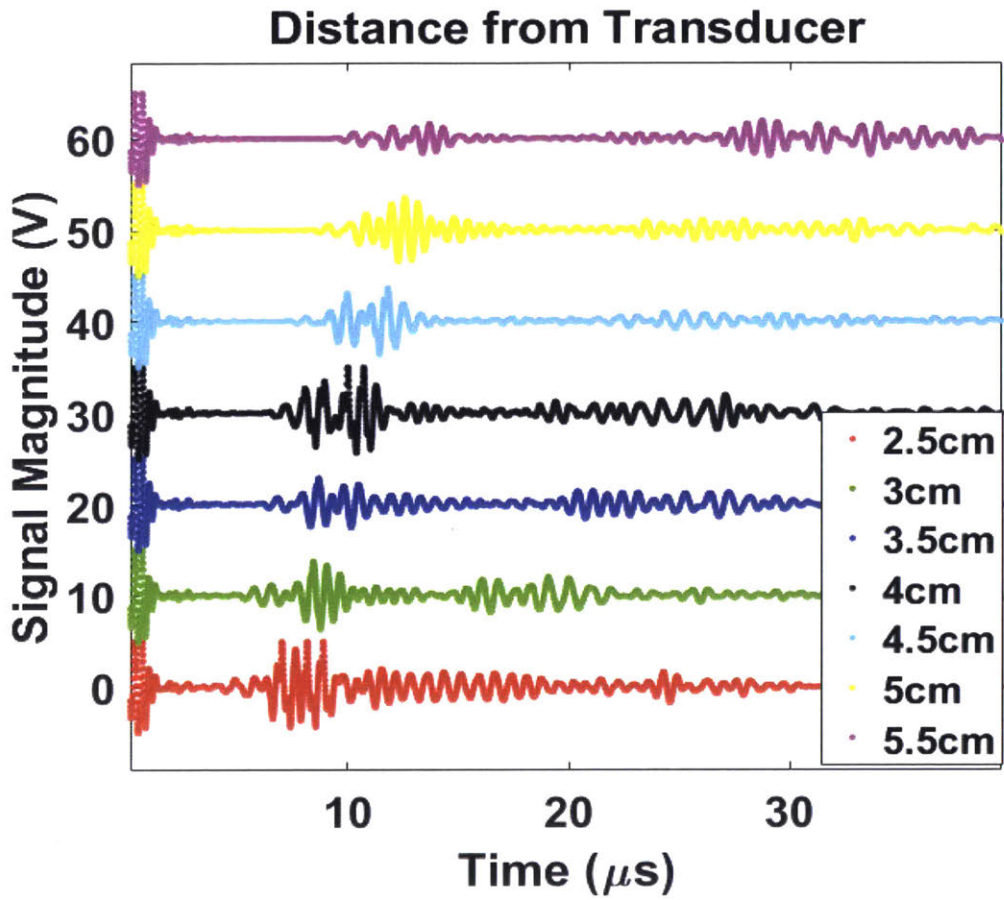
Figure 38: Lamb Wave Signal Characteristics as a Function of Increasing Distance from Receiving Transducer

Energy Distribution as a Function of Perpendicular Shift from Transducer
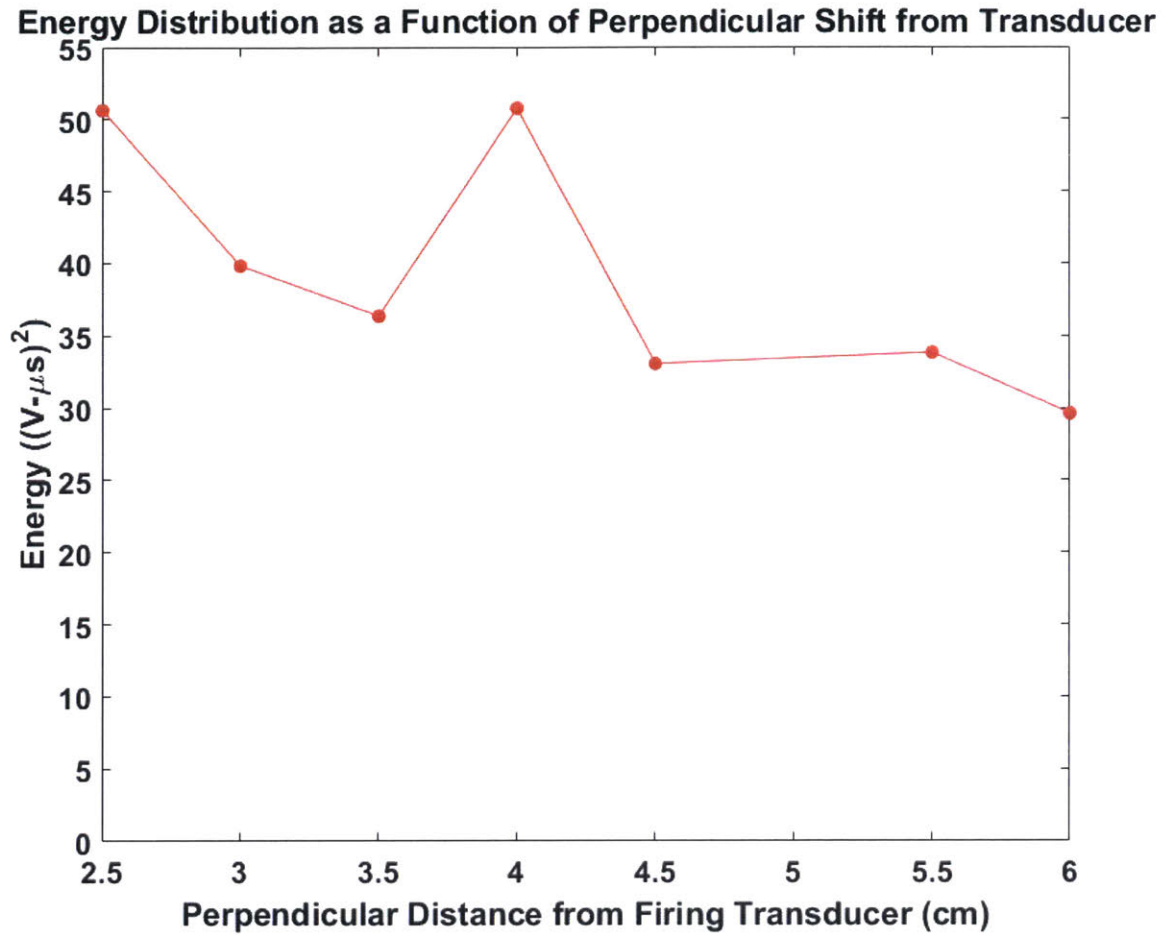
Figure 39: Energy Distribution Away from the Firing Transducer

6.3 Conclusion

The results from this section indicate that at the very least, an area of 48 cm^2 can be interrogated with the intent of creating tomographs. This large of a surface area is sufficient to demonstrate the viability of Lamb waves to interrogate the surface and bulk characteristics of R2R substrates.

7

FULL CONTACT LAMB WAVE TOMOGRAPHY

7.1 Introduction

Having established the possibility of using Lamb waves to analyze the surface and bulk properties of thin aluminum films, this section describes early attempts at creating tomographs using a full-contact ultrasound imaging approach.

7.2 Full Contact Lamb Wave Imaging

The first attempt at a full tomographic reconstruction involved the use of a full-contact setup. Here a full tomographic reconstruction refers to the interrogation of the bulk/surface characteristics of the film with the intent of creating a map of features. Two 1 MHz Olympus transducers were laterally scanned along the edges of the film as seen in Figure. The firing and receiving transducers were moved in 1cm increments and the area was raster scanned. The area under inspection was a 12cm x 12cm 76μm aluminum film. The firing-receiving transducers were moved not only in a left-right configuration, but also a top-bottom configuration. In essence, both dimensions of the film were analyzed. A sample workflow for this is as follows:

1) Place firing transducer at 1cm increment along left edge.
2) Collect data with receiving transducer at all 12 locations along right edge.
3) Move firing transducer to 2cm increment.
4) Repeat step 2.

The same four steps above were also repeated in the top-bottom configuration with the firing transducer being place along the top edge and the receiving transducer being place along the bottom edge. The data collection setup and apparatus were the same as mentioned before and the transducers were manually moved. Image of the film under consideration can be seen in Figure 40.
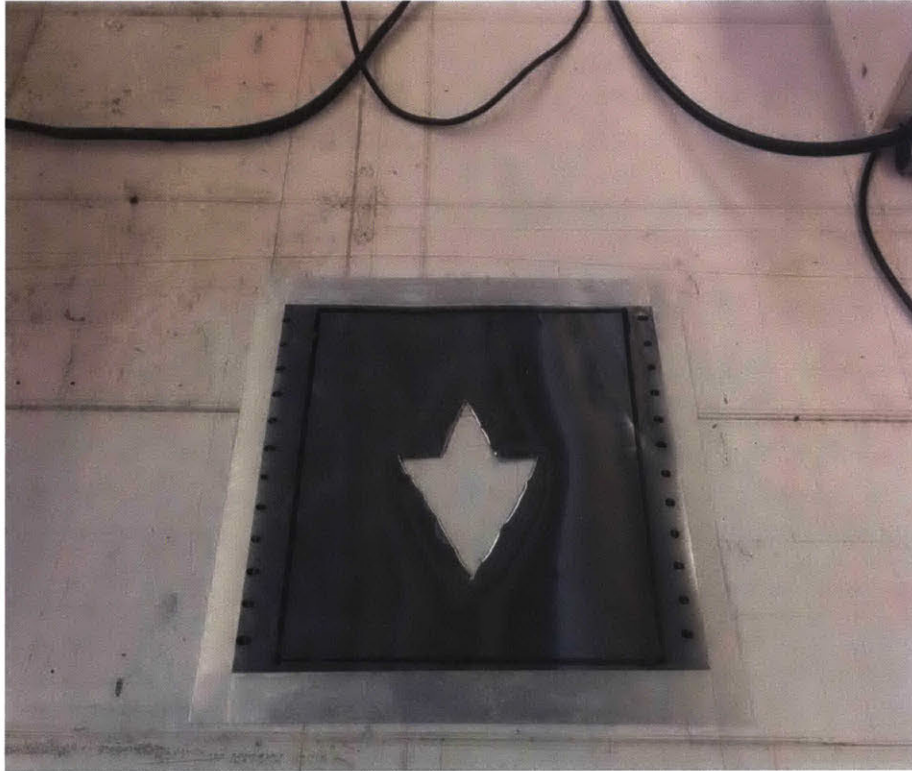
Figure 40: Aluminum Film used for Ray Path Intersection Algorithm

Once the data was collected, a simple reconstruction algorithm, which we call the Ray-Path Intersection Algorithm, was implemented:

1) The energy associated with every transmit-receive signal i was computed using a standard integral in time, $\psi(i)$. There were a total of M signals corresponding to every transmit-receive pair.

2) The area of the film was discretized in 1cm increments for a total of 144 grid points (j).

3) Straight lines and their corresponding equations were computed between every transmit-receive pair. Note: This algorithm assumed a linear wave path.

4) Grid points falling on the path of each ray were computed together with the length of intersection.

5) For all grid points falling in the path of a given ray, the lengths of intersections were summed.

6) Each grid point along a given ray path, was then assigned a length fraction w_{ij} that represented the fraction of the total length of intersection along the ray path within a specific grid point.

7) All grid points failing in the path of a given ray were then assigned the integral from step 1 scaled by the factor w_{ij} (also known as $\phi(j)$). This was done for all 144 rays.

A mathematical representation of this can be seen below:

$$\phi(j) = \sum_i^M w_{ij} \psi(i) \tag{7.1}$$

$$\psi(i) = \int |F_i(t)|^2 dt \tag{7.2}$$

Here $F_i(t)$ is the signal received between a single transmit-receive pair.

Using the above algorithm, analysis was conducted on the film above. Results of the reconstruction can be seen in Figures 41-44.

Signal Profile of Aluminum Film (76 μm)
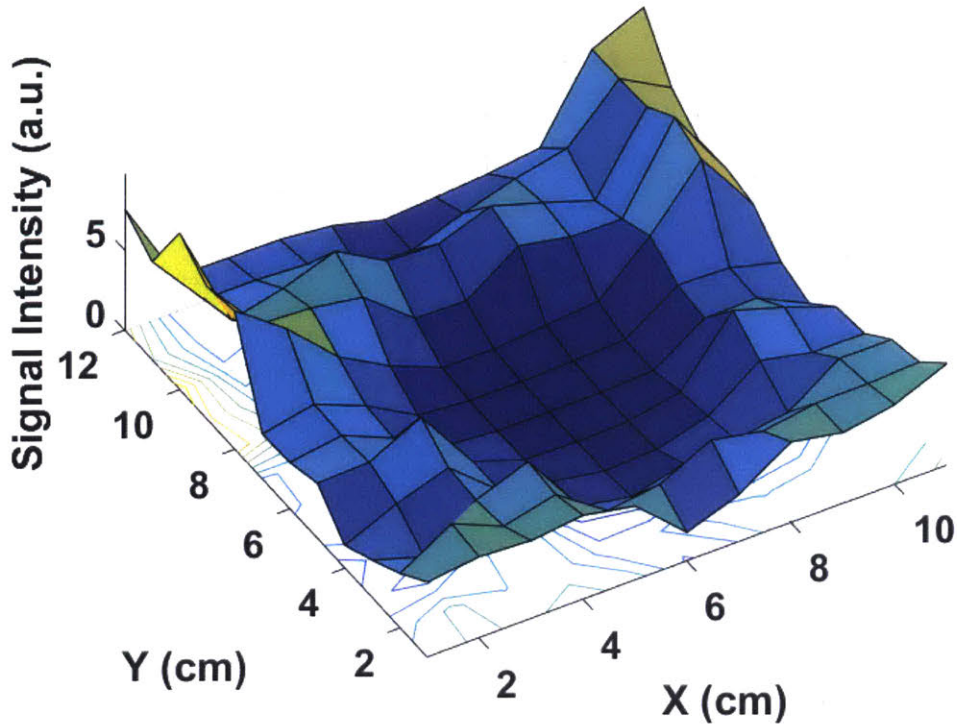
Figure 41: 3-D Signal Profile o f Aluminum Film Reconstructed using Ray-Path Intersection Algorithm

The 3-D nature of this graphic comes from the fact that as we get to grids closer and closer to the defect, the rays intersecting these grid points have smaller energies, $\Psi(i)$, and hence get smaller $\phi(j)$ added. This results in a convex numerical geometry with the defect kying in the center and the unperturbed film surrounding it.

Figures 41 and 42 show different interpretations of the same idea. Figures 41 and 42 depict a 3-D and 2-D contour maps respectively whereby lines of equal intensity indicate those grid points on the numerical grid that have the same exposure to the ultrasound radiation. Viewing the map this way makes it easier to discern areas on the film with similar interactions with the incident Lamb waves.
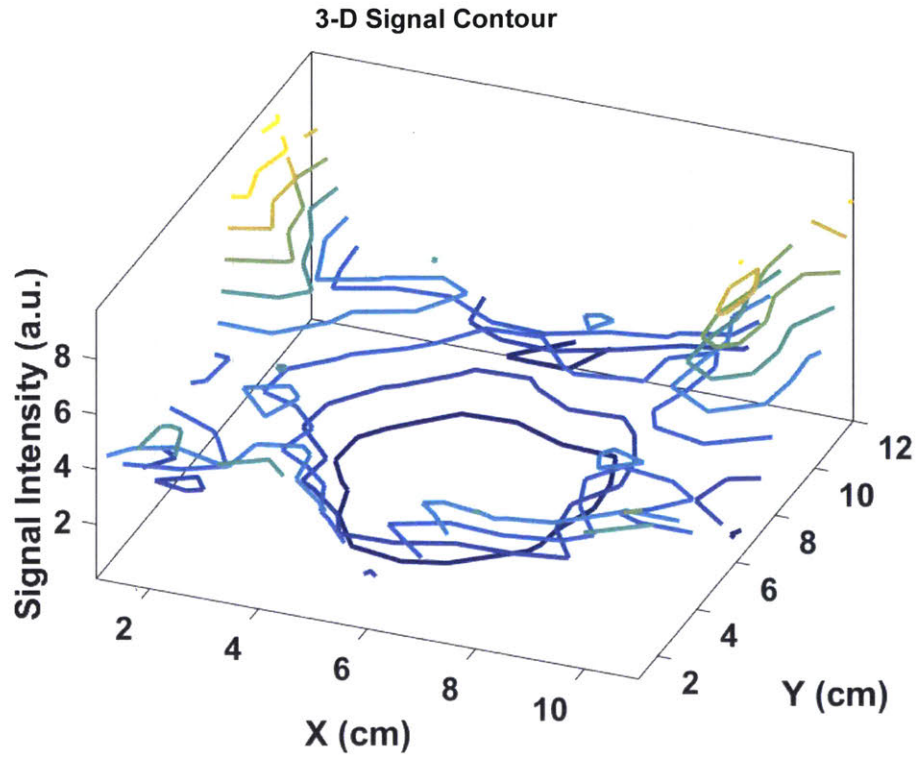
3-D Signal Contour

Figure 42: 3-D Signal Contour o f Aluminum Film Reconstructed using Ray-Path
Intersection Algorithm

2-D Signal Contour

74
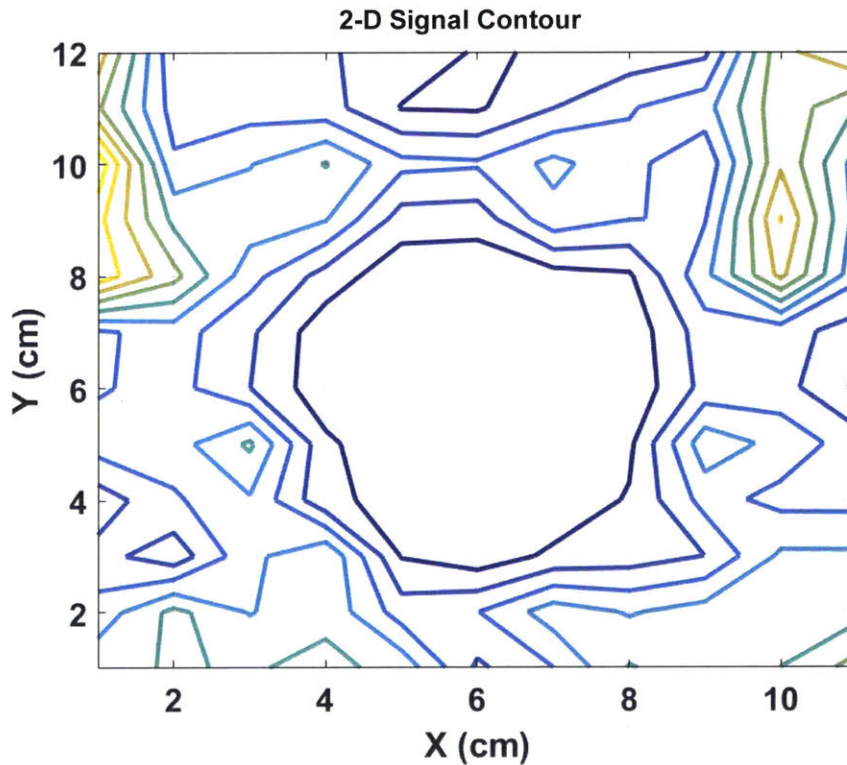
Figure 43: 2-D Signal Contour o f Aluminum Film Reconstructed
using Ray-Path Intersection Algorithm
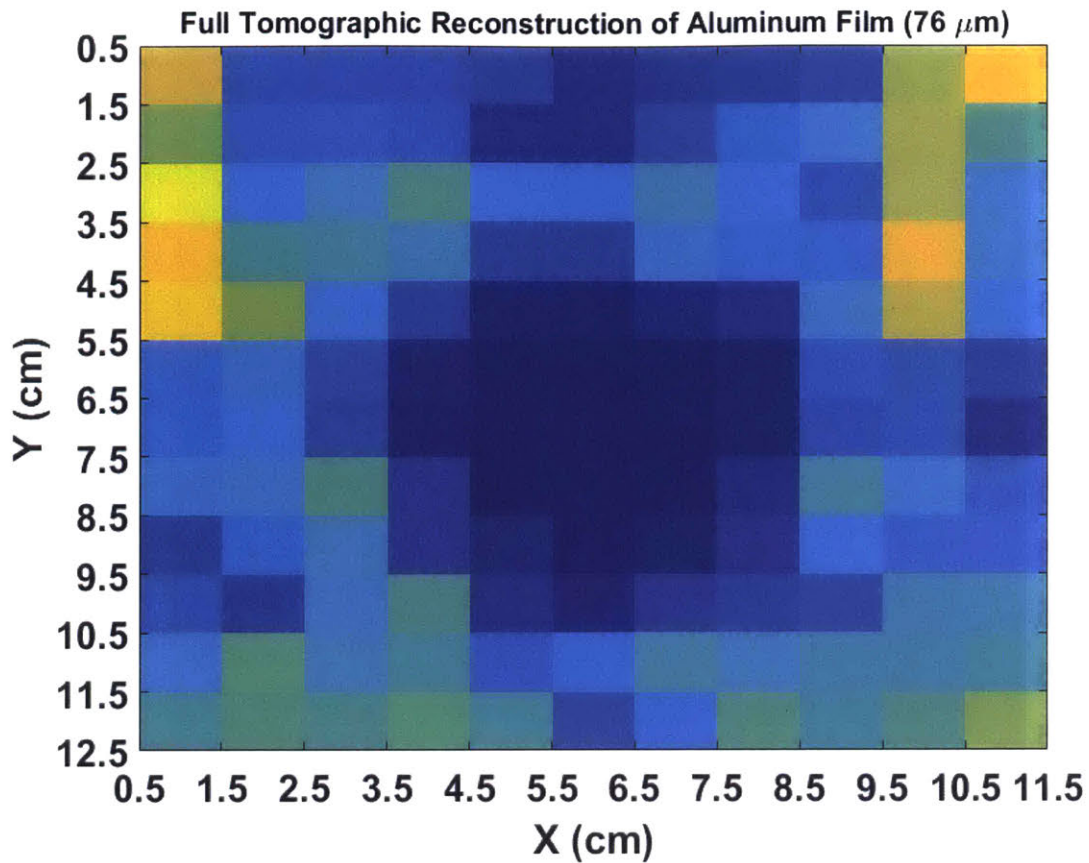
Figure 44: Tomographi Reconstruction o f Aluminum Film Reconstructed using Ray-Path Intersection Algorithm

Based on visual inspection and comparison with the true geometry, it seems that this simplistic method of reconstruction works well for relatively large defects. In an extension of this work, the ability of this method to detect surface features was explored. A relatively large drop of arbitrary size (~1.5cm in diameter) of ultrasound gel was dropped onto the film in the center and the procedure was repeated. The result of the tomographic reconstruction can be seen in Figure 45. Here, the true values of the grids mean very little. It is more important to know that the darker the color, the smaller the presence of ultrasound radiation in those grid points.
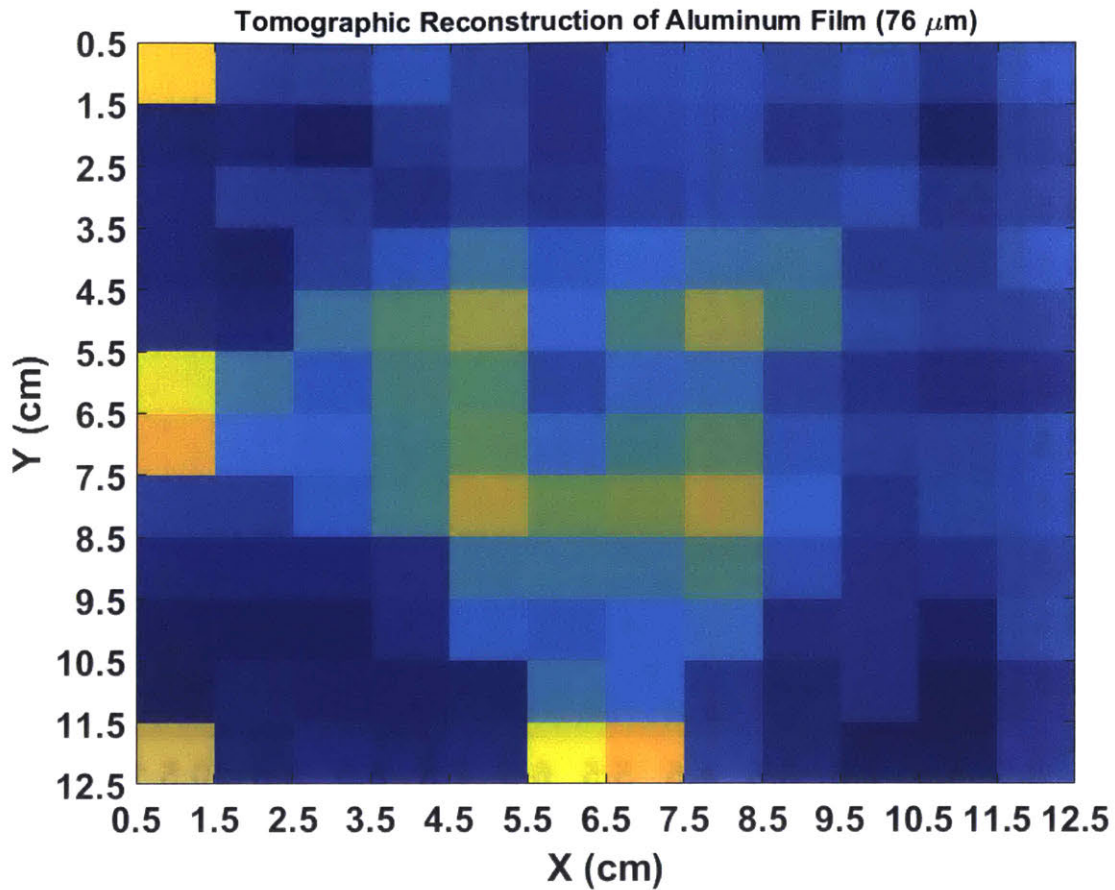
Figure 45: Tomographic Reconstruction of Film with Surface Addition (US Gel) using Ray-Path Intersection Algorithm

7.3 Conclusion

From this result it becomes obvious that there are a number of drawbacks associated with this simplistic algorithm and setup:

1) Inability to provide high resolution as evident from the size of defects this method can probe.

2) Inability to identify the presence of surface features such as the ultrasound gel.

3) Size of the transducer head (10mm) restricts fine incrementation during data collection.

4) The fully contacted nature of data acquisition makes this unappealing for sensitive processes such as R2R manufacturing.

8

QUASI CONTACT LAMB WAVE TOMOGRAPHY

8.1 Introduction

After the results of the previous experiments, the biggest limitations were the insufficient resolution and the contact-nature of the transduction. In an attempt to overcome these limitations, a quasi-contact approach was used. This chapter is devoted to the description of the experimentation and results of this approach. A quasi contact, as opposed to a full non-contact approach, was implemented because of the intricacies associated with setting up a vibrometer. Specifically, aligning steering mirrors and ensuring excellent reflection off the aluminum required extensive setup which were forgone for now, but were reproached later.

8.2 Introduction
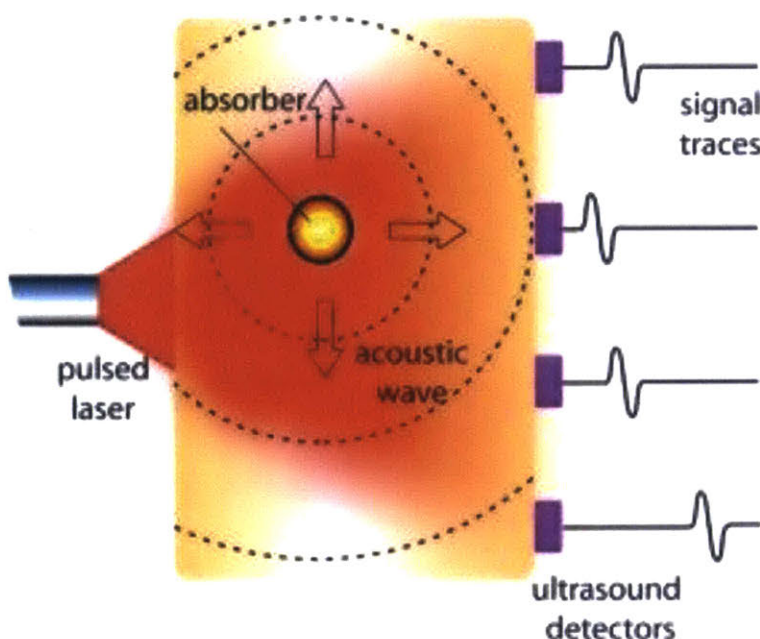
In this method, a 1064nm pulsed laser operating at ~1mW with a pulse frequency of 10Hz, a pulse duration of 9ns, and a spot size diameter of ~2mm was used to generate the Lamb waves. This method of generating ultrasonic waves is a branch of ultrasonics known as laser ultrasound or sometimes photoacoustics. A schematic of the

Figure 46: Photoacoustic Imaging and Signal Processing [33]

process on the surface can be seen in Figure 46. When a pulsating laser hits the absorbing surface, the area on the surface expands and contracts rapidly thereby producing pressure waves. Furthermore, given that the absorbing material here is a metal, the orthogonal nature of the laser source results in the formation of transverse waves, specifically Lamb waves. Finally, given the smaller spot size (2mm as opposed to 10mm), this method has the potential to raster scan the surface in finer increments thereby providing greater resolution.
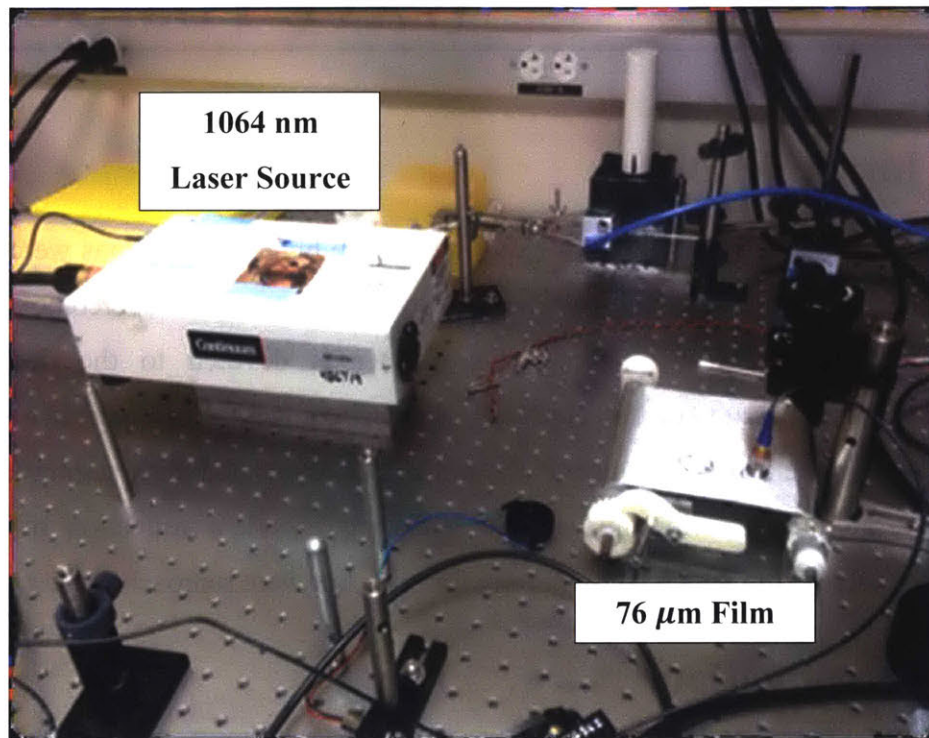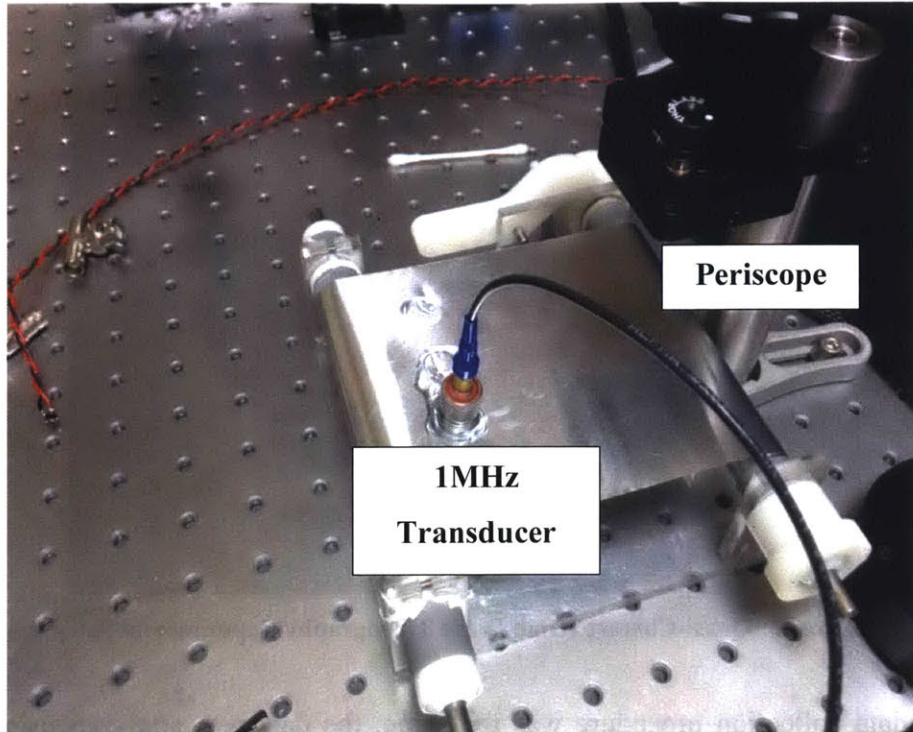
Figure 47: Quasi-Contact Lamb Wave Tomography Experimental Setup

A setup of our experiment can be seen in Figure 47. A periscope setup from Thorlabs (RS99T) along with a Nd:YAG mirror (NB1-K14) was used to deflect the incoming laser beam at 90°. The produced waves were captured using a 1MHz contact transducer as before. An NI DAQ along with a custom LabVIEW program (see Appendix) was used to collect the data. The data was collected with a sampling frequency of 125 MHz and the data collection scheme was the same as the one outlined earlier. The area under investigation was a 76 μm thick Aluminum film with a drop of cutting oil placed on it. The oil drop was of arbitrary size (~1in diameter). A schematic of this can be seen in Figure 48.
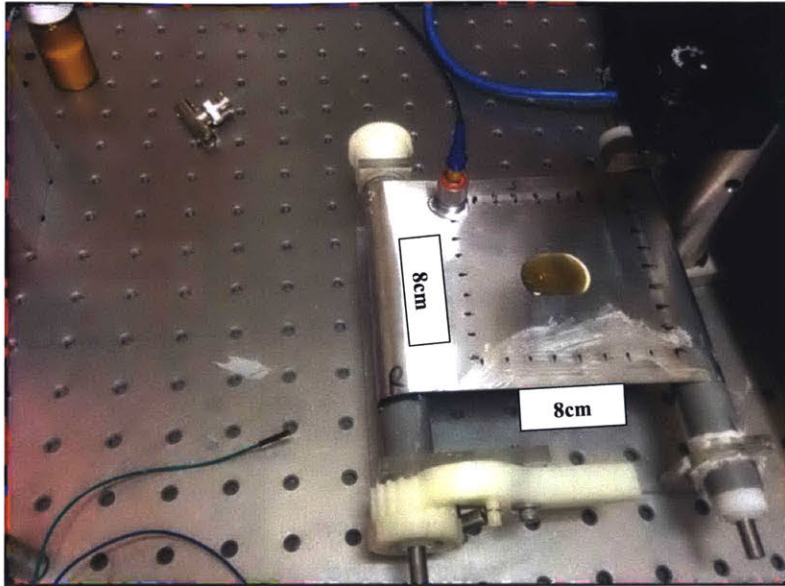
Figure 48: Quasi-Contact Lamb Wave Tomography Experimental Setup

While the data collection procedure was the same, the data was analyzed using a different algorithm. The Ray-Path Intersection algorithm was simplistic and was unable to pick up variations in signals associated with surface features. In this experiment, an algorithm known as Reconstruction Algorithm for Probabilistic Inspection of Defects (RAPID) [34] was used. The data acquisition procedure works as follows:

1) Place laser at 1cm increment along left edge.
2) Collect data with receiving transducer at all 9 locations along right edge with no oil drop present.
3) Move firing transducer to 2cm increment.
4) Repeat step 2.
5) Repeat procedure on the defect free surface in the other direction (Top-Bottom)

Following data collection on the intact film, the oil drop was placed and the data collection procedure above was re-done. A visualization of the grid points and the transmit-receive locations can be seen in Figure 49.
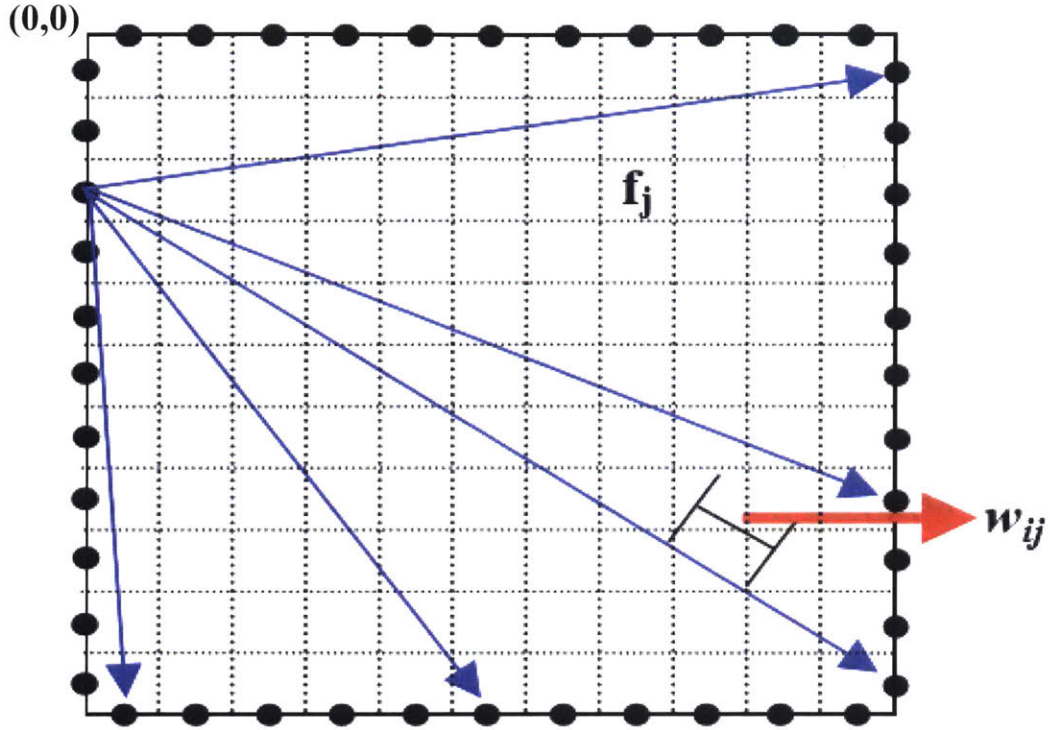
Figure 49: Transmit-Receive Locations and Grid Points for Quasi-Contact RAPID Algorithm

The reconstruction algorithm used once the data was collected is as follows:

1) The domain analyzed was discretized as a finite mesh with center points (x, y).

2) For every grid point, the following was computed. Intuitively, R is the relative distance of the grid point in question from the transmit-receive paid and s is a measure of which transmit-receive pair will irradiate a given grid point.

$$R_{i,j}(x, y) = \frac{\sqrt{(x_i-x)^2+(y_i-y)^2} + \sqrt{(x_j-x)^2+(y_j-y)^2}}{\sqrt{(x_j-x_i)^2+(y_j-y_i)^2}}$$

(8.1)

$$s_{i,j}(x,y) = \frac{\beta - R_{i,j}(x,y)}{1-\beta} \; if \; \beta > R_{i,j}(x,y) \tag{8.2}$$

Here x_i, x_j, y_i, y_j are the x and y positions of the firing and receiving transducers respectively.

3) In addition to step 2, a signal difference coefficient was computed for every transmit-receive pair. Intuitively, the SDC is a measure of the difference between the reference and perturbed signals.

$$SDC_{i,j} = \frac{(\sum_{t=0}^{T}(Ref(t)-\overline{Ref(t)}) \times (True(t)-\overline{True(t)}))}{(N_t \times stdev(Ref(t)) \times stdev(True(t))} \tag{8.3}$$

Here $Ref(t)$ and $True(t)$ are the reference (defect-free) and true (defect-ladden) signals respectively.

4) Finally, the probability of having a 'defect' at a given grid point was estimated as follows. This value can be thought of as a weighted sum of the SDC's of all transmit-receive signals scaled by the area of irradiations.

$$P(x,y) = \sum_{i=1}^{N} \sum_{j=1,j\neq i}^{N} SDC_{i,j} s_{i,j} \tag{8.4}$$

The only explained parameter here is β. This is a geometric free parameter that defines the area of influence of the transducer. A visualization of this can be seen in Figure 50.

82
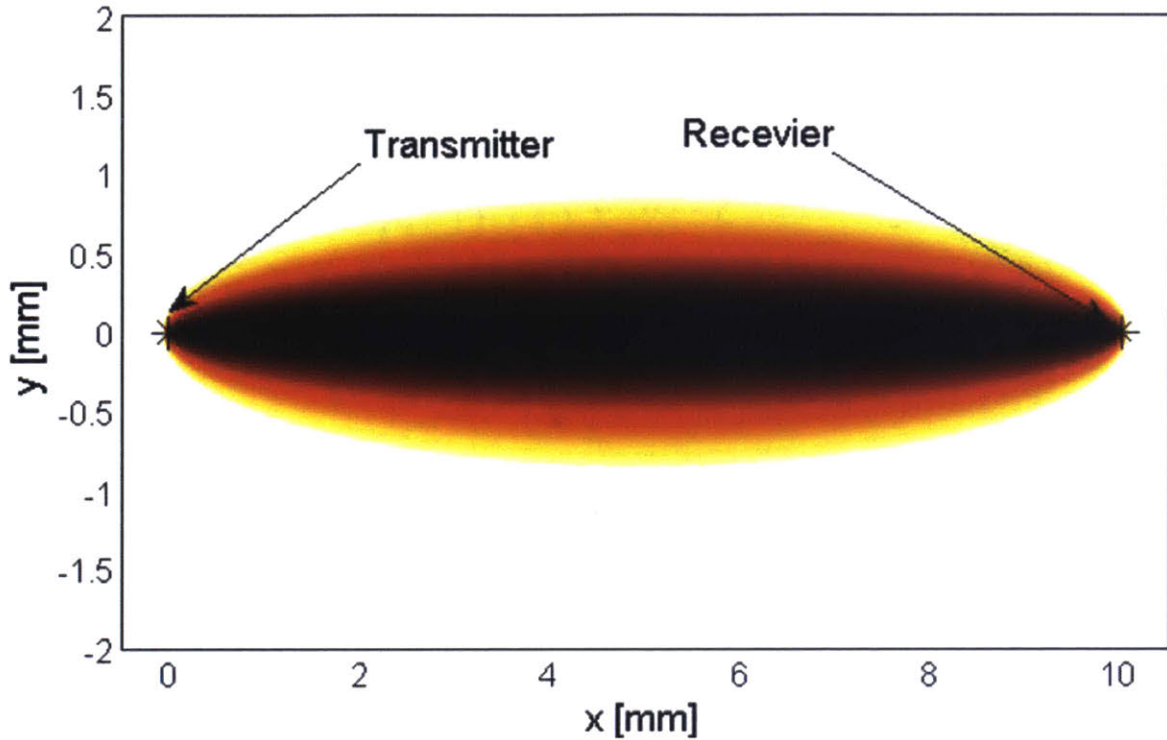
Figure 50: RAPID's Beta Parameter Visualization [32]

The algorithm was implemented for two values of β, 1.01 and 1.50. As can seen from Figure 49, as β increases, the area of influence of the transducer increases. Based on literature [32], a β value of 1.05 was chosen to perform the reconstruction.

Based on the results seen in Figure 51, this algorithm combined with the chosen value of β seems to work well as the reconstructed image matched the true strcuture quite well. This is evident because the algroithm successfully localizes the oil drop and estimates it's geometry with relatively good accuracy. One key point needs to be further refined in order to definitively determine the algorithm. Parameter optimization needs to be conducted in order to ascertain the best value for β. In Figure 52, the second image is a cleaned version of the first because the algorithm only retained those grid points where the porbability of a defect was significant (>0.85).

RAPID Tomographic Reconstruction of Aluminum Film (76 μm, β = 1.5)
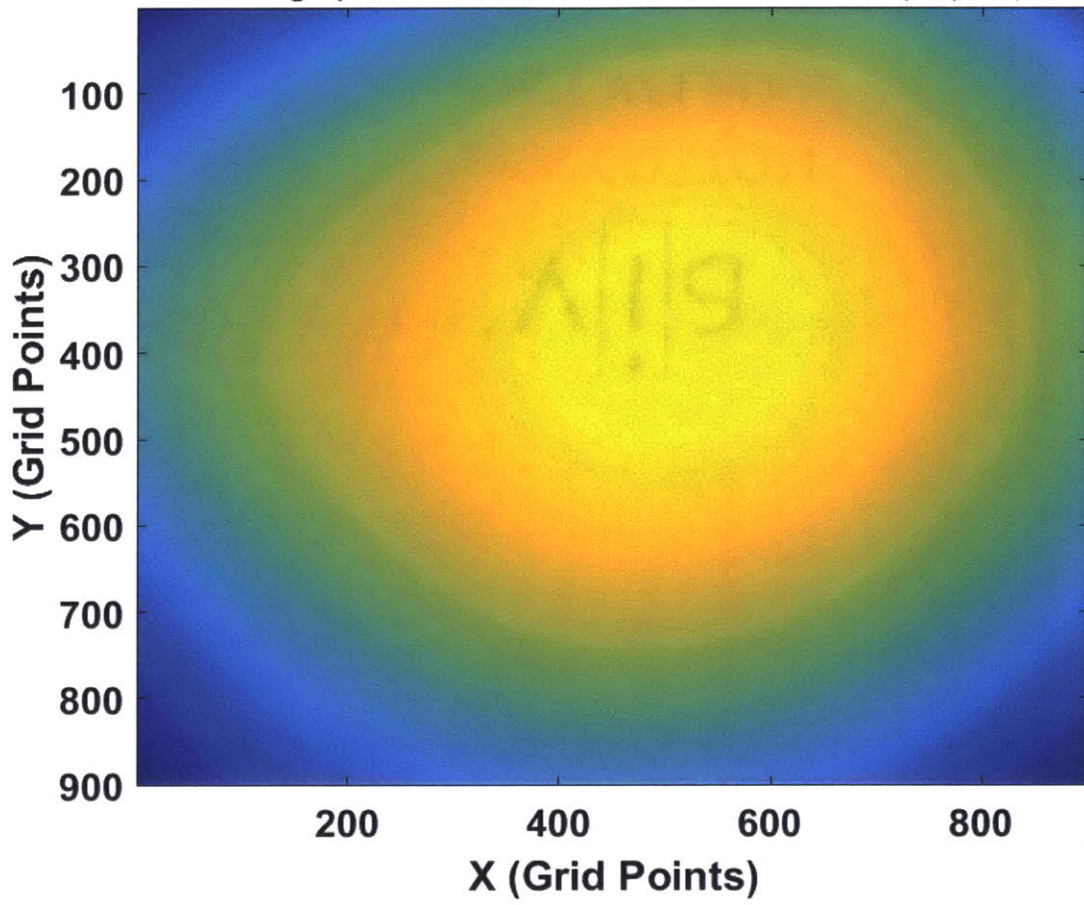
RAPID Reconstruction of Aluminum Film (76 μm, β = 1.01)
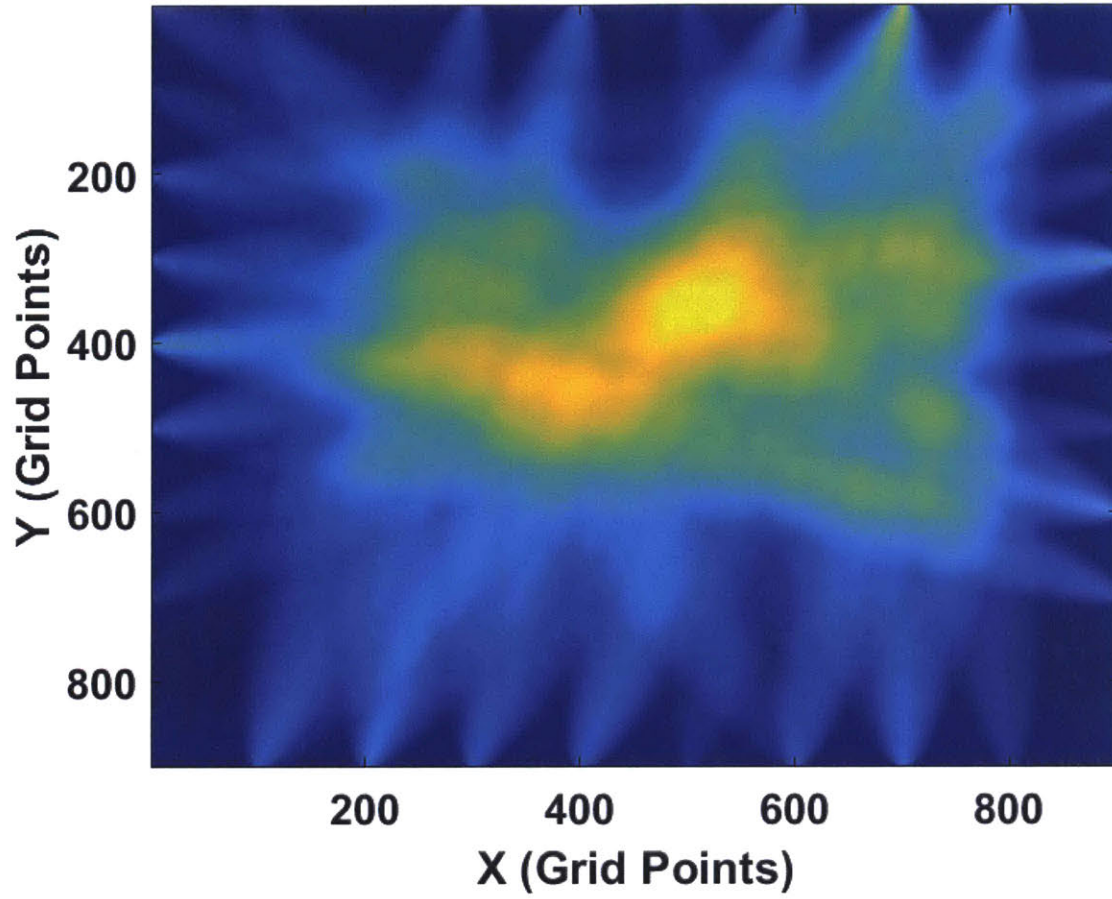
Figure 51: Effect of Increasing Beta on RAPID Reconstruction Results (a) β = 1.5 and (b) β=1.01

RAPID Tomographic Reconstruction of Aluminum (76 μm, β = 1.05)
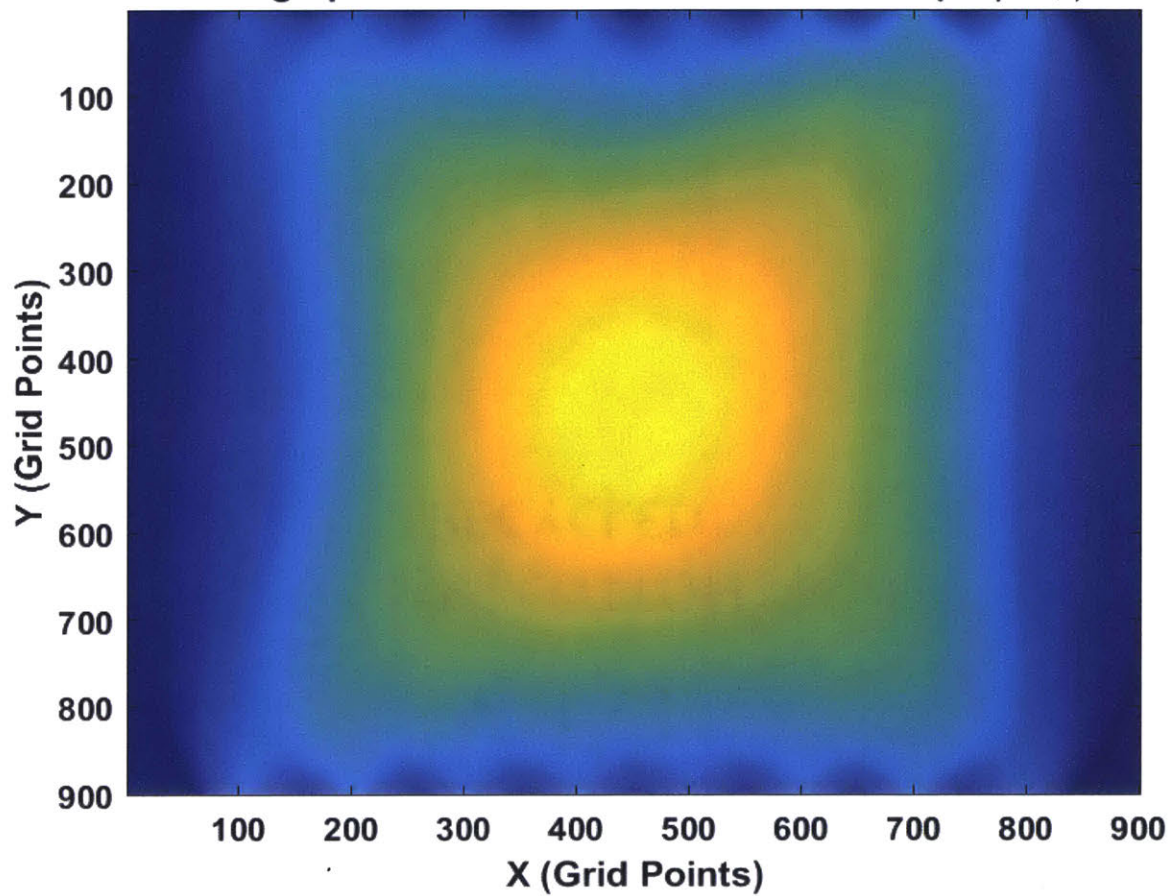
Refined RAPID Tomographic Reconstruction of Aluminum Film (76 μm, β = 1.05)
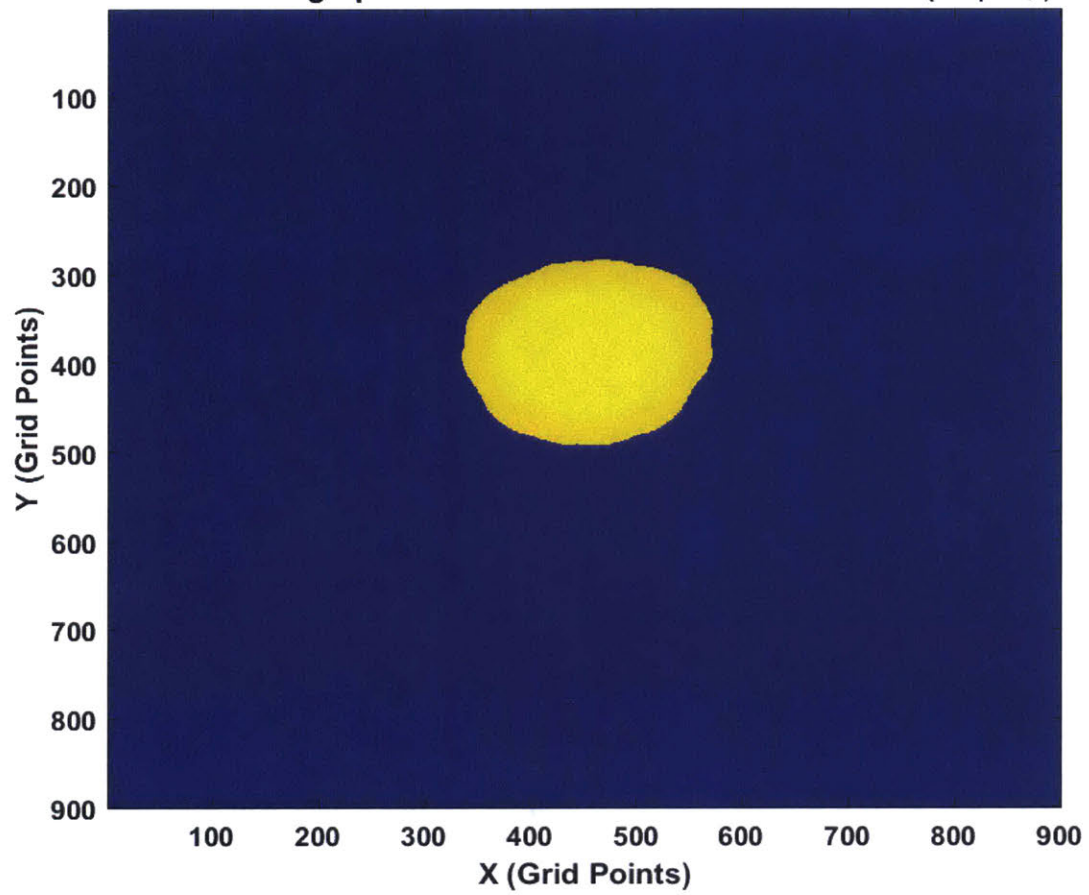
Figure 52: (a) RAPID Tomographic Reconstruction Results of Oil Drop on Aluminum Thin Film (b) Processed Image from RAPID Results to Identify High Probability Grid Points

Finally, a comparison between the true geometry overlayed with the computed geometry can be seen in Figure 53 below. The mismatch along the contours is due to the delay in capturing data. In waiting to capture data, the oil spread along the surface.
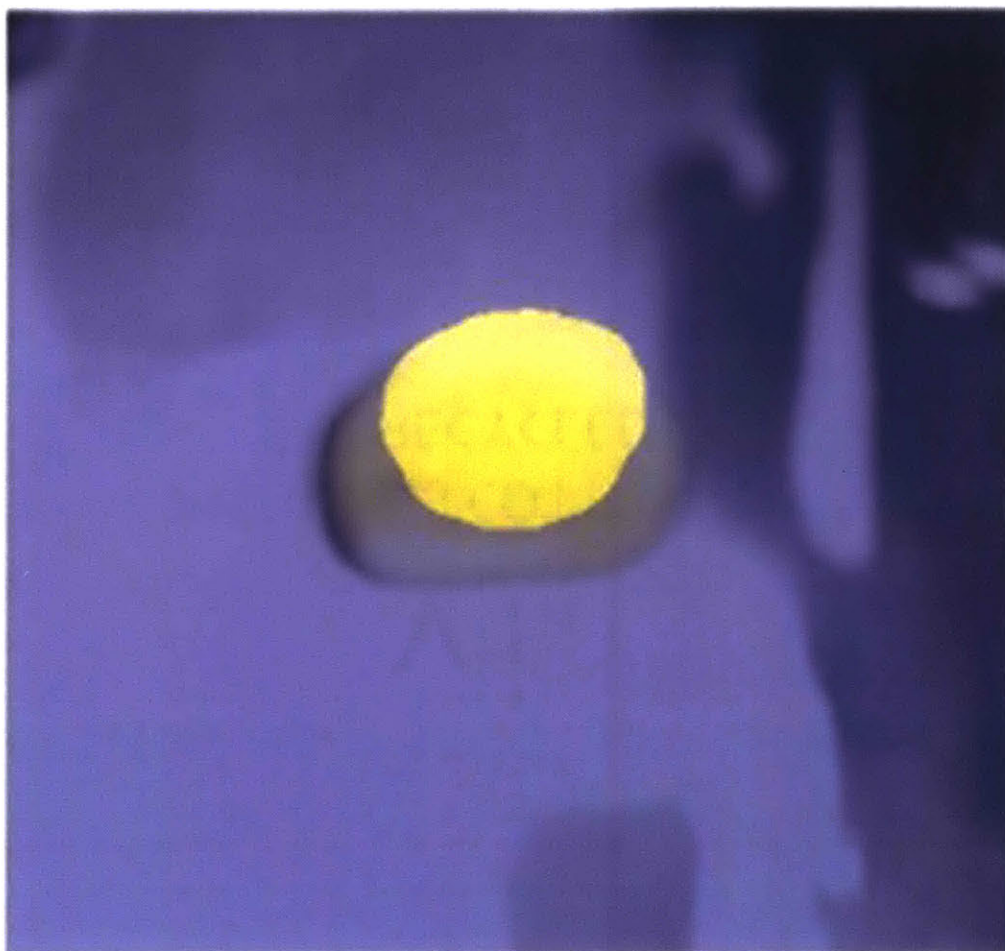
Figure 53: Visualization of Difference between Quasi Contact RAPID Imaging and the True Geometry

8.3 Conclusion

Based on the results presented in this section, it can be interpreted that the quasi-contact method combined with the RAPID algorithm maybe able to accurately reconstruct surface features. Given this, it is natural to ask the following questions (all of which will be addressed subsequently)

➢ **Orientation**: Can this method be converted to an entirely non-contact method?

➢ **Sensitivity**: Can this method be used to distinguish between surface features in terms of physiochemical properties such as density?

➢ **Resolution**: What is the smallest feature size this method of imaging can reconstruct?

The following sections will seek to address a number of these questions.

9

INCREASED SENSITIVITY
LAMB WAVE TOMOGRAPHY

9.1 Introduction

Prior to addressing the concerns associated with improving the quasi-contact lamb wave tomography, another important avenue was pursued. There are two major objectives associated with tomographic imaging of substrates using Lamb waves: (a) Identify bulk and surface features within/on the substrate and (b) Differentiate between different chemicals/materials placed on the surface of the substrate. The first objective has been accomplished with some level of accuracy, but the second one has not yet been addressed. While it has been shown that, for instance, drops of water/salt solutions in water placed on the surface of aluminum or other thin substrates produce a characteristic Lamb wave signal [35], it has not yet been show that these drops of water would manifest differently than drops of oil. The mechanical properties of chemicals such as viscosity may vary subtly. Furthermore, the feature size of these patterns on the substrates can range from nm to a few hundred microns. While this work has not advanced enough to image at that scale, imaging on the order of ~1mm should be possible. The resolutions of the S_0 and A_0 Lamb waves in 76μm aluminum at 1MHz are on the order of $\frac{5500(\frac{m}{s})}{10^6 Hz} = 5.5mm$ and $\frac{2000(\frac{m}{s})}{10^6 Hz} = 2mm$ respectively and as such increasing the frequency should increase the resolution to ~1mm.

9.2 Increased Sensitivity of Lamb Waves

In order to image on the order of ~1mm and to be able distinguish between chemicals with differing bulk fluid properties, higher frequency transducers were used to listen for the Lamb waves.

Black electrical tape 1mm in width was taped onto the 76 μm aluminum sheet which was excited with the 1MHz transducer source. 2.25 and 5 MHz receiving transducers were used to capture the transmitted signal in order to determine which configuration provided maximum
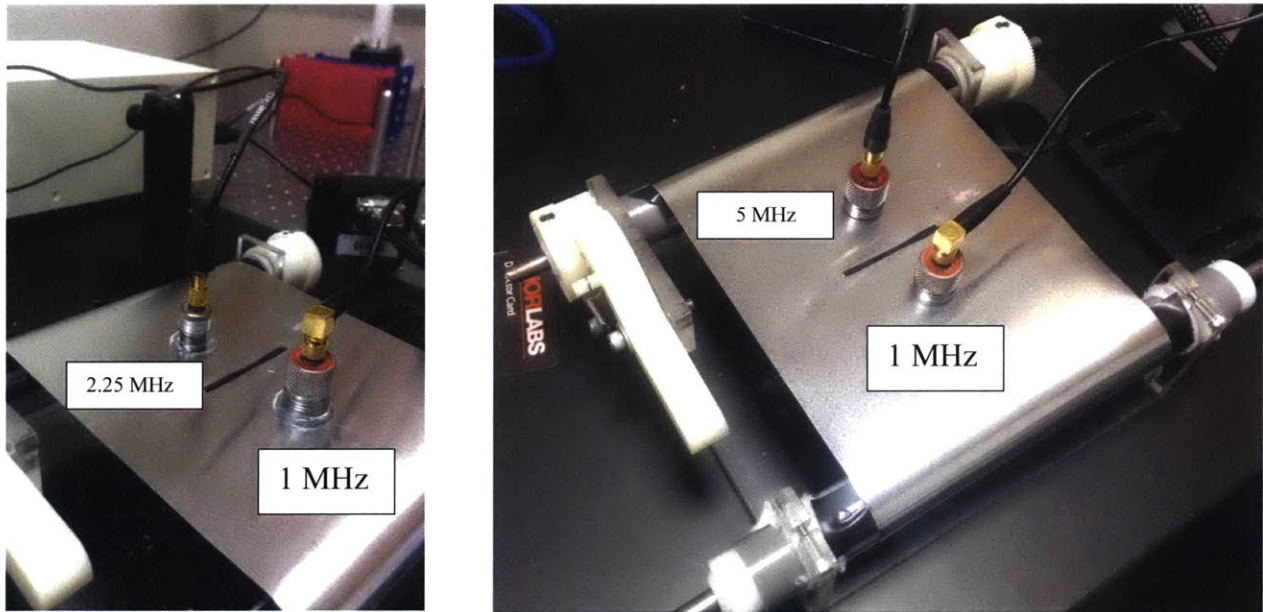
Figure 54: (a) 1.00 MHz Firing Transducer with a 2.25 MHz Receiving Transducer (b) 1.00 MHz Firing Transducer with a 5.00 MHz Receiving Transducer

sensitivity to a 1mm surface feature. Similarly, the higher frequency transducer configurations were also used to determine which transducer could distinguish between water (1000 kg/m^3) and oil drops (Castor Oil, 961 kg/m^3). Schematics of the test setup can be seen in Figure 54 (a) (2.25MHz) and 51(b) (5.0MHz).

The experimental procedure involved collecting a reference signal with no surface additions and then the tape/fluid was added and signals were re-collected. Finally, according to the SDC equation (8.3), a metric of differentiability was computed. As can be seen in Figure 55, the 1-2.25 MHz configuration provided the most sensitivity to perturbations on the order of ~1mm and variation in physiochemical properties of the artifacts.
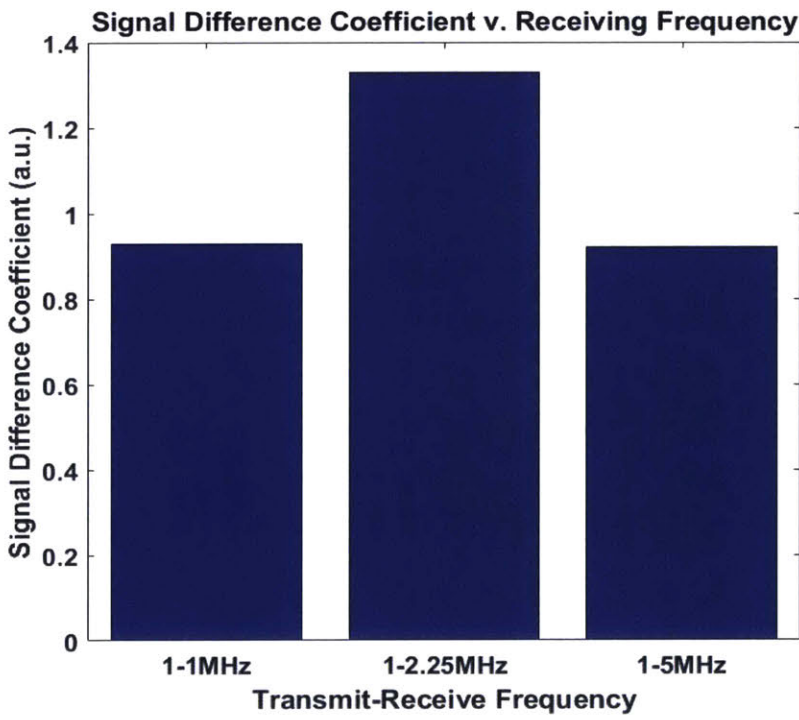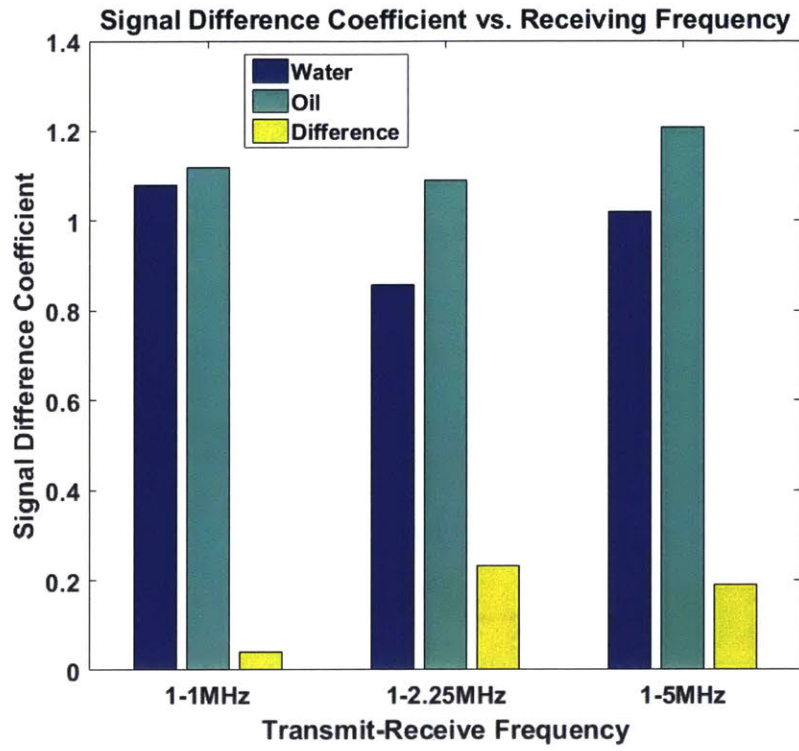
Figure 55: (a) Effect of Varying Fluid Additions on Lamb Wave Characteristics (b) Effect of Varying Reception Frequency on Lamb Wave Characteristics (1mm Tape as a Surface Addition)

From Figure 55a, it can be seen that the 1-2.25 MHz transmit-receive pair results in signals that are the most sensitive to the presence of differing fluids. The SDC value for the oil signal differs the most from that of the water when using the 2.25MHz transducer to listen. Similarly in Figure 55b, the SDC coefficient when using the 2.25MHz transducer provides the most sensitivity to the presence of the 1mm black tape.

Given the results of this experiment, the 2.25MHz transducer was used to reconstruct a finer tomographic map of the geometry depicted in Figure 56. Here black tape with a width of 1mm as used to outline an M on the aluminum. An M was chosen for several reasons:

1) It consists of multiple planes of symmetric thereby making the imaging from different edges meaningful.

2) The middle tip of the M consists of overlapping pieces of tape. This results in an increased thickness compared to the rest of the letter and as such the imaging process should be able to identify that.

A similar procedure as outlined in the full contact tomography before was followed with four notable exceptions:

- A 2.25 MHz transducer was used to listen for the Lamb waves.

- Given the smaller diameter of the 2.25 MHz transducer, the scanning was done in 0.5cm increments as opposed to 1cm increments.

- No defect free scan was acquired. The reference signal was obtained by sending a low amplitude pulse into the film. The amplitude was controlled by either lowering the power of the laser pulse or decreasing the pulse amplitude setting on the pulser. As such, the $SDC_{i,j}$ parameter was calculated as follows:

$$SDC_{i,j} = (a * Ref - True)^2 \qquad (9.1)$$

Here a is the ratio between the amplitudes of the True and Reference signals.

- Two additional scanning configurations were incorporated in addition to the left-right and top-bottom configurations. These were left- bottom and top-right.

A β value of 1.03 was used and the results of the reconstruction can be seen in Figure 58. A comparison of the true geometry and the reconstructed geometry can be seen in Figure 59. It becomes evident that even though this technique captures the shape of the surface feature, but the lack of resolution causes the defect to appear smeared.
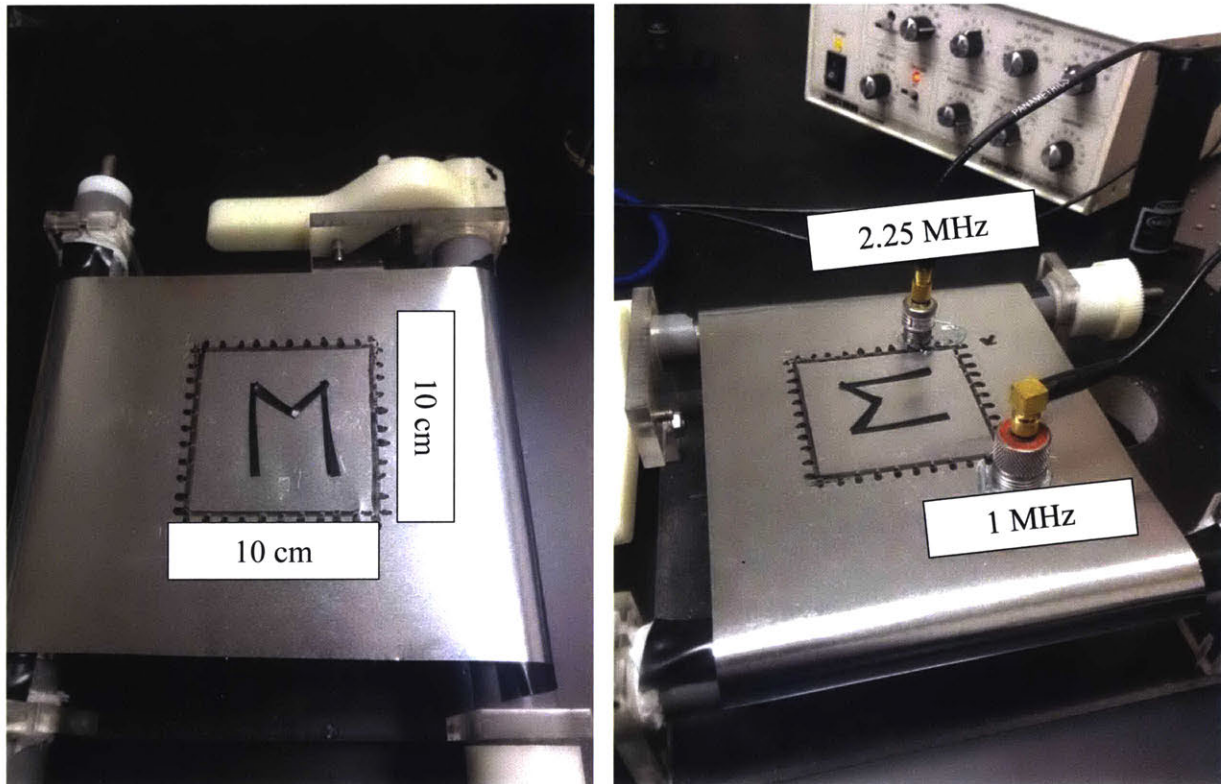
Figure 56: RAPID Imagig of 1mm Tape on 76 micron Aluminum ($\beta = 1.03$)

9.3 Conclusion

Based on these results, a number of important observations can be made:

1) As expected, the tip of the M where the tape overlapped does indeed appear prominently in the image indicating that this method can successfully pick up variations in thicknesses.

2) While a rough contour of the M can be observed, smaller spatial increments (increased transmit-receive pairs) will result in increased resolution.

3) Contact-based Lamb tomography interferes with signal collection due to the need for good contact, presence of ultrasound gel, and user variations. Non-contact Laster ultrasound would likely enhance the resolution seen here.
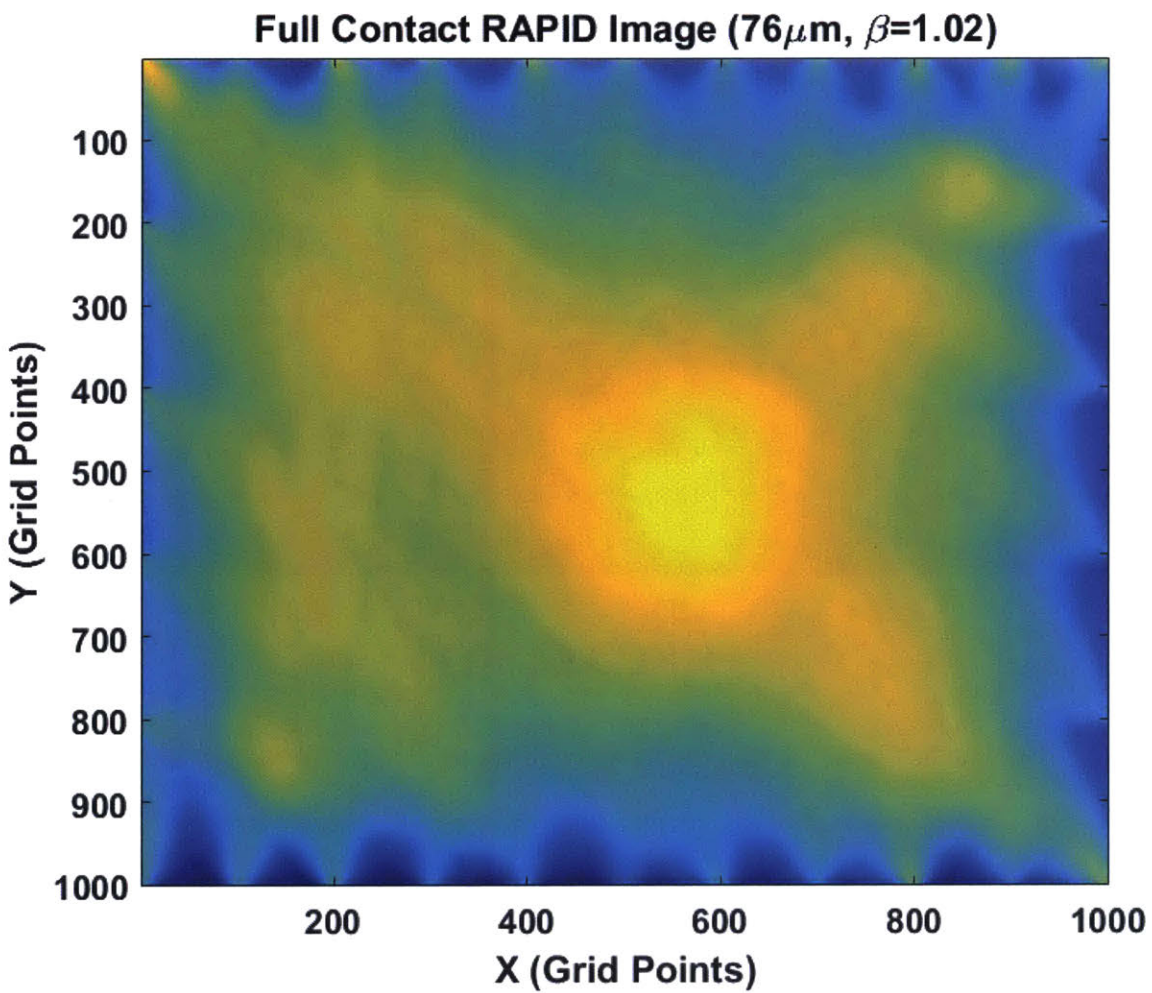
Figure 57: M Shape Reconstructed Using Increased Sensitivity RAPID ($\beta = 1.02$)

Full-Contact RAPID Imaging (76μm Aluminum, β = 1.03)
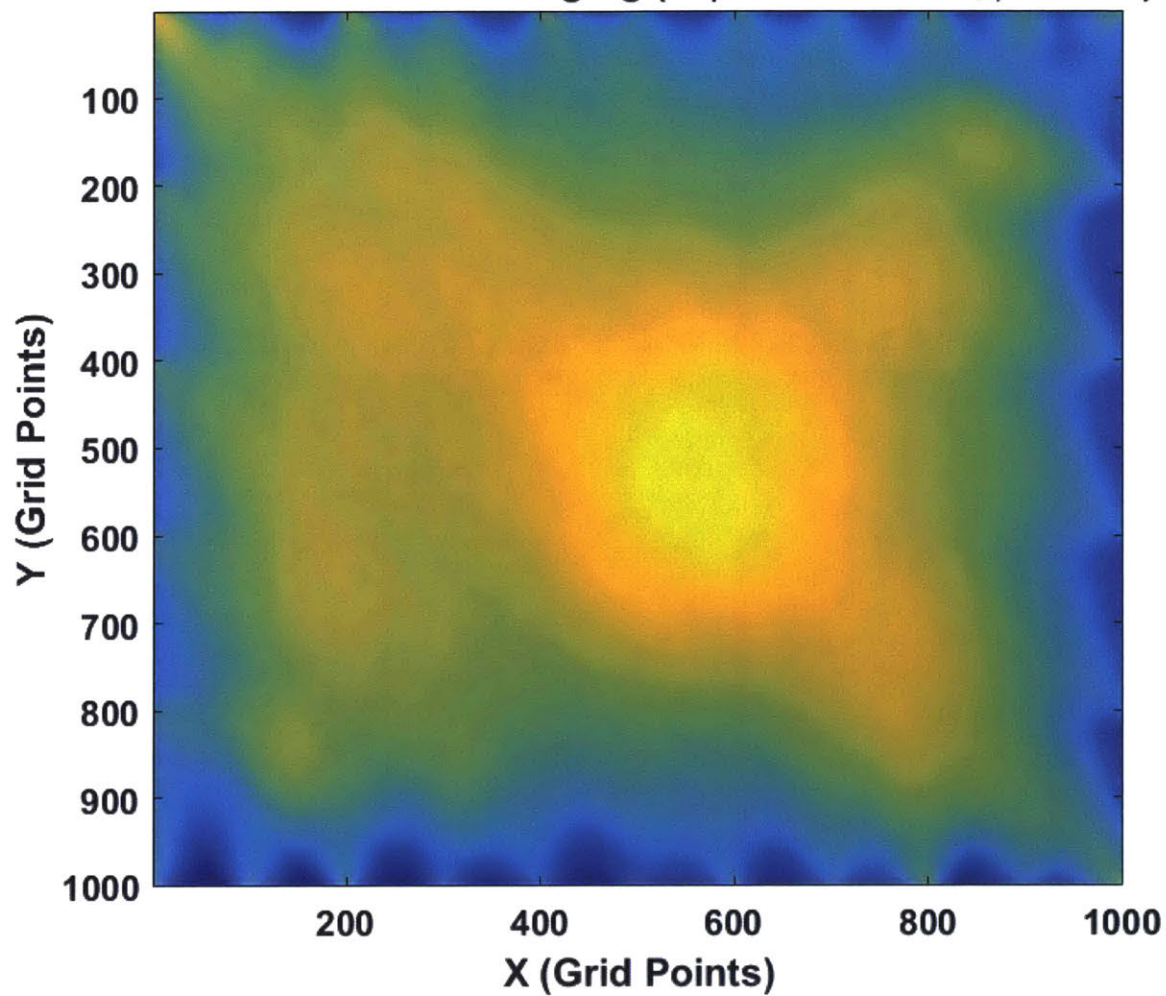
Figure 58: M Shape Reconstructed Using Increased Sensitivity RAPID (β = 1.03)

Figure 59: Comparison of Increased Sensitivty RAPID Imaging with True Geometry

10

PHOTOACOUSTIC LAMB WAVE TOMOGRAPHY

Given the success of the quasi-contact and increased sensitivity RAPID tomography, an attempt was made to make this process entirely non-contact. In addition to the 1064nm laser for the creation of Lamb waves, a 635nm vibrometer (OV-505 from Polytec) was used to receive/listen to the transmitted Lamb waves. The vibrometer and the laser were both deflected onto the setup using steering mirrors that could scan the entire area. An attempt at a tomographic reconstruction was made with a triangular cutout. A schematic of the experimental setup along with the test surface can be seen in Figure 60.
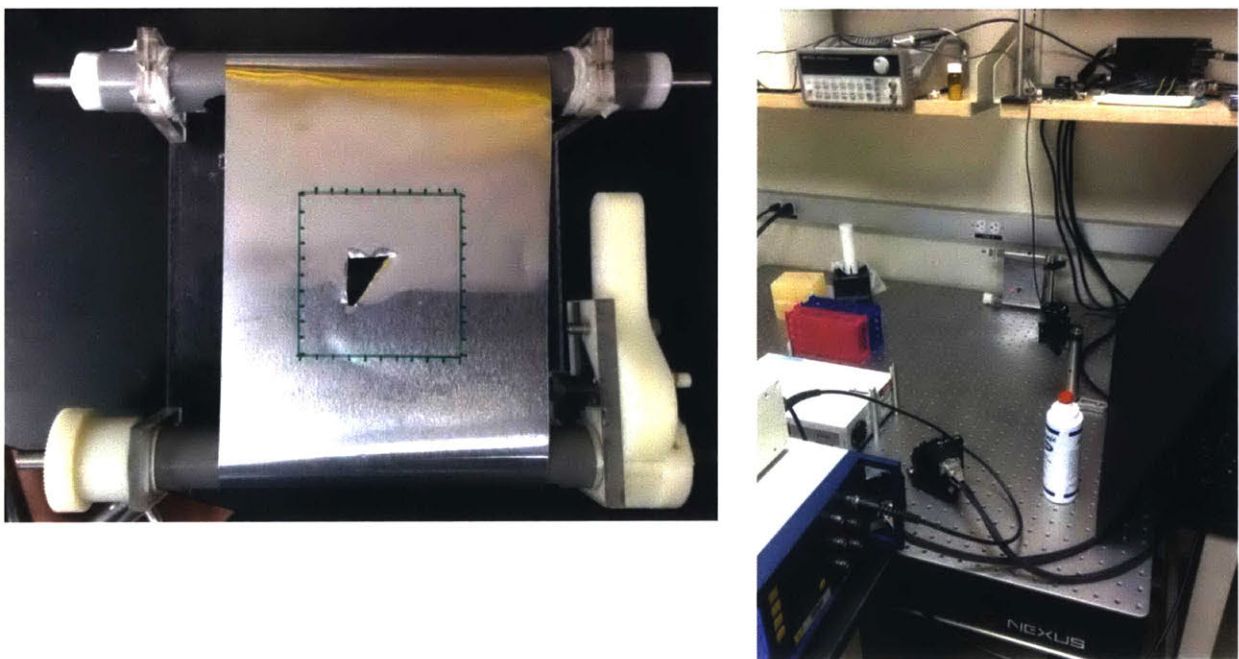
Figure 60: Experimental Setup for Photoacoustic Lamb Wave Tomography

However, as soon as the first data point was collected it became obvious that there were no signals being acquired. And the reason for this is that aluminum absorbs ~10-15% of incident light 635nm light and as such, there was reduced power returning to the vibrometer. The extremely sensitive nature of the vibrometer combined with the diminished power of returning light made it difficult to complete this analysis. That being said, two attractive alternatives are being considered for future testing:

1) Coating the aluminum with a reflective coating
2) Using a vibrometer whose wavelength is not absorbed by aluminum.

CHAPTER

11

FUTURE WORK AND CONCLUSIONS

Given the expansive nature of the work presented here, it is beneficial to summarize the high-level major conclusions and outline future work that would assist with the scale-up of this technology. The methods presented here have the potential to:

1) Identify cracks, holes, thickness variations, and surface additions with ~5mm accuracy in 76 μm aluminum thin films over relatively large areas. The methods show some success identifying features <5mm, but further refinement is required from the point of view of data acquisition and algorithm development.

2) Distinguish between surface additions of differing bulk fluid properties.

3) Create tomographic maps using a quasi-contact photoacoustic approach lending validity to the use of Lamb waves for large area metrology interrogation.

While these are major milestones, the following steps will make this technique ready to be deployed on a scale-up of industrialization:

1) Implement full non-contact tomography by using vibrometer of appropriate wavelength Given that the algorithm has already been established, implementing this will help with resolution of imaging and allow for finer imaging with no disturbance to the substrate.

2) Implement transducer arrays to capture signals at all receive locations simultaneously thereby cutting down the number of scans needed by N (number of transmit/receive points along each edge).

REFERENCES

[1] Krebs, Frederik C., and Roar R. Sandergaard. "Roll-to-Roll Fabrication of Large Area Functional Organic Materials." *Journal of Polymer Science Part B: Polymer Physics* 51.1 (2012): 16-34. Web.

[2] Jeans, Albert, Marcia Almanza-Workman, Robert Cobene, Richard Elder, Robert Garcia, Fernando Gomez-Pancorbo, Warren Jackson, Mehrban Jam, Han-Jun Kim, Ohseung Kwon, Hao Luo, John Maltabes, Ping Mei, Craig Perlov, Mark Smith, Carl Taussig, Frank Jeffrey, Steve Braymen, Jason Hauschildt, Kelly Junge, Don Larson, and Dan Stieler. "Advances in Roll-to-roll Imprint Lithography for Display Applications." *Alternative Lithographic Technologies II* (2010): n. pag. Web.

[3] Laasko, Petri, Saara Ruotsalainen, Eerik Halonen, Matti Mäntysalo, and Antti Kemppainen. "Sintering of Printed Nanoparticle Strcutures Using Laser Treatment." 28th International Congress on Applications 28th International Congress on Applications of Lasers and Electro-Opticsof Lasers and Electro-Optics, Nov. 2009. Web.

[4] Perelaer, Jolke, Chris E. Hendriks, Antonius W M De Laat, and Ulrich S. Schubert. "One-step Inkjet Printing of Conductive Silver Tracks on Polymer Substrates." *Nanotechnology* 20.16 (2009): 165303. Web.

[5] Schwartz, Evan. "Roll to Roll Processing for Flexible Electronics." Cornell University, 11 May 2006. Web.

[6] Randolph, Michael Aaron. *Commercial Assessment of Roll to Roll Manufacturing of Electronic Displays*. Diss. Massachusetts Institute of Technology, 2006. Cambridge: Massachusetts Institute of Technology, 2006. Web.

[7] Madappa, Muthappa Ponjanda. *Roll to Roll Manufacturing of Flexible Electronic Devices*. Diss. Visveswaraiah Technological U, 2006. Karnataka: Visveswaraiah Technological U, 2006. Web.

[8] "Home." *Roll-to-Roll Printing Market Size, Share - Report, 2024*. Global Markets Insight, n.d. Web. 15 May 2017.

[9] Lin, Xiaohui, Harish Subbaraman, Zeyu Pan, Amir Hosseini, Chris Longe, Klay Kubena, Paul Schleicher, Phillip Foster, Sean Brickey, and Ray Chen. "Towards Realizing High-

Throughput, Roll-to-Roll Manufacturing of Flexible Electronic Systems." *Electronics* 3.4 (2014): 624-35. Web.

[10] Shan, X. C., S. H. Chen, B. Salam, M. B. Mohahidin, and J. Wei. "Process Considerations, Process Challenges and Manufacturing Systems for Roll-to-roll Processing." *2016 IEEE 18th Electronics Packaging Technology Conference (EPTC)* (2016): n. pag. Web.

[11] Moyne, William. "Basic R2R Control Algorithms." *Run-to-Run Control in Semiconductor Manufacturing* (2000): n. pag. Web.

[12] Allen, Kimberly. "Reel to Real: Prospects for Flexible Displays." *MRS Proceedings* 814 (2004): n. pag. Web.

[13] Kang, Hwiwon, Hyejin Park, Yongsu Park, Minhoon Jung, Byung Chul Kim, Gordon Wallace, and Gyoujin Cho. "Fully Roll-to-Roll Gravure Printable Wireless (13.56â□...MHz) Sensor-Signage Tags for Smart Packaging." *Scientific Reports* 4.1 (2014): n. pag. Web.

[14] Gengel, G. "A Process for the Manufacture of Cost Competitive MCM Substrates." *Proceedings of the International Conference on Multichip Modules* (n.d.): n. pag. Web.

[15] Wendel, Bettina, Dominik Rietzel, Florian Kuhnlein, Robert Feulner, Gerrit Hulder, and Ernst Schmachtenberg. "Additive Processing of Polymers." *Macromolecular Materials and Engineering* 293rd ser. (2008): 799-809. Web.

[16] Chang, Joseph, Tong Ge, and Edgar Sanchez-Sinencio. "Challenges of Printed Electronics on Flexible Substrates." *2012 IEEE 55th International Midwest Symposium on Circuits and Systems (MWSCAS)* (2012): n. pag. Web.

[17] Espinosa, Nieves, Rafael GarcÃa-Valverde, Antonio Urbina, Frank Lenzmann, Matthieu Manceau, Dechan Angmo, and Frederik C. Krebs. "Life Cycle Assessment of ITO-free Flexible Polymer Solar Cells Prepared by Roll-to-roll Coating and Printing." *Solar Energy Materials and Solar Cells* 97 (2012): 3-13. Web.

[18] Tsuda, Tomio, Shinji Inoue, Akihiro Kayahara, Shin-Ichi Imai, Tomoya Tanaka, Naoaki Sato, and Satoshi Yasuda. "Advanced Semiconductor Manufacturing Using Big Data." *IEEE Transactions on Semiconductor Manufacturing* 28.3 (2015): 229-35. Web.

[19] Subbaraman, Harish, Xiaohui Lin, Xiaochuan Xu, Ananth Dodabalapur, L. Jay Guo, and Ray T. Chen. "Metrology and Instrumentation Challenges with High-rate, Roll-to-roll Manufacturing of Flexible Electronic Systems." *Instrumentation, Metrology, and Standards for Nanomanufacturing, Optics, and Semiconductors VI* (2012): n. pag. Web.

102

[20] Machui, Florian, Markus HÃ¶sel, Ning Li, George D. Spyropoulos, Tayebeh Ameri, Roar R. SÃ¸ndergaard, Mikkel JÃ¸rgensen, Arnulf Scheel, Detlef Gaiser, Kilian Kreul, Daniel Lenssen, Mathilde Legros, NoÃ«lla Lemaitre, Marja Vilkman, Marja VÃ¤limÃ¤ki, Sirpa Nordman, Christoph J. Brabec, and Frederik C. Krebs. "Cost Analysis of Roll-to-roll Fabricated ITO Free Single and Tandem Organic Solar Modules Based on Data from Manufacture." *Energy & Environmental Science* 7.9 (2014): 2792. Web.

[21] To, Hoang Minh, Dong Keun Shin, and Sung Lim Ko. "On-Line Measurement of Wrinkle Using Machine Vision." *Lecture Notes in Computer Science Computational Science and Its Applications â€" ICCSA 2007* (n.d.): 931-40. Web.

[22] Chinthalapudi, Ajaykumar S. *Investigation of Methods to Detect Defects in Thin Layered Materials*. Diss. Blekinge Institute of Technology, 2005. Karlskrona: Blekinge Institute of Technology, 2005. Web.

[23] Lovejoy, David. "Essential Magnetic Characteristics for Magnetic Particle Inspection." *Magnetic Particle Inspection* (1993): 45-55. Web.

[24] Weischedel, H.r., and R.p. Ramsey. "Electromagnetic Testing, a Reliable Method for the Inspection of Wire Ropes in Service." *NDT & E International* 24.6 (1991): 325. Web.

[25] Weischedel, H.r., and R.p. Ramsey. "Electromagnetic Testing, a Reliable Method for the Inspection of Wire Ropes in Service." *NDT & E International* 24.6 (1991): 325. Web.

[26] Liao, T.warren, and Jiawei Ni. "An Automated Radiographic NDT System for Weld Inspection: Part I â€" Weld Extraction." *NDT & E International* 29.3 (1996): 157-62. Web.

[27] Krause, M., M. BÃ¶rmann, R. Frielinghaus, F. Kretzschmar, O. Kroggel, K.j. Langenberg, C. Maierhofer, W. MÃ¼ller, J. Neisecke, M. Schickert, V. Schmitz, H. Wiggenhauser, and F. Wollbold. "Comparison of Pulse-echo Methods for Testing Concrete." *NDT & E International* 30.4 (1997): 195-204. Web.

[28] "Longitudinal Waves | Sound Waves and Pressure Waves." *Physics*. Byjus Classes, 08 Sept. 2016. Web. 15 May 2017.

[29] Kojimoto, Nigel C. *Ultrasonic Inspection Methods for Defect Detection and Process Control in Roll-to-Roll Flexible Electronics Manufacturing*. Diss. Massachusetts Institute of Technology, 2015. Cambridge: Massachusetts Institute of Technology, 2015. Web.

[30] Bedford, Anthony, and D. S. Drumheller. *Introduction to Elastic Wave Propagation*. Chichester: John Wiley & Sons, 1996. Print.

[31] "Photoacoustic Imaging." *Universiteit Twente in Enschede: High Tech Human Touch*. N.p., n.d. Web. 15 May 2017.

[32] Tabatabaeipour, Morteza, Jan Hettler, Steven Delrue, and Koen Van Den Abeele. "Reconstruction Algorithm for Probabilistic Inspection of Damage (RAPID) in Composites." *11th European Conference on Non-Destructive Testing* (2014): n. pag. Oct. 2014. Web.

[33] Zhou, Lianqun, Yihui Wu, Ming Xuan, Jean-FranÃ§ois Manceau, and FranÃ§ois Bastien. "A Multi-Parameter Decoupling Method with a Lamb Wave Sensor for Improving the Selectivity of Label-Free Liquid Detection." *Sensors* 12.12 (2012): 10369-0380. Web.

[34] Jeans, Albert, Marcia Almanza-Workman, Robert Cobene, Richard Elder, Robert Garcia, Fernando Gomez-Pancorbo, Warren Jackson, Mehrban Jam, Han-Jun Kim, Ohseung Kwon, Hao Luo, John Maltabes, Ping Mei, Craig Perlov, Mark Smith, Carl Taussig, Frank Jeffrey, Steve Braymen, Jason Hauschildt, Kelly Junge, Don Larson, and Dan Stieler. "Advances in Roll-to-roll Imprint Lithography for Display Applications." *Alternative Lithographic Technologies II* (2010): n. pag. Web.

[35] Popescu, D., F. D. Anania, C. E. Cotet, and C. G. Amza. "Fully-Automated Liquid Penetrant Inspection Line Simulation Model for Increasing Productivity." *International Journal of Simulation Modelling* 12.2 (2013): 82-93. Web.

[36] Bedford, Anthony, and D. S. Drumheller. *Introduction to Elastic Wave Propagation*. Chichester: John Wiley & Sons, 1996. Print.

[37] "Chebfun—numerical Computing with Functions." *Numerical Computing with Functions » Chebfun*. The University of Oxford, n.d. Web. 30 May 2017.

APPENDICES

Appendix A: MATLAB® CODE

A1: MATLAB® Code for Quasi-Contact RAPID Tomography

Left-Right Data analysis

```
%Material properties
Cl = 6320; %[m/s]
Ct = 3170; %[m/s]

%Define boundary
L = 9;
W = 9;

%Grid Spacings
x = [0:0.01:L]';
y = [0:-0.01:-W]';

%Transmit and Receive co-ordinates
T=[ 9 0; 9 -1; 9 -2; 9 -3;9 -4; 9 -5; 9 -6; 9 -7];
R = T;
R(:,1) = 0;

%Create grid
[X Y] = meshgrid(x,y);

%Number of TR pairs
N = 8;

%Caluclate signal difference coefficient
[Psi, Speed, SoundCount] = SDCLR(N,1);

%Other parameters
beta = 1.05;

%Final grid
GridLR = zeros(size(X,1),size(X,2));
countt = 1;

% RAPID alogrithm
for i = 1:size(X,1)
    for ii = 1:size(X,2)
        Sum = 0;
        SpeedSum = 0;
```

```
            count = 1;
            for iii = 1:N
                  for iv = 1:N

                        Tx = T(iii,1);
                        Ty = T(iii,2);
                        Rx = R(iv,1);
                        Ry = R(iv,2);


                        Rvalue = Rval(X(i,ii),Y(i,ii),Tx,Ty,Rx,Ry);

                        if Rvalue<beta

                              Sum = Sum + (beta - Rval(X(i,ii),Y(i,ii),Tx,Ty,Rx,Ry))/(beta-
1) * Psi(count,1);

                        else
                            Sum =  Sum + 0;
                        end
                        %
                        count = count + 1;
                  end
            end

        countt = countt + 1;
        GridLR(i,ii) = Sum;



    end
end
```

Top-Down Data analysis

```
%Define boundary
L = 9;
W = 9;
x = [0:0.01:L]';
y = [0:-0.01:-W]';

%Transmit and Receive co-ordinates
T=[ 1 0; 2 0; 3 0;4 0; 5 0; 6 0; 7 0; 8 0];
R = T;
R(:,2) = -W;

%Create grid
[X Y] = meshgrid(x,y);

%Number of TR pairs
```

```
N = 8;

%Caluclate Signal Difference Coefficient
[Psi,Speed, SoundCount] = SDCTB(N,2);

%Final grid
GridTD= zeros(size(X,1),size(X,2));
SpeedTB = zeros(size(X,1),size(X,2));

countt = 1;

% RAPID alogrithm
for i = 1:size(X,1)
    for ii = 1:size(X,2)
        Sum = 0;
        SpeedSum = 0;

            count = 1;
            for iii = 1:N
                for iv = 1:N
                    Tx = T(iii,1);
                    Ty = T(iii,2);
                    Rx = R(iv,1);
                    Ry = R(iv,2);
                    Rvalue = Rval(X(i,ii),Y(i,ii),Tx,Ty,Rx,Ry);

                    if Rvalue<beta

                        Sum = Sum + (beta - Rval(X(i,ii),Y(i,ii),Tx,Ty,Rx,Ry))/(beta-
1) * Psi(count,1);

                    else
                        Sum =  Sum + 0;
                    end
                    %
                    count = count + 1;
                end
            end
            countt = countt + 1;
            GridTD(i,ii) = Sum;


    end
end

%Combine both imaging perspectives
GridFinal = GridLR + GridTD;

%Clean up image based on probability threshold
```

```
Max = max(max(GridFinal));
Metric = GridFinal./Max;
for i = 1: size(GridFinal,1)
    for ii = 1:size(GridFinal,2)
        if Metric(i,ii)>0.85
            GridFinal(i,ii) = GridFinal(i,ii);
        else
            GridFinal(i,ii) = 0;
        end
    end
end

%Plotting
figure(1); imagesc(GridLR);hold on
figure(2); imagesc(GridTD);hold on
figure(3); imagesc(GridFinal);hold on
% pcolor(X,Y,GridFinal);
% shading flat;
```

A2: MATLAB® Code for Increased Sensitivity RAPID Tomography

Left-Right Data analysis

```
%Material properties
Cl = 6320; %[m/s]
Ct = 3170; %[m/s]

%Define boundary
L = 5;
W = 5;
x = [0:0.005:L]';
y = [0:-0.005:-W]';

%Transmit and Receive co-ordinates
T=[ 0 0; 0 -0.5; 0 -1; 0 -1.5; 0 -2; 0 -2.5; 0 -3; 0 -3.5; 0 -4; 0 -4.5; 0 -5];
R = T;
R(:,1) = L;

%Create grid
[X Y] = meshgrid(x,y);

%Number of TR pairs
N = 11;

%Caluclate SDC
[Psi, Speed, SoundCount] = SDCLR(N,1);
```

```matlab
%Other parameters
beta = 1.02;

%Final grid
GridLR = zeros(size(X,1),size(X,2));
countt = 1;

% RAPID alogrithm
for i = 1:size(X,1)
    i
    for ii = 1:size(X,2)
        Sum = 0;
        SpeedSum = 0;

            count = 1;
            for iii = 1:N
                for iv = 1:N

                    Tx = T(iii,1);
                    Ty = T(iii,2);
                    Rx = R(iv,1);
                    Ry = R(iv,2);


                    Rvalue = Rval(X(i,ii),Y(i,ii),Tx,Ty,Rx,Ry);

                    if Rvalue<beta

                        Sum = Sum + (beta - Rval(X(i,ii),Y(i,ii),Tx,Ty,Rx,Ry))/(beta-
1) * Psi(count,1);

                    else
                        Sum =  Sum + 0;
                    end
                    %
                    count = count + 1;
                end
            end

        countt = countt + 1;
        GridLR(i,ii) = Sum;

    end
end
%Plotting
GridLR = GridLR./max(max(GridLR));
figure(1); imagesc(GridLR);hold on
```

Top-Down analysis

```
%Define boundary
L = 5;
W = 5;
x = [0:0.005:L]';
y = [0:-0.005:-W]';

%Transmit and Receive co-ordinates
T=[ 0 0; 0.5 0; 1 0;1.5 0; 2 0; 2.5 0; 3 0; 3.5 0; 4 0; 4.5 0; 5 0];
R = T;
R(:,2) = -W;

%Create grid
[X Y] = meshgrid(x,y);

%Number of TR pairs
N = 11;

%Caluclate SDC
[Psi,Speed, SoundCount] = SDCTB(N,2);

%Final grid
GridTD= zeros(size(X,1),size(X,2));
countt = 1;

% RAPID alogrithm
for i = 1:size(X,1)
    i
    for ii = 1:size(X,2)
        Sum = 0;
        SpeedSum = 0;

            count = 1;
            for iii = 1:N
                for iv = 1:N
                    Tx = T(iii,1);
                    Ty = T(iii,2);
                    Rx = R(iv,1);
                    Ry = R(iv,2);
                    Rvalue = Rval(X(i,ii),Y(i,ii),Tx,Ty,Rx,Ry);

                    if Rvalue<beta

                        Sum = Sum + (beta - Rval(X(i,ii),Y(i,ii),Tx,Ty,Rx,Ry))/(beta-
1) * Psi(count,1);
                    else
                        Sum =  Sum + 0;
                    end
                    %
                    count = count + 1;
```

```
                    end
                end
            countt = countt + 1;
            GridTD(i,ii) = Sum;

        end
    end
GridTD = GridTD./max(max(GridTD));
```

Left-Down analysis

```
%Define boundary
L = 5;
W = 5;
x = [0:0.005:L]';
y = [0:-0.005:-W]';

%Transmit and Receive co-ordinates
T=[ 0 0; 0 -1; 0 -2; 0 -3; 0 -4];
R = [ 0 -5; -1 -5; -2 -5; -3 -5; -4 -5; -5 -5];


%Create grid
[X Y] = meshgrid(x,y);

%Number of TR pairs
N = 5;

%Caluclate SDC
[Psi,Speed, SoundCount] = SDCLB(N,3);

%Final grid
GridLD= zeros(size(X,1),size(X,2));
countt = 1;

% RAPID alogrithm
for i = 1:size(X,1)
    i
    for ii = 1:size(X,2)
        Sum = 0;
        SpeedSum = 0;

            count = 1;
            for iii = 1:N
                for iv = 1:N+1
                    Tx = T(iii,1);
                    Ty = T(iii,2);
                    Rx = R(iv,1);
                    Ry = R(iv,2);
                    Rvalue = Rval(X(i,ii),Y(i,ii),Tx,Ty,Rx,Ry);
```

```
                if Rvalue<beta

                    Sum = Sum + (beta - Rval(X(i,ii),Y(i,ii),Tx,Ty,Rx,Ry))/(beta-
1) * Psi(count,1);
                else
                    Sum =  Sum + 0;
                end
                %
                count = count + 1;
            end
        end
        countt = countt + 1;
        GridLD(i,ii) = Sum;

    end
end
GridLD = GridLD./max(max(GridLD));
```

9.4   Top-Right analysis

```
%Define boundary
L = 5;
W = 5;
x = [0:0.005:L]';
y = [0:-0.005:-W]';

%Transmit and Receive co-ordinates
T=[ 0 0; 1 0; 2 0; 3 0; 4 0];
R = [ 5 0; 5 -1; 5 -2; 5 -3; 5 -4 ; 5 -5];


%Create grid
[X Y] = meshgrid(x,y);

%Number of TR pairs
N = 5;

%Caluclate SDC
[Psi,Speed, SoundCount] = SDCTR(N,3);

%Final grid
GridTR= zeros(size(X,1),size(X,2));
SpeedTR = zeros(size(X,1),size(X,2));


countt = 1;

% RAPID alogrithm
for i = 1:size(X,1)
    i
```

```
    for ii = 1:size(X,2)
        Sum = 0;
        SpeedSum = 0;

            count = 1;
            for iii = 1:N
                for iv = 1:N+1
                    Tx = T(iii,1);
                    Ty = T(iii,2);
                    Rx = R(iv,1);
                    Ry = R(iv,2);
                    Rvalue = Rval(X(i,ii),Y(i,ii),Tx,Ty,Rx,Ry);

                    if Rvalue<beta
                        Sum = Sum + (beta - Rval(X(i,ii),Y(i,ii),Tx,Ty,Rx,Ry))/(beta-1)
* Psi(count,1);

                    else
                        Sum =  Sum + 0;
                    end
                    %
                    count = count + 1;
                end
            end
            countt = countt + 1;
            GridTR(i,ii) = Sum;



    end
end


GridTR = GridTR./max(max(GridTR));
```

Final Processing

```
%Add difference imaging perspectives
GridFinal = flipud(GridLR') + GridTD + GridLD + GridTR;
GridFinal = GridFinal./max(max(GridFinal));

%Clean up image based on probability threshold
Max = max(max(GridFinal));
Metric = GridFinal./Max;
for i = 1: size(GridFinal,1)
    for ii = 1:size(GridFinal,2)
        if Metric(i,ii)>0.65
            GridFinal(i,ii) = GridFinal(i,ii);
        else
            GridFinal(i,ii) = 0;
        end
```

```
        end
    end



%Plotting
figure(1); imagesc(Metric);hold on
```

A3: MATLAB® Code for k-Wave Simulations

```
clear all;

% simulation settings
DATA_CAST = 'single';

%Source Properties
Freq = 1e6; %[Hz]
c = 2400; %[m/s]
Lambda = c/1e6; %[mm]
a = 2; %[grid pts/wavelength]
Lx = 50/1000; %[m]
Ly = 10/1000; %[m]
Lz = 0.08/1000; %[m]

%Make grid
Nx = floor(Lx/Lambda * a);
Ny = floor(Ly/Lambda*a);
Nz = floor(Ny/2);
dx = Lx/Nx;
dy = Ly/Ny;
dz = Lz/Nz;
kgrid = makeGrid(Nx, dx, Ny, dy, Nz, dz);

% define the properties of the propagation medium
medium.sound_speed = c;   % [m/s]
medium.alpha_coeff = 0.33;   % [dB/(MHz^y cm)]
medium.alpha_power = 1.1;
medium.density = 1380*ones(Nx,Ny,Nz);       %[kg/m3]



% define properties of the input signal
source_strength = 10e6;         % [MPa]
tone_burst_freq = Freq;         % [Hz]
tone_burst_cycles = 1;
```

```matlab
% create time array
t_end = 50e-6;
kgrid.t_array = makeTime(kgrid, medium.sound_speed, [], t_end);

% create the input signal using toneBurst
input_signal = toneBurst(1/kgrid.dt, tone_burst_freq, tone_burst_cycles);

% scale the source magnitude by the source_strength divided by the
% impedance (the source is assigned to the particle velocity)
input_signal = (source_strength./(c*1380)).*input_signal;

% physical properties of the transducer
transducer.number_elements = 1;    % total number of transducer elements
transducer.element_width = 1;       % width of each element [grid points]
transducer.element_length = 1;      % length of each element [grid points]

transducer.element_spacing = 0;     % spacing (kerf width) between the elements [grid
points]
transducer.radius = inf;            % radius of curvature of the transducer [m]

% calculate the width of the transducer in grid points
transducer_width = transducer.number_elements*transducer.element_width ...
    + (transducer.number_elements - 1)*transducer.element_spacing;

% use this to position the transducer in the middle of the computational grid
transducer.position = round([Nx-4, Ny/2 - transducer_width/2, 1]);

% apodization
transducer.transmit_apodization = 'Rectangular';
transducer.receive_apodization = 'Rectangular';

% properties used to derive the beamforming delays
transducer.sound_speed = 2400;              % sound speed [m/s]
% transducer.focus_distance = 20e-3;         % focus distance [m]
% transducer.elevation_focus_distance = 19e-3;% focus distance in the elevation plane
[m]
% transducer.steering_angle = 0;             % steering angle [degrees]

% define the transducer elements that are currently active
transducer.active_elements = zeros(transducer.number_elements, 1);
transducer.active_elements(:) = 1;

% append input signal used to drive the transducer
transducer.input_signal = input_signal;

% create the transducer using the defined settings
transducer = makeTransducer(kgrid, transducer);

% define a binary sensor mask
% define a sensor mask through the central plane of the transducer
```

```matlab
medium.density(Nx  - transducer.element_length-25, floor(Ny/2), 1) = 1380;

sensor.mask = zeros(Nx, Ny, Nz);

sensor.mask(Nx-25, round(Ny/2 - transducer_width/2), 1) = 1;

% run the simulation
input_args = {'DisplayMask', sensor.mask, ...
'PMLInside', false, ...
    'PlotPML', true, ...
    'PMLSize', [10], ...
    'PMLAlpha', [2], ...
    'PlotScale', [-source_strength/2, source_strength/2]};


[sensor_data] = kspaceFirstOrder3D(kgrid, medium, transducer, sensor,input_args{:});


% calculate the amplitude spectrum of the input signal and the signal
% recorded each of the sensor positions
[f_input, as_input] = spect([input_signal, zeros(1, 2*length(input_signal))],
1/kgrid.dt);
[f, as_1] = spect(sensor_data(1, :), 1/kgrid.dt);
% [f, as_2] = spect(sensor_data(2, :), 1/kgrid.dt);
% [f, as_3] = spect(sensor_data(3, :), 1/kgrid.dt);
keyboard
% plot the input signal and its frequency spectrum
figure;
subplot(2, 1, 1), plot((0:kgrid.dt:(length(input_signal)-1)*kgrid.dt)*1e6,
input_signal, 'k.-','MarkerSize',14);
xlabel('Time [\mus]');
ylabel('Input Particle Velocity [m/s]');
subplot(2, 1, 2), plot(f_input/1e6, as_input./max(as_input(:)), 'k.-
','MarkerSize',14);
hold on;
line([tone_burst_freq, tone_burst_freq]/1e6, [0 1], 'Color', 'k', 'LineStyle', '--
','LineWidth',4);
xlabel('Frequency [MHz]');
ylabel('Relative Amplitude Spectrum [au]');
f_max = medium.sound_speed / (2*dx);
set(gca, 'XLim', [0 f_max/1e6]);
set(gca,'FontSize',20,'FontWeight','bold');


keyboard
% plot the recorded time series
figure;
plot(kgrid.t_array*1e6, sensor_data./max(sensor_data),'r.','MarkerSize',14);
xlabel('Time [\mus]');
ylabel('Magnitude (a.u.)');
title('Response 2.56 cm Away from Source');
set(gca,'FontSize',20,'FontWeight','bold');
```

```matlab
% plot the corresponding amplitude spectrums
figure;
plot(f/1e6, as_1./max(as_1(:)), 'k-');
legend('Sensor Position 1', 'Sensor Position 2', 'Sensor Position 3');
xlabel('Frequency [MHz]');
ylabel('Normalised Amplitude Spectrum [au]');
f_max = medium.sound_speed / (2*dx);
set(gca, 'XLim', [0 f_max/1e6]);
```

A4: MATLAB® Code Full Contact Lamb Wave Tomography

```matlab
%Define Plate dimensions in cm
L = 12;
H = 12;
dx = 1;
dy = 1;

%Define Left-Right Transmit-Receive Co-ordinates
Tl=[ 0 -0.5; 0 -1.5; 0 -2.5; 0 -3.5;0 -4.5; 0 -5.5; 0 -6.5; 0 -7.5; 0 -8.5; 0 -9.5; 0
-10.5; 0 -11.5];
Rl = Tl;
Rl(:,1) = L;

%Define Top-Bottom Transmit-Receive Co-ordinates
Tt = Tl;
Rt = Rl;

%Computer lengths of intersection with grid blocks for left-right (l) and
%top-bottom (t)
Lengthsl = ComputeLengths(Tl,Rl,dx,dy);
Lengthst = ComputeLengths(Tt,Rt,dx,dy);


N = length(Tt);
%Compute energy contained in every transmit receive pair (integration)
Psil = CreatePsi(N,1);
Psit = CreatePsi(N,2);


%Perform computation
Grid = VisualizeDefects(Lengthsl,Psil(:),L);
Grid = Grid + flipud(VisualizeDefects(Lengthst,Psit(:),L)');
```

```
%Visualize results
figure(1)
imagesc(Grid(1:end,2:end))
figure(2)
surfc(flipud(Grid(1:end,2:end)))
figure(3)
contour3(flipud(Grid(1:end,2:end)))
```

```
function Grid = VisualizeDefects(Lengths,Psi,L)

%Psi is the energy contained in a transmit-receieve pair
N  = sqrt(length(Psi));
Grid = zeros(N^2,1);

for i = 1:size(Lengths,1)

    Total = sum(Lengths(i,:));
    for ii = 1:size(Lengths,2)
        if Lengths(i,ii)~=0

            frac  = (Lengths(i,ii)/Total);
            Grid(ii,1) = Grid(ii,1)+ frac*Psi(i,1);


        end
    end
end
Grid = reshape(Grid,N,N)';
```

Appendix B: LabVIEW® Code

B1: LabVIEW® Code for Full Contact Data Acquisition with Block Flow Diagram [29]